Integral Equation Theories and Computer Simulations for Systems with Bounded Potentials

Diplomarbeit
zur Erlangung des Akademischen Grades
Magistra der Naturwissenschaften

unter Leitung von
Ao. Univ. Prof. Dr. Martin Neumann
Institut für Experimentalphysik, Universität Wien
und
Ao. Univ. Prof. Dr. Gerhard Kahl
Institut für Theoretische Physik, Technische Universität Wien

eingereicht an der Fakultät für Naturwissenschaften und Mathematik
der Universität Wien

von

Bianca Maria Mladek

Wien, im Dezember 2003

To my grandmothers Elisabeth and Rosmarie.

Abstract

In an effort to gain more insight into the general thermodynamic behaviour of fluids interacting by means of bounded potentials we have analysed three types of potentials, namely the Gaussian core model (GCM), the double Gaussian core model (DGCM), which possibly contains a small attractive part and the generalised Gaussian core model (GGCM-n), which contains a tuneable parameter n that interpolates between the continuous GCM and the discontinuous penetrable sphere model. We have examined the radial distribution function $g(r)$ and the dimensionless equation of state $\beta P/\varrho$ for these potentials as obtained by the mean spherical, the hypernetted chain and the Percus-Yevick approximation. For the case of the GCM, we have also developed the formalism of the self-consistent Ornstein-Zernike approximation, i.e. an advanced liquid state theory that guarantees thermodynamic self-consistency between the compressibility and the virial route. We have then complemented the acquired results with data obtained by Monte Carlo simulations.

Furthermore, we have investigated a criterion proposed by Likos et al. [Phys. Rev. E **63**, 31206 (2001)] which classifies potentials by deciding whether a given system will freeze at all temperatures into a crystal of particle-clusters or will display re-entrant melting.

Kurzfassung

Im Bemühen, detaillierte Einsicht in das thermodynamische Verhalten von Flüssigkeiten zu erhalten, die mittels sogenannter weicher Potentiale wechselwirken, haben wir drei verschiedene Potentiale untersucht: das ,,Gaussian core model" (GCM), das ,,double Gaussian core model" (DGCM), das eventuell einen attraktiven Teil haben kann, und das ,,generalised Gaussian core model" (GGCM-n), das mittels eines veränderlichen Parameters n zwischen dem kontinuierlichen GCM und dem unstetigen ,,penetrable sphere model" variiert. Wir haben die Paarverteilungsfunktion $g(r)$ und die dimensionslose Zustandsgleichung $\beta P/\varrho$ für diese Potentiale mittels der ,,mean spherical", der ,,hypernetted chain" und ,,Percus-Yevick" Näherung berechnet. Im Falle des GCM haben wir außerdem den Formalismus der ,,self-consistent Ornstein-Zernike approximation", die thermodynamische Selbstkonsistenz zwischen der Kompressibilitäts- und der Virial-Zustandsgleichung erzwingt, entwickelt. Weiters haben wir unsere Resultate durch Daten aus Monte Carlo Simulationen ergänzt.
Darüber hinaus haben wir ein Kriterium getestet, welches von Likos et al. [Phys. Rev. E **63**, 31206 (2001)] aufgestellt wurde und das es erlaubt, Potentiale danach zu klassifizieren, ob ein System bei jeder Temperatur in Form eines Kristalls aus Teilchenclustern erstarrt oder ob sogenanntes ,,re-entrant melting" auftritt.

A good traveller has no fixed plans, and is not intent on arriving.

Lao-Tse

Contents

Chapter 1

Introduction

Out of the three states of matter - gaseous, liquid and solid - the fluid state is the most difficult one to understand. Whereas gases were already studied extensively in the nineteenth century and solids were widely analysed in the middle of the twentieth century by taking benefit of lattice periodicity and quantum physics, the theoretical concepts developed in these fields could not be applied to fluids: on the one hand, unlike solids, fluids are not periodic, thus, principles of symmetry are of no use in understanding them. On the other hand, due to the intermediate and high densities of the liquid state, density expansions around the gaseous state ($\varrho \to 0$) are not applicable as the series expansion cannot be truncated after a finite number of terms. Furthermore, there can be non-trivial short- and long-range correlations between the constituent particles not present in gases. In particular, these correlations lead to liquid state concepts which are practically intractable by analytical means. Hence, the thermodynamic behaviour of fluids is very difficult to be handled by the conventional methods of condensed matter theory.

However, things began to change with the rapid development of increasingly powerful computers after World War II, which led to an equally rapid the development of atomic simulation methods which - in principle - yield exact solutions to thermodynamic and statistical mechanical problems. In the fifties and the following decades, new liquid state theories, i.e. integral equation theories (IETs) and thermodynamic perturbation theories, were introduced. Some of these theories could be solved analytically for a few simple model systems, but the vast majority could only be solved numerically; in this way computers permitted new insight into the structure of fluids and allowed to elaborate more sophisticated theories.

Nowadays, there are three different ways to approach the problem of understanding liquids: the conventional routes - experiment and theory - and as a complementary approach, computer simulation.

The first liquids to be studied were *simple, atomic liquids* [1]. These are systems consisting of a single component of spherical particles - atoms such as noble gases - interacting by a radially symmetric pairwise additive potential. A wide range of successful theories was formulated for

this kind of liquids and the validity of their predictions was tested against the data obtained by computer simulations and experiments. Nowadays, these theories are well established and they allow to reliably predict the behaviour of simple, atomic liquids and, to a certain extent, also that of simple polyatomic fluids.

Unfortunately, a large number of of liquids we encounter in our everyday lives and which are of great technical or biological importance are of a different kind: their main characteristic is that they consist of mesoscopic particles or structures, i.e. their sizes range from 1nm - 1µm and they are a subset of the class of *complex fluids* [2].[1] This subgroup comprises polymers, dispersion colloids, tensides, biological macromolecules, and the like. As the mesoscopic size of the constituent particles of such systems results in a certain "softness" of the interaction, which means that their rigidity against mechanical deformations is many orders of magnitude smaller than that of atomic systems [3], these materials are also referred to as *soft matter*.

The aim of soft condensed matter physics is to predict the macroscopic behaviour of soft matter on the basis of the material's essential microscopic properties. The main difficulty in doing so is to handle the large number of degrees of freedom of the components constituting the mesoscopic particles. Statistical mechanics solves this problem by integrating out degrees of freedom on the microscopic scale. For instance, a star polymer or dendrimer consisting of many connected monomers can be regarded as one effective particle with only a few translational degrees of freedom (see figure 1.1). A prediction of the thermodynamic behaviour of these complex fluids can then be obtained by applying to these effective particles the same methods also used for simple liquids.

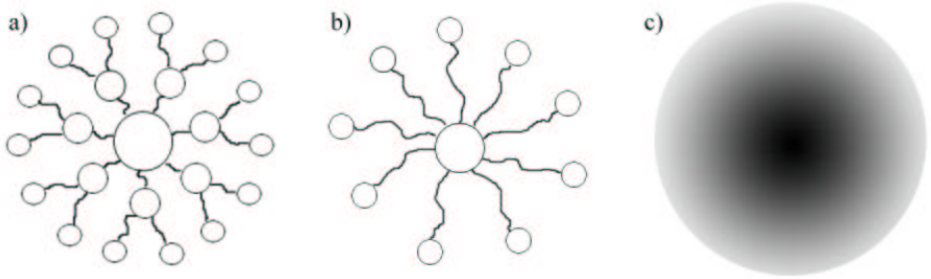

Figure 1.1: a) Schematic representation of a dendrimer (from Greek *τό δένδρον* - tree), which is an artificially manufactured or synthesised molecule built from branched units (monomers). b) Schematic representation of a star polymer. c) Schematic representation of an effective particle interacting via a soft potential.

The main difference between a simple, atomic or molecular fluid and a system of effective particles representing a complex fluid is the nature of the interaction potential. Whereas most simple fluids interact via hard core potentials, such as the Lennard-Jones or the hard core Yukawa potential, soft matter systems can be described by *soft potentials*, i.e. potentials that remain finite at $r = 0$ or diverge only very slowly as $r \to 0$ (see figure 1.2). In the case of star polymers, for instance, this

[1] This term does not imply that these systems are only studied in their fluid state.

is because the structure of these particles allows two such polymers to intertwine, which results in effective potentials that do not forbid overlaps between effective particles.

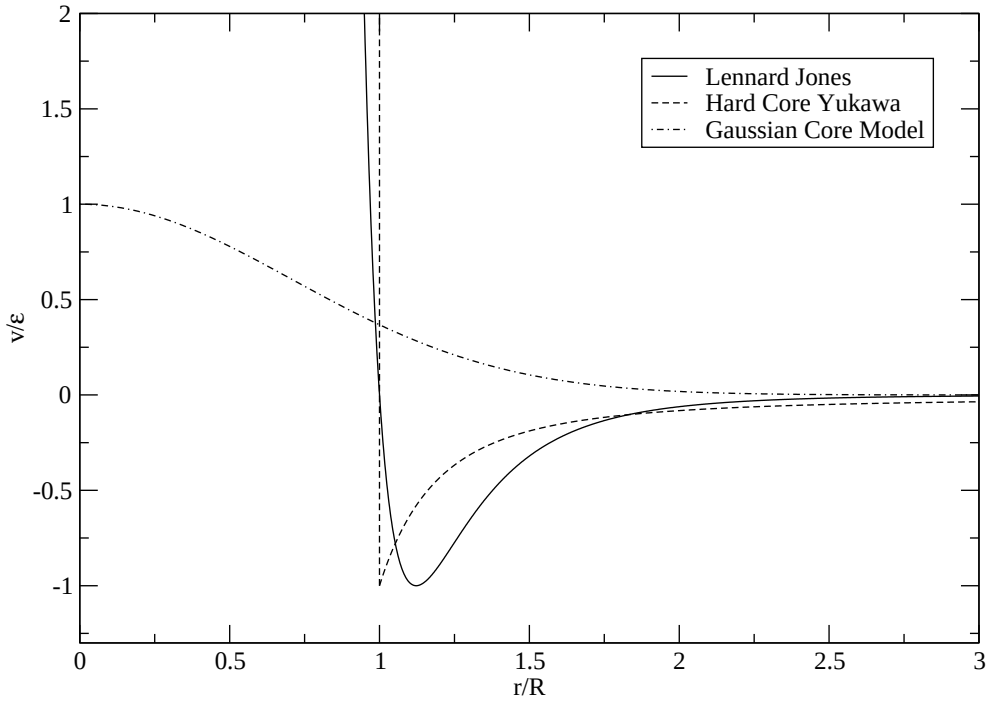

Figure 1.2: Schematic comparison of the Lennard-Jones potential, the hard core Yukawa potential, and a soft model potential, namely the Gaussian Core Model.

The goal of the present work is to analyse the thermodynamic and structural properties of soft model-potentials via a parallel strategy of IETs and computer simulations.

The rest of this thesis is organised as follows: in chapter 2 we give a short overview of statistical mechanics. In chapter 3, at we first present the general idea of IETs and subsequently concentrate on the description of the following theories: the mean spherical, the hypernetted chain, the Percus-Yevick, and the self-consistent Ornstein-Zernike approximation. Next, we discuss the concept of Monte Carlo (MC) simulations, especially for the canonical ensemble. Chapter 4 takes a look at the general properties of soft model potentials and at a criterion to classify them according to their expected thermodynamic behaviour. In this chapter we also present the potentials considered in this thesis, namely the Gaussian core model, the double Gaussian core model and the generalised Gaussian core model with index n. In chapter 5 we turn from theory to practice and explain some "tricks of the trade" in implementing IETs and statistical mechanical simulations on the computer. In chapter 6 we discuss the technical details of our computer programmes and in chapter 7 we present our results for the radial distribution function $g(r)$ and the dimensionless equation of state $\beta P/\varrho$ according to our calculations. In chapter 8, we summarise our results and provide an outlook for expected developments.

Chapter 2

Statistical Mechanics

The aim of statistical mechanics [4, 5] is to provide a mathematical framework to describe the macroscopic thermodynamic properties of a system as predicted by the statistical behaviour of its constituent particles. This concept also allows the calculation of a wide variety of properties not accessible within thermodynamics, such as structural and dynamic properties.

2.1 Basic Concepts

In the present work, the thermodynamic systems under consideration consist of N identical particles enclosed in a volume V and the systems exchange only heat, but no work, mass or momentum with their surroundings, implying that the temperature T of the system is fixed and constant.
The *thermodynamic state* of a system is characterised by the value of a few macroscopic properties, such as pressure P or temperature T. Many other quantities, in turn, are determined by the state of the system. Therefore, it is possible to develop relationships between the various state properties and *equations of state* are examples of some of these expressions: they attempt to describe the dependence of some property of the system such as pressure P on temperature T and density ϱ. For example, the equation of state of an *ideal gas* is given by

$$P = \varrho\, k_{\mathrm{B}} T, \tag{2.1}$$

where

$$\varrho = \frac{N}{V} \tag{2.2}$$

is the number density and $k_{\mathrm{B}} = 1.38065 \times 10^{-23}\,\mathrm{J/K}$ is the Boltzmann constant.
Often, equations of state can be specified as

$$P^{\mathrm{tot}} = P^{\mathrm{id}} + P^{\mathrm{ex}}, \tag{2.3}$$

meaning that the total pressure P^{tot} of the system can be split up into the pressure P^{id} of some idealised reference system, which can easily be calculated, and into an *excess* part P^{ex} that takes into account all contributions to the pressure that stem from additional interactions. Analogously, other thermodynamic properties can be split up in ideal and excess parts.

2.2 The Ensemble

An *ensemble* is a large number of copies of one and the same system, whose microscopic states differ from one another but are compatible with fixed macroscopic parameters which describe the thermodynamic state of the system. Nevertheless, each of those systems is assumed to evolve under the microscopic laws of motion from its initial condition so that the time evolution of each system will be different from all the others. The ensemble concept then states that macroscopic observables can be calculated by performing averages, so-called *ensemble averages*, in the ensemble: let A denote a macroscopic property. Then, the ensemble average of A, denoted as $\langle A \rangle$, is obtained by calculating the value of A in each system of the ensemble and performing an average over all these values:

$$\langle A \rangle = \frac{1}{M} \sum_{i=1}^{M} A_i, \tag{2.4}$$

where M is the number of systems in the ensemble and A_i is the value of A in the i^{th} system.

2.3 The Canonical Ensemble and its Partition Function

The particles of a system are considered to interact by the potential $v(\mathbf{r}_1, ..., \mathbf{r}_N) = v(\mathbf{r}^N)$, where $\{\mathbf{r}_1, ..., \mathbf{r}_N\} =: \mathbf{r}^N$ denote the spatial coordinates of the N particles. The momenta are given by $\{\mathbf{p}_1, ..., \mathbf{p}_N\} =: \mathbf{p}^N$.

A *canonical ensemble* is a collection of systems, each consisting of N particles enclosed in a volume V at constant temperature T. It is therefore sometimes called an NVT-ensemble. To achieve the condition of assigning a fixed value to the temperature, the systems of the ensemble are imagined to have been brought to thermal equilibrium by bringing them into contact with a heat bath of temperature T.

At the heart of statistical mechanics is the *partition function* of the canonical ensemble. In the classical limit it is given by

$$Z(N, V, T) = \frac{h^{-3N}}{N!} \iint e^{-\beta \mathcal{H}(\mathbf{r}^N, \mathbf{p}^N)} \, \mathrm{d}\mathbf{r}^N \mathrm{d}\mathbf{p}^N, \tag{2.5}$$

where $\beta = 1/k_{\mathrm{B}}T$, $\mathcal{H}$ is the system's Hamiltonian, $h = 6.626068 \times 10^{-34}$ Js is the Planck constant and the factor $N!$ accounts for the indistinguishability of the particles.

In quantum mechanics, the partition function can be written as

$$Z(N,V,T) = \sum_i e^{-\beta E_i} \tag{2.6}$$

for systems with non-degenerate eigenvalues. Here, E_i is the i^{th} energy eigenvalue of the system's Hamiltonian operator $\mathcal{H}$ and the sum runs over all those eigenvalues.
The link between statistical mechanics and thermodynamics is established via the relation

$$F = -k_{\text{B}}T \log Z(N,V,T), \tag{2.7}$$

where F is the *Helmholtz free energy*, which is the appropriate *thermodynamic potential* for a system of fixed N, V and T.
If F is a known function of N, V and T, all other thermodynamic state functions can be obtained by differentiation, thus, the free energy or equivalently the partition function contain virtually every information about the macroscopic thermodynamic behaviour of the system.
For instance, it can be shown [1] that

$$U = -\frac{1}{Z}\left(\frac{\partial Z}{\partial \beta}\right)_{V,N} = -\left(\frac{\partial \log Z}{\partial \beta}\right)_{V,N} = \langle \mathcal{H} \rangle, \tag{2.8}$$

where U is the *internal energy*.
Also, properties like the pressure P of the system can be calculated if the partition function or, respectively, the free energy are known:

$$P = k_{\text{B}}T\left(\frac{\partial \log Z}{\partial V}\right)_T = -\left(\frac{\partial F}{\partial V}\right)_T. \tag{2.9}$$

In general, the Hamiltonian $\mathcal{H}$ can be separated into kinetic and potential energy terms: thus, the integration over the momenta in (2.5) can be carried out explicitly. Then, (2.5) can be rewritten as

$$Z(N,V,T) = \frac{\Lambda^{-3N}}{N!}\, z_N(T,V), \tag{2.10}$$

where

$$z_N(V,T) = \int e^{-\beta \Phi(\mathbf{r}^N)}\, \mathrm{d}\mathbf{r}^N \tag{2.11}$$

is the *configurational integral*, $\Phi(\mathbf{r}^N)$ is the total potential energy and

$$\Lambda = \sqrt{\frac{2\pi\beta\hbar^2}{m}} \tag{2.12}$$

is the *de Broglie thermal wavelength*. Here, m is the mass of the particles and

$$\hbar = \frac{h}{2\pi} = 1.05457 \times 10^{-34}\ \text{Js}. \tag{2.13}$$

In the case of the ideal gas, $\Phi(\mathbf{r}^N) = 0$ and $z_N(T,V) = V^N$. Therefore, the partition function of the ideal gas is given by

$$Z^{\mathrm{id}}(N,V,T) = \frac{\Lambda^{-3N}}{N!} V^N. \tag{2.14}$$

Now, the partition function of a system of interacting particles can be written as

$$Z(N,T,V) = Z^{\mathrm{id}} \frac{z_N(V,T)}{V^N}. \tag{2.15}$$

On taking the logarithm of both sides of this equation, the free energy naturally separates into an ideal and an excess part

$$F = F^{\mathrm{id}} + F^{\mathrm{ex}} \tag{2.16}$$

and thus affirms the concept of ideal/excess parts of thermodynamic quantities already discussed earlier (see section 2.3).
Using Stirling's approximation for large N

$$\log N! \sim N \log N - N, \tag{2.17}$$

F^{id} is given by

$$\frac{\beta F^{\mathrm{id}}}{N} = \log \varrho + 3 \log \Lambda - 1 \tag{2.18}$$

and the excess part F^{ex} of the free energy is

$$F^{\mathrm{ex}} = -k_{\mathrm{B}} T \log \frac{z_N(V,T)}{V^N}. \tag{2.19}$$

Analogously, the internal energy can be separated

$$U = U^{\mathrm{id}} + U^{\mathrm{ex}}, \tag{2.20}$$

where $U^{\mathrm{id}} = \frac{3}{2} N k_{\mathrm{B}} T$ and

$$U^{\mathrm{ex}} = \frac{1}{z_N(T,V)} \int \Phi(\mathbf{r}^N) e^{-\beta \Phi(\mathbf{r}^N)} \, \mathrm{d}\mathbf{r}^N = \langle \Phi \rangle. \tag{2.21}$$

Chapter 3

Methods

In the quest of determining the properties of a fluid, at first, one has to assume a model interaction potential between the constituent particles of the liquid. Then, the thermodynamics of this model fluid can be determined via concepts based on statistical mechanics; the most commonly used approximations are classical computer simulation techniques or liquid state theories.
Computer simulations provide for a given model potential virtually exact results for structural and thermodynamic quantities, superposed with a statistical error essentially due to the use of a finite number of particles and finite simulation length. Unfortunately, calculations can require considerable computational resources (i.e. time and memory) and modelling a fluid in a simulation box can be tedious, problematic and highly biased by finite size and surface effects [6].
As already discussed in chapter 2, all thermodynamic properties relevant for the description of the fluid can also be determined by means of equilibrium statistical mechanics if the partition function Z is known. This function is related to the interparticle potential by relations which cannot be used directly. Therefore, approximations have to be invoked to solve the problem and this is the point where liquid state theories, i.e. integral equation theories (IETs) and thermodynamic perturbation theories tie in.
These theories introduce a certain degree of approximation in the description of the properties of the model fluid compared to the quasi-exact computer simulations. Therefore, results for structural and thermodynamic properties obtained by these theories have to be assessed against the corresponding results provided by simulations. Still, computer simulations are limited to systems of finite size, while IETs treat systems at the thermodynamic limit. Though in most cases results can only be obtained numerically which requires the use of spatial grids, the grid size is in general by far larger than typical simulation box sizes. Furthermore, such numerical calculations need in general significantly less computational resources (in particular time) than comparably accurate simulations.

3.1 Integral Equation Theories

3.1.1 The Radial Distribution Function

For a fluid consisting of N particles in a volume V at temperature T, the *two-particle distribution function* is defined as

$$g_N(\mathbf{r}_1, \mathbf{r}_2) = \frac{1}{z_N} V^2 \int ... \int e^{-\beta \Phi(\mathbf{r}^N)} \, \mathrm{d}\mathbf{r}_3 ... \mathrm{d}\mathbf{r}_N, \tag{3.1}$$

where $\Phi(\mathbf{r}^N)$ is the total potential energy of the system and $z_N(V,T)$ is the *configurational integral* given by (2.11).
$g_N(\mathbf{r}_1, \mathbf{r}_2)\mathrm{d}\mathbf{r}_1\mathrm{d}\mathbf{r}_2$ is a measure for the probability to find particle 1 in a volume $\mathrm{d}\mathbf{r}_1$ at $\mathbf{r}_1$ and particle 2 in a volume $\mathrm{d}\mathbf{r}_2$ at $\mathbf{r}_2$, disregarding the positions of the other $N-2$ particles of the system. Therefore, $g_N \to 1 - \frac{1}{N}$ as the distance between the two particles tends to infinity and $g_N \to 1$ for $r \to \infty$ and $N \to \infty$. This limiting value expresses the loss of correlation between the particles at large distances.
For an isotropic and homogeneous system, $g(\mathbf{r}_1, \mathbf{r}_2)$ only depends on the distance $|\mathbf{r}_1 - \mathbf{r}_2| = r$:

$$g(\mathbf{r}_1, \mathbf{r}_2) = g(r). \tag{3.2}$$

$g(r)$ is called *radial distribution function* and is proportional to the probability of finding a particle of the fluid at distance r from a given particle.

3.1.2 Thermodynamic Properties

Given the case that all particles interact only by means of central pair forces $v(r)$ for which the total potential energy can be written as

$$\Phi(\mathbf{r}^N) = \frac{1}{2} \sum_{i \neq j} v(r_{ij}), \tag{3.3}$$

where $r_{ij} = |\mathbf{r}_i - \mathbf{r}_j|$ and $i, j = 1, ..., N$, most pair properties of the system, such as the pressure P, can be expressed by means of $g(r)$.
This leads to one possible formulation of the equation of state

$$\frac{\beta P}{\varrho} = 1 - \frac{2\pi}{3} \beta \varrho \int g(r) \, r^2 \left(r \frac{d}{dr} v(r) \right) \mathrm{d}r, \tag{3.4}$$

where ϱ is given by (2.2). As equation (3.4) determines the pressure in terms of an ensemble average of the virial, it is called *virial equation.*
In this work, two other routes to obtain the pressure of the system will be used. The first one is

called *energy route*. According to (2.9), the excess pressure P^{ex} is given by

$$P^{\mathrm{ex}} = -\left(\frac{\partial F^{\mathrm{ex}}}{\partial V}\right)_T. \tag{3.5}$$

F^{ex} is the excess free energy, which reads as

$$\frac{\beta F^{\mathrm{ex}}}{N}(\varrho) = \int_0^\beta \frac{U^{\mathrm{ex}}}{N}(\beta', \varrho)\ \mathrm{d}\beta'; \tag{3.6}$$

the integral is evaluated along an isochoric path. U^{ex} is the excess internal energy and is related to $g(r)$ via

$$\frac{U^{\mathrm{ex}}}{N} = 2\pi\varrho \int g(r)\, v(r)\, r^2\ \mathrm{d}r. \tag{3.7}$$

Thermodynamic fluctuation theory yields the so-called *compressibility equation*[1], where the isothermal compressibility κ_T of the system is obtained by

$$1 + \varrho \int [g(\mathbf{r}) - 1]\, \mathrm{d}\mathbf{r} = \varrho\, k_{\mathrm{B}} T \kappa_T. \tag{3.8}$$

The pressure of the system is then determined by

$$\kappa_T = -\frac{1}{V}\left(\frac{\partial V}{\partial P}\right)_T = \left[\varrho\left(\frac{\partial P}{\partial \varrho}\right)_T\right]^{-1}. \tag{3.9}$$

If the true $g(r)$ of the system could be calculated with some method, the virial, compressibility and energy routes would yield the same value for the pressure; then this method would be called *thermodynamically consistent*.

IETs of $g(r)$ in general give - as a consequence of the simplifying assumptions introduced - only approximate estimates for the radial distribution function; hence, they are thermodynamically inconsistent, i.e. the three routes to determine the pressure provide different results.

3.1.3 The Ornstein-Zernike Equation

The *total pair correlation function* $h(r)$ is defined as

$$h(r) = g(r) - 1. \tag{3.10}$$

So as $g(r) \to 1$, $h(r) \to 0$.

The *structure factor* $S(\mathbf{k})$, which can be obtained experimentally by measurements of the cross-section for scattering of neutrons and X-rays as a function of the scattering angle, is connected to

[1] Unlike the pressure and energy equations, this equation is also valid in systems where the interparticle forces are not pairwise additive.

the pair correlation function in a very basic way

$$S(\mathbf{k}) = 1 + \varrho\hat{h}(\mathbf{k}), \tag{3.11}$$

where

$$\hat{h}(\mathbf{k}) = \int h(\mathbf{r})e^{-i\mathbf{r}\mathbf{k}}\ \mathrm{d}\mathbf{r} \tag{3.12}$$

denotes the Fourier transform of $h(r)$ (see appendix A).
Ornstein and Zernike [7] introduced in a heuristic way a function, called *direct correlation function* $c(r)$, which they related to the total correlation function in the following way:

$$h(\mathbf{r}) = c(\mathbf{r}) + \varrho \int c(|\mathbf{r} - \mathbf{r}'|)\, h(\mathbf{r}')\ \mathrm{d}\mathbf{r}'. \tag{3.13}$$

This equation is valid for translationally invariant and isotropic fluids and is called *Ornstein-Zernike equation* (OZE). The Fourier transform of this equation leads to

$$\hat{h}(\mathbf{k}) = \frac{\hat{c}(\mathbf{k})}{1 - \varrho\,\hat{c}(\mathbf{k})}, \tag{3.14}$$

where $\hat{c}(\mathbf{k})$ is obtained similarly to (3.12).
$h(\mathbf{r})$ can be expressed formally by iteratively inserting the OZE:

$$h(\mathbf{r}) = c(\mathbf{r}) + \varrho \int c(|\mathbf{r} - \mathbf{r}'|)\, c(\mathbf{r}')\ \mathrm{d}\mathbf{r}' + \varrho^2 \iint c(|\mathbf{r} - \mathbf{r}'|)\, c(|\mathbf{r}' - \mathbf{r}''|)\, c(\mathbf{r}'')\ \mathrm{d}\mathbf{r}'\mathrm{d}\mathbf{r}'' + \ldots\ . \tag{3.15}$$

The formal structure of (3.15) points out a possible interpretation of the OZE: the total correlation between two particles in the fluid separated by a distance r is the sum of the direct correlation between those two particles plus the indirect correlations mediated by $c(\mathbf{r})$ through an increasing number of many body correlations over the rest of the fluid.
The pair and direct correlation function are amenable to a systematic analysis in terms of configurational integrals over clusters of particles, known as *cluster expansion*. By this, it can be shown that

$$g(r) = e^{-\beta v(r) + h(r) - c(r) + B(r)}, \tag{3.16}$$

where the *bridge function* $B(r)$ is the sum of an infinite number of terms, each consisting of integrals whose kernels are products (of increasing order) of correlation functions and simple functions of the potential. The exact $B(r)$ is not known for any system.
IETs arise from the joint use of the OZE and equation (3.16): these two equations involve three unknown functions, namely $h(r)$ [or equivalently $g(r)$], $c(r)$ and $B(r)$. Different strategies are used to cope with this underdetermined problem: some IETs introduce approximations for $B(r)$ and (3.16) is used as a *closure* to the OZE. Thus, $h(r)$ and $c(r)$ can be determined by solving a non-linear integral equation in one of these two functions. Other IETs have been formulated by starting from an approximate ansatz for $h(r)$ or $c(r)$ rather than from an estimate for $B(r)$. In

the following we will briefly present the IETs used in this thesis.

3.1.4 The Mean Spherical Approximation

The *mean spherical approximation* (MSA) was first proposed by Lebowitz and Percus in 1966 [8] as a generalisation of the mean-spherical model of the Ising Spin systems. Usually, the MSA is used for fluids for which the pair potential consists of a hard-sphere interaction

$$v(r) = \infty \quad \text{for} \quad r < R, \tag{3.17}$$

plus a "tail" which can take different functional forms for $r > R$, where R denotes the hard core diameter. For such potentials, the MSA is formulated in terms of an ansatz for the direct correlation function:

$$c(r) = -\beta v(r) \quad \text{for} \quad r > R \tag{3.18}$$

and

$$g(r) = 0 \quad \text{for} \quad r < R. \tag{3.19}$$

This relation is called *core condition* and expresses the impenetrability of the particles.
Soft potentials as those used in this thesis lack the presence of a hard core; so for such systems the MSA reduces to

$$c(r) = -\beta v(r) \quad \forall r \tag{3.20}$$

and is sometimes also called *random phase approximation* (RPA). When supplemented by the OZE, (3.18) and (3.19) resp. (3.20) yield an integral equation for g(r).
Using cluster expansion analysis of $c(r)$, it can be generally shown that

$$c(r) \cong -\beta v(r) \quad \text{for} \quad r \to \infty. \tag{3.21}$$

Thus, the MSA is correct in the limit $r \to \infty$ and can be considered to extend the realm of validity of (3.21) to short distances.
Despite the simple form assumed for $c(r)$, the MSA gives good results for many model systems. However, the most attractive feature of the MSA is the fact that it can be solved analytically for a number of model potentials of physical interest, including the hard core Yukawa-potential, the charged hard sphere and the adhesive hard sphere model [1]. On the other hand, the MSA suffers from some deficiencies, such as that in the case of soft potentials it can yield negative values of $g(r)$ at low densities (see section 7.1), which is unphysical.[2]

[2] This does not occur in the case of hard core potentials, as such a behaviour is explicitly forbidden by (3.19).

3.1.5 The Hypernetted-chain Approximation

Under the assumption

$$B(r) = 0, \tag{3.22}$$

(3.16) becomes

$$g(r) = e^{-\beta v(r)+h(r)-c(r)}. \tag{3.23}$$

This is equivalent to

$$c(r) = -\beta v(r) + h(r) - \log[h(r) + 1]. \tag{3.24}$$

This is the so-called *hypernetted-chain approximation* (HNC) [9]. In contrast to the MSA, which can be solved analytically for some potentials, the HNC must be solved numerically in any case. The HNC approximation provides satisfactory results for bounded potentials and for long-ranged interactions, such as the Coulomb potential.

3.1.6 The Percus-Yevick Approximation

The *Percus-Yevick approximation* (PY), proposed in 1958 by Percus and Yevick [10], assumes that

$$c(r) = \left[1 - e^{\beta v(r)}\right] g(r), \tag{3.25}$$

so that $c(r)$ equals zero wherever the potential vanishes.
In this case, the radial distribution function is given by

$$g(r) = e^{-\beta v(r)}[1 + h(r) - c(r)]. \tag{3.26}$$

Expanding the expression (3.23) with respect to $[h(r) - c(r)]$ up to the first order gives

$$\begin{aligned} g(r) &= e^{-\beta v(r)+h(r)-c(r)} = \\ &= e^{-\beta v(r)} e^{h(r)-c(r)} = \\ &= e^{-\beta v(r)}[1 + h(r) - c(r)]. \end{aligned} \tag{3.27}$$

Thus, the PY approximation is attained by linearising the HNC closure. A cluster analysis of both closures shows that the HNC approximation is obtained by summing up a higher number of terms than the PY closure. In most cases, the solution of (3.25) and the OZE has to be found numerically, but in some cases, e.g. for the hard sphere fluid or for adhesive hard spheres, it can be obtained analytically [1].
Considering short-ranged, repulsive potentials, the PY equation is very successful. Its greater success for this kind of potentials in contrast to other conventional IETs might be due to some extent to the cancellation of errors while summing up the terms of the cluster expansion. On the other side, the PY approximation is usually not a good choice for soft potentials.

3.1.7 The Self-consistent Ornstein-Zernike Approximation

In 1984, Høye and Stell [11] proposed a more "sophisticated" IET, the *self-consistent Ornstein-Zernike approximation* (SCOZA) which belongs to the class of the *advanced IETs*. Its idea is to impose thermodynamic consistency between (at least) two thermodynamic routes that were already discussed in section 3.1.2.
As the SCOZA enforces equality in isothermal compressibility or resp. pressure, one could assume that this self-consistent theory is also 'exact' at the structural level, i.e. that one finds the exact $g(r)$. However, we find that for some states of the GCM - just like the MSA for low densities - the radial distribution function is unphysical, i.e. negative. This contradiction can be understood, as the pressure is only obtained by *integrating* over $g(r)$ [see (3.4)], where the particular slope and eventual negative values can play a minor role.
In the present work, we enforce the equality of the isothermal compressibilities as calculated according to the virial and the compressibility route:

$$\left(\beta\frac{\partial P^{\text{vir}}}{\partial \varrho}\right)_T = 1 - \varrho\,\hat{c}(k=0). \tag{3.28}$$

In the SCOZA, a closure is obtained by assuming that

$$\begin{cases} g(r) = 0 & r < R \\ c(r) = K(\beta,\varrho)\,v(r) & r > R \end{cases} \tag{3.29}$$

in the case of hard core potentials, respectively

$$c(r) = K(\beta,\varrho)\,v(r) \qquad \forall r \tag{3.30}$$

for soft core potentials, where $K(\beta,\varrho)$ is the sought-after function that enforces thermodynamic consistency as described in (3.28).
To the author's knowledge, up to now the SCOZA has only been solved for hard core Yukawa fluids and lattice gases [12, 13, 14, 15].

3.2 Monte Carlo Simulations

If a theory that provides an approximate description of the fluid of interest is tested by direct comparison to an experiment, one is faced by the problem that the knowledge of the intermolecular interactions is limited, so disagreement between theory and experiment means that either the theory is wrong or that the assumptions on the intermolecular interactions are inadequate - or even both.
Computer simulations represent the missing tool in-between theory and experiment. They allow one to obtain essentially exact results for a given model system without having to rely on approx-

imate theories. They do not only provide the possibility to compare calculated properties of a model system to those of an experimental system, but also to compare the results of simulations with those of an approximate theory such as IETs or perturbation theories applied to the same model. If the results disagree in the first case, this means that the model is inadequate and that the estimate of the nature of the intermolecular interactions has to be improved. In the second case, the computer simulation plays the role of the experiment designed to test the theory, so in this case disagreement means that the theory is flawed. These are the main reasons why computer simulations are of tremendous importance.
MC methods [6, 16, 17, 18] were invented in the forties in Los Alamos in the course of the construction of the atomic bomb. Basically, these algorithms use random numbers to solve numerical problems which can be described by stochastic processes. Therefore, MC methods are not limited to simulations of thermodynamic systems, but are applied to a wide range of problems such as for instance the determination of high-dimensional integrals.

3.2.1 The Master Equation

A system consisting of N particles enclosed in a simulation box of volume V and surrounded by a reservoir of a given temperature T, is assumed to be in a state μ characterised by the configuration of the particles. The probability that the system will be in state ν at time span $\mathrm{d}t$ later is denoted as $P(\mu \to \nu)\,\mathrm{d}t$. By means of statistical mechanics it is possible to define a transition probability for every state that the system can reach.
Assuming that $\{w_\mu(t)\}$ is a set of weights which represent the probability that the system will be in state μ at time t, we can write a *master equation* for the time-evolution of $w_\mu(t)$

$$\frac{\mathrm{d}w_\mu}{\mathrm{d}t} = \sum_\nu \left[w_\nu(t)P(\nu \to \mu) - w_\mu(t)P(\mu \to \nu)\right]. \tag{3.31}$$

The first term on the right hand side describes transitions of the systems *into* state μ, whereas the second one describes transitions *out of* state μ into other states. The probabilities $w_\mu(t)$ must also obey the sum rule

$$\sum_\mu w_\mu(t) = 1 \qquad \forall t, \tag{3.32}$$

since the system must be in *some* state at any time.
The *ensemble average* $\langle A\rangle$ of an arbitrary macroscopic property A of the system is calculated with the help of the weights according to

$$\langle A\rangle_t = \sum_\mu A_\mu w_\mu(t), \tag{3.33}$$

where A_μ is the value that A takes in state μ.[3] The relation between $\langle A \rangle$ and the observed value of A can be interpreted as follows: assuming a very large number of copies of the system of interest, $\langle A \rangle$ is an estimate for the mean value of A measured in all systems simultaneously.

3.2.2 Equilibrium

In the *equilibrium state*, the weights $\{w_\mu(t)\}$ will take constant values, which implies that the derivative $\mathrm{d}w_\mu(t)/\mathrm{d}t = 0$ for all times. Considering (3.31), one possibility that $\mathrm{d}w_\mu(t)/\mathrm{d}t$ vanishes is that for fixed μ

$$w_\nu(t)P(\nu \to \mu) - w_\mu(t)P(\mu \to \nu) = 0 \qquad \forall \nu. \tag{3.34}$$

It is assumed that the weights $\{w_\mu(t)\}$ converge towards an equilibrium distribution. These *time-independent* values of $\{w_\mu(t)\}$ are called *equilibrium occupation probabilities* and are defined by

$$p_\mu = \lim_{t \to \infty} w_\mu(t). \tag{3.35}$$

Gibbs [19] showed that for a canonical ensemble

$$p_\mu = \frac{1}{Z} e^{-\beta E_\mu}, \tag{3.36}$$

where E_μ is the energy of state μ and Z is the *partition function* defined by (2.6).
The probability function in (3.36) is known as the *Boltzmann distribution*. According to (3.33), (3.35) and (3.36), the expectation value, i.e. the ensemble average for a macroscopic quantity A of the system is

$$\langle A \rangle = \frac{1}{Z} \sum_\mu A_\mu e^{-\beta E_\mu}. \tag{3.37}$$

For instance, the expectation value of the energy,

$$U = \langle E \rangle = \frac{1}{Z} \sum_\mu E_\mu e^{-\beta E_\mu}, \tag{3.38}$$

is the internal energy U.

3.2.3 The Simulations

MC simulations create a model system on the computer and make it pass through a variety of states in such a way that the probability of being in state μ is equal to p_μ. To achieve this, the rules for changing from one state to another during the simulation have to be chosen so that the equilibrium solution to the corresponding master equation is precisely the Boltzmann distribution

[3] (2.4) and (3.33) are equivalent. Whereas in (2.4) the average is taken over all different systems in the ensemble, here, the average is taken over different, weighted *states*.

(3.36). These probabilities are then used to select the states which the system passes through during the course of the simulation.
The advantage about this technique is that only relatively few representative states but not all possible states have to be sampled to gather good estimates of physical quantities of the system. As a consequence of the limited number of states in this simulating procedure, resulting functions are superimposed by a statistical noise, which is one main disadvantage of this approach: taking derivatives of noisy functions is problematic, so that calculating expectation values from e.g. derivatives of Z as discussed in section 2.3 is not a good way to proceed. Instead, it is common to calculate as many quantities directly via expectation values as possible. For instance, the pressure P can be calculated via the virial W

$$\langle P \rangle = \frac{\varrho}{\beta} - \frac{\langle W \rangle}{3V}, \tag{3.39}$$

where the virial W is defined by

$$W = \sum_{i<j} r_{ij} \frac{\partial v(r)}{\partial r}\Big|_{r=r_{ij}}. \tag{3.40}$$

3.2.4 The Estimator

Basically, the usual goal in the MC simulation of a system is the calculation of the ensemble average $\langle A \rangle$ given by (3.33) of some observable quantity A. The ideal route of calculating such an expectation value - that of averaging the weighted quantity of interest over all states μ of the system - is only tractable in extremely small systems. In larger systems, one is forced to average over some subset of the states, though this necessarily introduces some inaccuracy into the calculation. MC techniques work by choosing a subset of states at random from the probability function p_μ. Supposing that the system has passed M such states $\{\mu_1, ..., \mu_M\}$ during the course of the simulation, the *estimator* A_M for the quantity A is simply given as the mean value of the values of A in the different sampled states:

$$A_M = \frac{1}{M} \sum_{i=1}^{M} A_{\mu_i}. \tag{3.41}$$

As the number M of states sampled increases, A_M becomes more and more accurate and when $M \to \infty$, then $A_M = \langle A \rangle$.
Consequently, it is decisive to find an algorithm that effectively samples states according to the probability distribution p_μ.

3.2.5 Importance Sampling

Importance sampling techniques [17, 18] choose random numbers from the probability distribution p_μ, which allows the evaluation of A to be concentrated on those states that make important

contributions to (3.41). Then, the simulated system will mainly be in a rather small but representative number of states and the relative frequency with which a state is chosen corresponds to the amount of time a real system would spend in this state.
Still, the problem of finding an algorithm that samples the states according to the probability distribution p_μ has only been rephrased, not solved. The main problem is finding a method of generating a sequence of states so that by the end of the simulation each state has occurred with the appropriate probability. The standard solution for this problem is to use a *Markov process* [6, 16, 17].

3.2.6 Markov Processes

One way to generate an appropriate set of states according to the Boltzmann distribution (3.36) would be to choose states at random and accept or reject them with a probability $\exp(-\beta E_\mu)$. This is a very slow algorithm. In the end, nearly all configurations would be rejected since the probability for their acceptance would be exponentially small. So instead, a *Markov process* [18, 20, 21] is used. This mechanism generates a new state ν of the system from a given system state μ in a random fashion. The probability of generating the state ν from a given μ is called *transition probability* $P(\mu \to \nu)$ and for a Markov process all transition probabilities have to satisfy three criteria:

- First, they should not vary over time.
- Second, they should depend only on the properties of the current states μ and ν and not on any other states the system has passed through.
- Third, they have to satisfy the *sum rule*

$$\sum_\nu P(\mu \to \nu) = 1, \tag{3.42}$$

  since the Markov process has to produce *some* state ν when the system is in state μ.

It is important to emphasise that the probability $P(\mu \to \mu)$, i.e. the probability that the system will stay in the state it is in, does not need to be zero.
MC simulations use a Markov process repeatedly to generate a *Markov chain* of states. The Markov process itself is chosen in a way that, when it is run sufficiently long starting from an arbitrary state of the system, it will come to equilibrium and will then produce a sequence of states which appear with the probabilities given by the Boltzmann distribution. To achieve this, the Markov process has to fulfill two conditions, the conditions of *ergodicity* and of *detailed balance*.

3.2.7 Ergodicity

The *condition of ergodicity* is the requirement that the Markov process has to be able to reach any state of the system from any other state in a finite number of steps. Every state ν appears with

some non-zero probability in the Boltzmann distribution and if that state were inaccessible from another state μ no matter how long the Markov process is continued for, then the probability of finding state ν in the simulation will be equal to zero, and not p_ν, as required. Consequently, the sampled states would follow a wrong distribution function. The condition of ergodicity does not prohibit some of the transition probabilities in the Markov process to be equal to zero, as long as there is always at least one path of non-zero transition probabilities between any arbitrary states μ and ν.

3.2.8 Detailed Balance

The *condition of detailed balance* is the second condition imposed on the Markov process and it ensures that it is the Boltzmann distribution which is generated after the system has come to equilibrium.
The definition of *equilibrium* is that the rate at which the system makes transitions out of a given state μ must be equal to the number of transitions into that state:

$$\sum_\nu p_\mu P(\mu \to \nu) = \sum_\nu p_\nu P(\nu \to \mu). \tag{3.43}$$

Using (3.42), (3.43) simplifies to

$$p_\mu = \sum_\nu p_\nu P(\nu \to \mu). \tag{3.44}$$

Usually, an even stronger criterion, the *condition of detailed balance* is imposed on the transition probabilities

$$p_\mu P(\mu \to \nu) = p_\nu P(\nu \to \mu), \tag{3.45}$$

which ensures that on average the system should go from state μ to ν just as often as from ν to μ. If the chosen Markov process fulfills (3.45), then the probability distribution of the states tends to the Boltzmann distribution p_μ and (3.45) becomes

$$\frac{P(\mu \to \nu)}{P(\nu \to \mu)} = \frac{p_\nu}{p_\mu} = e^{-\beta(E_\nu - E_\mu)}. \tag{3.46}$$

This equation along with (3.42) are the constraints imposed on the transition probabilities $P(\mu \to \nu)$. If they are satisfied, as well as the condition of ergodicity, then the equilibrium distribution of states of the Markov process will be the Boltzmann distribution.

3.2.9 Acceptance Ratios

There are several possibilities to choose the transition probabilities $P(\mu \to \nu)$, which have not yet been fixed, as long as (3.42) and (3.45) are fulfilled. As it would be very complicated to elaborate an algorithm for a Markov process that directly generates the correct transition ratios,

the following trick is used.

At first, consider the probability that the system stays in the state it is in at the moment. If $\nu = \mu$ in (3.45), the equation simplifies to the simple tautology $1 = 1$, i.e. the condition of detailed balance is always satisfied for every $P(\mu \to \mu)$, no matter which value it takes. Furthermore, even if $P(\mu \to \nu)$ and $P(\nu \to \mu)$ are adjusted, the condition of detailed balance is still satisfied as long as the original ratio $\frac{P(\mu \to \nu)}{P(\nu \to \mu)}$ is preserved. As the simulation itself only depends upon this ratio, the transition probabilities do not even have to be normalised, so they are allowed to violate the sum rule (3.42). In a next step, the transition probabilities are split into two factors

$$P(\mu \to \nu) = s(\mu \to \nu)\, a(\mu \to \nu), \tag{3.47}$$

where $s(\mu \to \nu)$ denotes the *selection probability*, i.e. the probability, given an initial state μ, that the algorithm generates a new state ν, and $a(\mu \to \nu)$ is the *acceptance ratio*, which indicates the probability with which the change from μ to ν will be accepted as a new state. If this so-called *trial move* is not accepted, the system will stay in μ.

With (3.47), (3.45) now becomes

$$\frac{P(\mu \to \nu)}{P(\nu \to \mu)} = \frac{s(\mu \to \nu)\, a(\mu \to \nu)}{s(\nu \to \mu)\, a(\nu \to \mu)}. \tag{3.48}$$

The acceptance ratio can be chosen as an arbitrary number between 0 and 1, so the ratio $\frac{a(\mu \to \nu)}{a(\nu \to \mu)}$ can take any positive value, which means that according to (3.48) both $s(\mu \to \nu)$ and $s(\nu \to \mu)$ can take any positive value desired.

The trick is to develop an algorithm that generates random new states ν, given a state μ, with a set of probabilities $s(\mu \to \nu)$ and then to accept or reject those states with acceptance ratios $a(\mu \to \nu)$, which are chosen in a way that (3.48) is satisfied.

If the acceptance ratios are low, then the algorithm will stay in the state it is in for several moves as new moves are rejected most of the time and the simulation will proceed slowly. As it is desired for the algorithm to move swiftly about phase space and sample a wide selection of states in a representative time span, acceptance ratios are chosen to be as close to unity as possible. (3.48) fixes only the ratio $\frac{a(\mu \to \nu)}{a(\nu \to \mu)}$ of the acceptance ratios for the transitions in either direction between any two states. Thus, it is allowed to multiply both $a(\mu \to \nu)$ and $a(\nu \to \mu)$ by the same factor and (3.48) is still fulfilled. The only constraint is that both acceptance ratios remain between 0 and 1. In practice, the larger one of those two acceptance ratios is often set to 1 while the other one takes the required value in order to satisfy the condition of detailed balance. This ensures that the acceptance ratios will be as large as possible while still fulfilling the relevant conditions, and that at least for one direction of changing from state μ to ν (respectively vice versa), moves will always be accepted. This is called *asymmetric rule*.[4]

[4] Symmetric rules, where $a(\mu \to \nu) = a(\nu \to \mu) \neq 1$, are usually used in the simulation of spin systems.

3.2.10 Metropolis Monte Carlo

In 1953, Metropolis *et al.* proposed an algorithm [22] to speed up MC simulations making use of the tricks discussed before. In their algorithm, the selection probabilities $s(\mu \to \nu)$ for each of the possible states ν that can be reached from state μ are chosen to be equal. The selection probabilities for all other states are set to zero. This is done in the following way:
At first, the N particles of the modelled system are placed in an arbitrary configuration within a cubic box of length L. Then, each of the particles is moved in succession or randomly according to

$$\mathbf{r}_i \to \mathbf{r}_i + \Delta\boldsymbol{\xi}_i \qquad i = 1, ..., N \tag{3.49}$$

where Δ is the maximum allowed displacement, which is arbitrary within the constraint $\Delta < \frac{L}{2}$, and the $\boldsymbol{\xi}_i$ are vectors of random numbers between -1 and 1. After a move, the particle is equally likely to be anywhere in a cube of side 2Δ centred around its original position.
Since a particle is allowed to move to any point within this cube with a finite probability, it is clear that it can reach any point of the box if the number of moves is large enough. Since this is true for all particles, the system is able to reach every possible point in configuration space. Hence, the method is ergodic.
As $s(\mu \to \nu) = s(\nu \to \mu)$, (3.46) and (3.48) simplify to

$$\frac{P(\mu \to \nu)}{P(\nu \to \mu)} = \frac{s(\mu \to \nu)\, a(\mu \to \nu)}{s(\nu \to \mu)\, a(\nu \to \mu)} = \frac{a(\mu \to \nu)}{a(\nu \to \mu)} = e^{-\beta(E_\nu - E_\mu)}. \tag{3.50}$$

To choose the acceptance ratios $a(\mu \to \nu)$, the change in energy $\Delta E = E_\nu - E_\mu$ of the system caused by the displacement of the particle is calculated. If $\Delta E < 0$, i.e. if the energy of the system is lower than before, the trial move is accepted and the particle is placed at its new coordinates. On the other hand, if $\Delta E > 0$, the trial move is allowed with a probability of $\exp(-\beta\Delta E)$. To achieve this, a random number $\hat{\xi}$ between 0 and 1 is generated, and if $\hat{\xi} > \exp(-\beta\Delta E)$ the particle remains at its old position, while it is moved to the new coordinates if $\hat{\xi} < \exp(-\beta\Delta E)$ (see figure 3.1). No matter if the new configuration has been accepted or not, i.e. the system is still in the old configuration, we consider it to be in a new configuration for the purpose of taking our averages according to (3.41). After this attempted move, the procedure is repeated with the next particle and so forth, generating a *random walk* through phase space.
To summarise, the algorithm chooses the acceptance ratios to be

$$a(\mu \to \nu) = \begin{cases} e^{-\beta(E_\nu - E_\mu)} & \text{if } E_\nu - E_\mu = -\Delta E > 0 \\ 1 & \text{otherwise.} \end{cases} \tag{3.51}$$

Since (3.51) satisfies the condition of detailed balance (3.48), the Metropolis algorithm generates states according to the Boltzmann distribution function. As it is a very efficient algorithm, it has become *the* algorithm of choice in the majority of MC studies of simple statistical models.

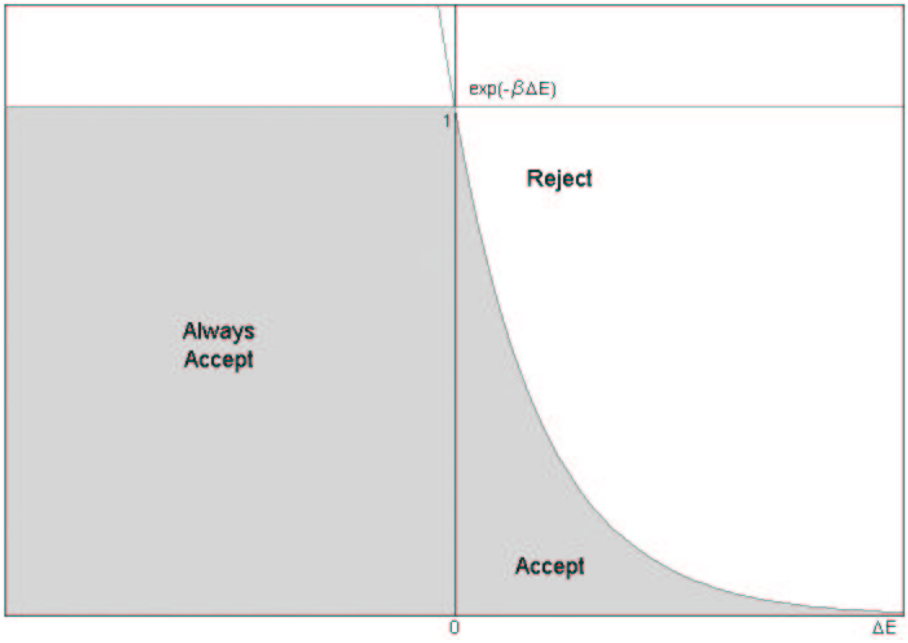

Figure 3.1: Acceptance ratios in the Metropolis MC simulation. Moves with $\Delta E < 0$ are always accepted. For $\Delta E > 0$, moves get accepted if $\hat{\xi} \leq \exp(-\beta \Delta E)$ and rejected for $\hat{\xi} > \exp(-\beta \Delta E)$, where $\hat{\xi}$ is a random number.

Chapter 4

Systems

4.1 System Parameters

In this thesis, we consider one-component systems, i.e. systems with only one species of particles that interact via radially symmetric and density independent pair-potentials $v(\mathbf{r}) = v(r)$. For the liquid and gas phase we consider the systems to be homogeneous and isotropic, i.e. the mean density is constant for every point in space. Solid phases are not considered in this thesis.
For a system consisting of N particles enclosed in a volume V, the number density ϱ is defined by (2.2). The *reduced dimensionless number density* ϱ^* is defined as

$$\varrho^* = \frac{N}{V} R^3, \tag{4.1}$$

where R is the length-scale which characterises the potential. The energy scale that delineates the potential is called ε. The *reduced dimensionless temperature* T^* is defined via ε according to

$$T^* = \frac{1}{\beta\varepsilon} = \frac{k_\mathrm{B}T}{\varepsilon} = \frac{1}{\varepsilon^*}, \tag{4.2}$$

where ε^* is the *reduced dimensionless energy* $\varepsilon^* = \beta\varepsilon$.

4.2 Soft Potentials

The task of calculating the thermodynamics of systems consisting of macromolecules, such as linear polymers, dendrimers, star polymers et cetera, is a formidable one as the constituent macromolecules may contain thousands or even millions of atoms interconnected with one another in complicated ways. Determining for instance such a system's free energy by taking into account all individual interactions rapidly becomes intractable. However, making use of a *coarse-graining* procedure [23], which amounts to averaging out certain degrees of freedom, considerable progress can be made. In the first step, instead of attempting to calculate a system's thermodynamic prop-

erties by taking into account the coordinates of all the individual monomers, suitable effective coordinates - as for instance the centre of mass of the macromolecule - are introduced and the macromolecules are substituted by effective point particles. Next, the average of the interaction between all monomers belonging to the macromolecule is taken for a given fixed configuration of the effective coordinates, which defines an *effective interaction* between those coordinates. Now, the macroscopic system is regarded as consisting of point particles interacting by means of this *effective potential* (see figure 1.1) and thermodynamic quantities can be investigated using the well known tools from the theory of atomic and simple molecular fluids.
As the centres of mass of two polymer chains can coincide without any of the monomers violating the excluded volume conditions, i.e. without sitting on top of each other, the coarse-graining procedure gives rise to a new class of potentials called soft potentials, whose main feature is that they remain finite or diverge only very slowly as $r \to 0$. In this thesis, the nomenclature as used by Likos [24] is adopted:

- **soft potentials** - A soft potential remains finite or diverges only slowly as $r \to 0$.
- **ultrasoft potentials** - As r approaches zero, the repulsive interaction grows much more slowly than any inverse power law.
- **bounded potentials** - A soft potential is called *bounded* if

$$v(r = 0) < \infty.$$

4.3 Q^+ and $Q^\pm$ Potentials

The considerations in this section are based on a paper called "Criterion for determining clustering versus re-entrant melting behaviour for bounded interaction potentials" by Likos et al. [25].
Some of the bounded potentials considered in this thesis can be written as

$$v(r) = \varepsilon\, \phi(r/R) \tag{4.3}$$

where $\phi(x)$ is a dimensionless function *decaying monotonically* from 1 at $r = 0$ to zero as $r \to \infty$.[1] This function does not have to be analytic, i.e. discontinuities in the potential or its derivatives are allowed. Let $\widetilde{\phi}(k) = R^{-3}\widehat{\phi}(k)$ be the dimensionless Fourier transform of the interaction.
For $\widetilde{\phi}(k)$, there are two possibilities:

- $\widetilde{\phi}(k)$ is a positive semidefinite and monotonic decaying function, i.e. $\widetilde{\phi}(k) \geq 0$ for all k. Such potentials are called Q^+*-potentials*. The Gaussian core model (GCM) [23], which will be discussed in detail in the next section, belongs to this kind of potentials.

[1] This implies that the potentials considered in this section are free of attractive parts.

- The Fourier transform has oscillatory behaviour at large k, i.e. it is a non-monotonic function of k, attaining negative values for certain ranges of the wave number. Such potentials are called $Q^{\pm}$-*potentials*. The penetrable sphere model (PSM), characterised by the interaction potential

$$v(r) = \varepsilon\, \Theta(R - r), \tag{4.4}$$

with the Heaviside step function $\Theta(x)$ is the most famous representative of this kind of potentials [23].

Detailed studies [23, 25, 26] have shown that the thermodynamic properties of these two kinds of classes of potentials differ considerably from one another:
Q^{+}-potentials show re-entrant melting behaviour, which will be discussed in detail in (4.4). For $Q^{\pm}$-potentials on the other hand, no re-entrant melting was found. Instead, the freezing line of the systems seems to persist at all temperatures, and sequences of transitions in the solid were found in which solids with multiple site occupancies are stable with increasing temperature and density. This phenomenon is called *clustering*.

4.4 The Gaussian Core Model

The GCM is a bounded potential and is defined by

$$v(r) = \varepsilon\, e^{-(r/R)^2}. \tag{4.5}$$

In the absence of an infinitely repulsive core, the first question is that of thermodynamic stability against collapse, i.e. the existence of a well defined thermodynamic limit. Let us consider a system of N particles enclosed in a fixed volume V and interacting via a Gaussian pair potential. According to Ruelle [27], the total interaction energy $\Phi_N(\mathbf{r}^N)$, which can be built up of pair or higher order potentials, is stable if there exists a $B \geq 0$ so that

$$\Phi_N(\mathbf{r}^N) \geq -NB, \tag{4.6}$$

for all $N > 0$ and all r_i, $i = 1, ..., N$ in V.
For pair potentials v, the total potential energy of the system for every arbitrary configuration $\mathbf{r}^N \in \mathbb{R}^{3N}$ of N particles can be written as

$$\Phi(\mathbf{r}^N) = \sum_{1 \leq i < j \leq N} v(|\mathbf{r}_i - \mathbf{r}_j|). \tag{4.7}$$

For purely repulsive potentials, such as the GCM with $\varepsilon \geq 0$, (4.6) is trivially satisfied with $B = 0$, implying that a well-defined thermodynamic limit exists.

The Fourier transform of the GCM reads

$$\hat{v}(k) = \pi^{3/2} \varepsilon \, R^3 e^{-k^2 R^2/4}, \tag{4.8}$$

so the dimensionless Fourier transform is given by

$$\widetilde{\phi}(k) = R^{-3} \varepsilon^{-1} \hat{v}(k) = \pi^{3/2} \, e^{-k^2 R^2/4}. \tag{4.9}$$

As $\widetilde{\phi}(k) \geq 0$ for all k, the GCM belongs to the class of the Q^+-potentials.

The GCM was first proposed by Flory and Krigbaum [28] as an effective interaction between the centres of mass of two polymer chains. Its properties as a bounded potential were first analysed by Stillinger *et al.* who calculated the $T^* = 0$ phase diagram of the GCM in the late 1970s [29], showing the existence of two stable crystal structures, i.e. face-centered cubic (fcc) for low densities and base-centred cubic (bcc) for higher ones. Later, a detailed study of the structure and of the phase behaviour of the GCM was carried out [30, 31, 32]. It was shown that for temperatures $T^* > 0.01$ the system remains fluid at all densities, whereas for $T^* \leq 0.01$ re-entrant melting is observed: increasing the density, the system shows a fluid $\rightarrow$ fcc transition, followed by a structural fcc $\rightarrow$ bcc transition and finally the crystal melts again. The region of the solid phase grows with decreasing temperature (see figure 4.1) [31].

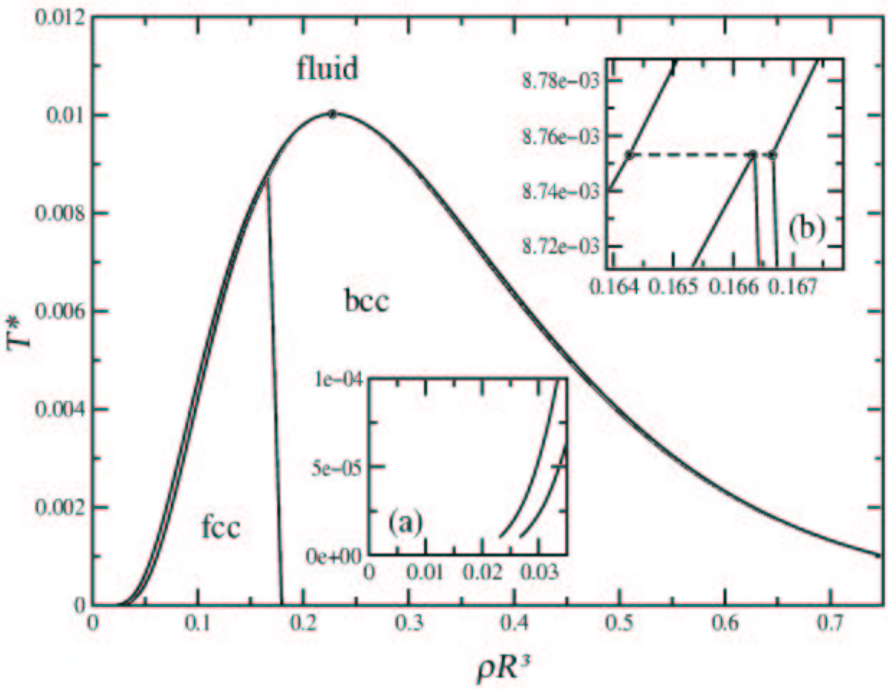

Figure 4.1: The phase diagram of the GCM according to Lang *et al.* [31]. The double lines enclose the two-phase regions. The fcc-bcc coexistence lines are also double lines but they cannot be resolved on the scale of the figure because the fcc-bcc density gap is too small.

A structural signature of this phase diagram can be seen in the anomalous behaviour of the liquid structure factor $S(k)$. The height of its main peak grows with increasing density, reaching a maximum and decreasing again.

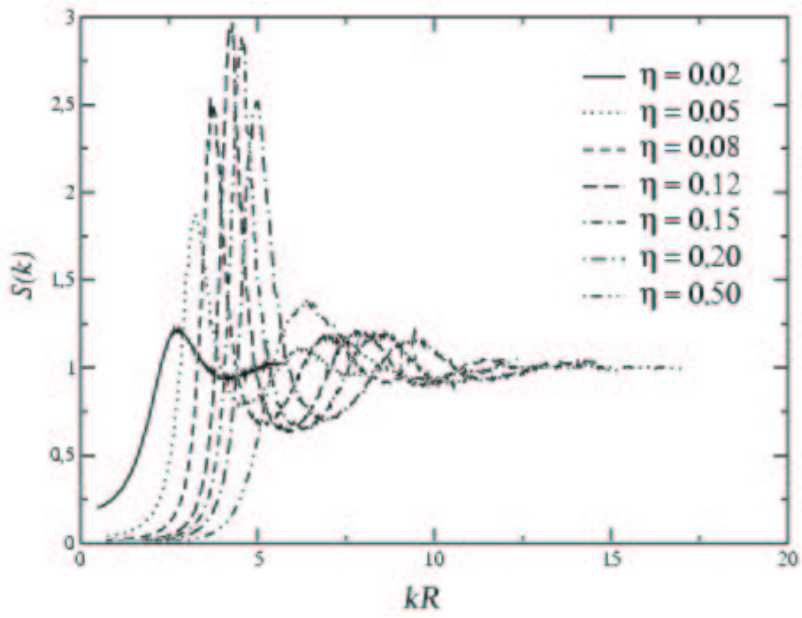

Figure 4.2: The structure factor of the GCM at $\varepsilon^* = 100$ according to [31]. Here, $\eta = \frac{\pi}{6}\varrho^*$ is the packing fraction.

This reflects the stability of the fluid beyond the re-entrant melting line. The Hansen-Verlet criterion, which states that freezing occurs when, as one decreases the temperature of the system, the magnitude of the first main peak in the structure factor $S(k)$ reaches a certain value (~ 2.8), is satisfied for both the freezing and the re-entrant melting lines (see figure 4.2) [31].
Recently, a large number of studies have been dedicated to the GCM as it is equally important to soft matter physics as is the hard sphere potential for atomic systems.

4.4.1 The GCM in the Hard Core Limit

The Boltzmann factor $B(r, \beta)$ of the Gaussian core potential is given by

$$B(r, \beta) = \exp\left[-\beta\varepsilon e^{-(r/R)^2}\right], \tag{4.10}$$

which varies from $e^{-\beta\varepsilon}$ for $r \to 0$ to 1 for $r \to \infty$. At very low temperatures $\beta\varepsilon \gg 1$, $e^{-\beta\varepsilon} \simeq 0$. Of interest are the value of r where $B(r, \beta)$ has the intermediate value $1/2$

$$r_{0.5}(\beta) = R\sqrt{\ln\left(\frac{\beta\varepsilon}{\ln 2}\right)} \tag{4.11}$$

and the derivative of $B(r,\beta)$ at this point, which is given by

$$\left.\frac{\mathrm{d}B(r,\beta)}{\mathrm{d}r}\right|_{r_{0.5}(\beta)} = \frac{r_{0.5}(\beta)}{R^2}\ln 2. \tag{4.12}$$

As β approaches infinity, $r_{0.5}(\beta)$ also approaches infinity and the derivative diverges as well. In other words, lowering the temperature, $B(r,\beta)$ looks more and more like a step function with a discontinuity at $r_{0.5}(\beta)$ [29]. This is precisely the Boltzmann factor of a hard sphere potential with a diameter $r_{0.5}(\beta)$. Therefore, the GCM is bound to display an fluid-fcc transition at low temperatures, just as the hard sphere fluid does. The coexistence densities ϱ_{solid} and ϱ_{fluid} can then be calculated from the known values in the hard sphere system [33]. In the zero-temperature limit, the GCM displays co-existence between the fluid and the fcc solid which both have very low densities.

4.4.2 The MSA for the Gaussian Core Model

The MSA is a rather simple IET, nevertheless, its decisive advantage is that it can be solved analytically in case of the Gaussian core model.
Remembering that the MSA for bounded potentials is defined by (3.20), the Fourier transform of $c(r)$ reads

$$\hat{c}(k) = -\beta\hat{v}(k) = -\pi^{3/2}\varepsilon^* R^3 e^{-k^2R^2/4}. \tag{4.13}$$

Using the OZE, the Fourier transform of $h(r)$ is obtained as[2]

$$\hat{h}(k) = -\frac{\alpha}{\varrho}\frac{1}{e^{k^2R^2/4}+\alpha}, \tag{4.14}$$

where the dimensionless coupling parameter α was introduced as

$$\alpha = \pi^{3/2}\varepsilon^*\varrho^*. \tag{4.15}$$

The structure factor can then be written as

$$S(k) = 1 + \varrho\hat{h}(k) = \frac{1}{1-\varrho\,\hat{c}(k)} = \frac{1}{1+\alpha\,e^{-k^2R^2/4}}. \tag{4.16}$$

To obtain the radial distribution function, the following equation has to be solved

$$g(r) = 1 + h(r) = 1 - \frac{\alpha}{\varrho}\frac{1}{8\pi^3}\int e^{-i\mathbf{kr}}\frac{1}{e^{k^2R^2/4}+\alpha}\,\mathrm{d}^3k. \tag{4.17}$$

This integral cannot be determined analytically, except for $r = 0$:

$$g(0) = 1 + h(0) = 1 - \frac{\alpha}{\varrho}\frac{1}{8\pi^3}\int \frac{1}{e^{k^2R^2/4}+\alpha}\,\mathrm{d}^3k = 1 + \frac{\varepsilon^*}{\alpha}\,\mathrm{Li}_{3/2}(-\alpha), \tag{4.18}$$

[2] For intermediate steps in this and the following calculations, see appendix B.

where the nth polylogarithm is defined by

$$\mathrm{Li}_n(z) = \frac{z}{\Gamma(n)} \int_0^\infty \frac{t^{n-1}}{e^t - z}\,\mathrm{d}t \quad \text{for} \quad n \in \mathbb{R}^+. \tag{4.19}$$

For a more detailed discussion of the polylogarithm, see appendix D.

Thermodynamic Properties

In the MSA, the equation of state can be calculated analytically via all three thermodynamic routes already discussed in section 3.1.2.
According to the *compressibility route*, the pressure P is given by

$$(\beta P)^{\mathrm{C}} = \int_0^\varrho \frac{\partial P(\varrho')}{\partial \varrho'}\,\mathrm{d}\varrho' = \int_0^\varrho [1 - \varrho'\hat{c}(k=0;\varrho')]\,\mathrm{d}\varrho'. \tag{4.20}$$

For the MSA, this yields,

$$\left(\frac{\beta P}{\varrho}\right)^{\mathrm{C}} = 1 + \frac{1}{2}\,\alpha. \tag{4.21}$$

For soft-core potential systems the *virial equation* (3.4) reads

$$(\beta P)^{\mathrm{V}} = \varrho + \frac{1}{2}\varrho^2\beta\hat{v}(k=0) - \frac{2\pi}{3}\varrho^2 \int_0^\infty r^3\,\frac{\partial \beta v(r)}{\partial r}\,h(r)\,\mathrm{d}r. \tag{4.22}$$

Using this equation for the GCM, one obtains

$$\left(\frac{\beta P}{\varrho}\right)^{\mathrm{V}} = 1 + \frac{1}{2}\,\alpha - \varepsilon^*\,\aleph(\alpha), \tag{4.23}$$

where

$$\aleph(\alpha) = \frac{1}{2\alpha}\,\left[\mathrm{Li}_{3/2}(-\alpha) - \mathrm{Li}_{5/2}(-\alpha)\right]. \tag{4.24}$$

This function is displayed in figure 4.3.
To obtain the equation of state according to the *energy route*, first, the excess internal energy per particle U^{ex}/N has to be calculated; one finds

$$\frac{\beta U^{\mathrm{ex}}}{N} = 2\pi\varrho\beta \int_0^\infty v(r)\,g(r)\,r^2\,\mathrm{d}r = \frac{\alpha}{2} - \frac{\varepsilon^*}{2\alpha}\,\left[\alpha + \mathrm{Li}_{3/2}(-\alpha)\right]. \tag{4.25}$$

Then, the excess free energy per particle F^{ex}/N is given by

$$\frac{\beta F^{\mathrm{ex}}}{N}(\varrho) = \int_0^\beta \frac{\beta' U^{\mathrm{ex}}}{N}(\beta',\varrho)\,\frac{\mathrm{d}\beta'}{\beta'} = \frac{\alpha}{2} - \frac{\varepsilon^*}{2\alpha}\,\left[\alpha + \mathrm{Li}_{5/2}(-\alpha)\right]. \tag{4.26}$$

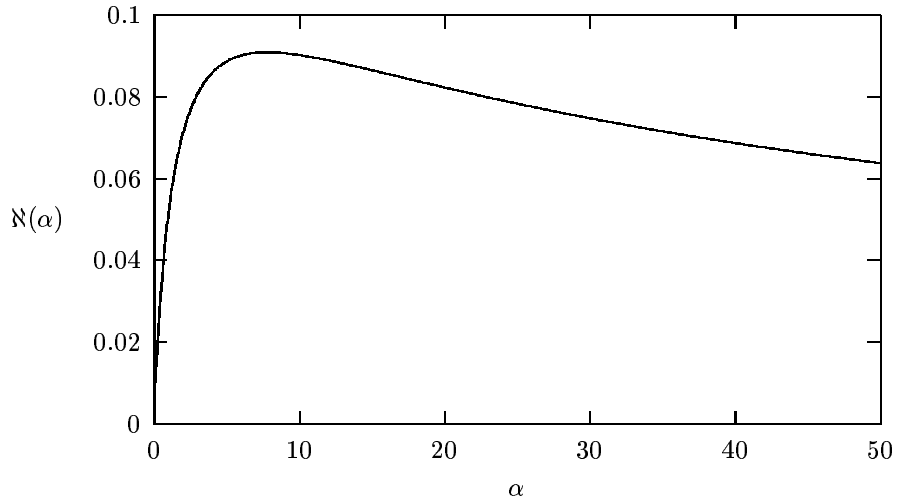

Figure 4.3: $\aleph(\alpha)$ [see (4.24)] is zero for $\alpha = 0$, has a maximum of 0.09082 at $\alpha = 7.798$ and approaches zero for $\alpha \to \infty$, which implies that for any fixed ε^*, the MSA becomes thermodynamically consistent in the high density limit.

Subsequently, the excess pressure P^{ex} is obtained by

$$\left(\frac{\beta P^{\mathrm{ex}}}{\varrho}\right)^{\mathrm{E}} = \varrho \frac{\partial \beta F^{\mathrm{ex}}/N}{\partial \varrho} = \frac{1}{2}\,\alpha - \varepsilon^*\,\aleph(\alpha). \tag{4.27}$$

Hence, the equation of state according to the energy route is given by

$$\left(\frac{\beta P}{\varrho}\right)^{\mathrm{E}} = 1 + \frac{1}{2}\,\alpha - \varepsilon^*\,\aleph(\alpha). \tag{4.28}$$

Comparing (4.23) to (4.28), it can be seen that in the MSA the virial and the energy route yield the same expression for the pressure of the system, i.e. that the MSA is thermodynamically consistent for the GCM regarding those two routes.

4.4.3 The SCOZA for the Gaussian Core Model

Instead of using (3.30) as an ansatz for the direct correlation function, in this thesis the following equation was used as a start for the SCOZA:

$$c(r) = \beta K(\varrho, \beta)\, v(r). \tag{4.29}$$

Here, $K(\varrho, \beta)$ is a dimensionless function to be determined such that the virial and the compressibility route yield thermodynamically consistent results.

Now, the Fourier transform of $c(r)$ reads

$$\hat{c}(k) = \beta K(\varrho,\beta)\,\hat{v}(k) = \pi^{3/2}\varepsilon^* R^3 K(\varrho,\beta)\; e^{-k^2R^2/4}. \tag{4.30}$$

Using the OZE, one obtains the Fourier transform of the pair correlation function

$$\hat{h}(k) = \frac{\psi}{\varrho}\frac{1}{e^{k^2R^2/4}-\psi}, \tag{4.31}$$

where

$$\psi = \pi^{3/2}\varrho^*\varepsilon^* K(\varrho,\beta) \tag{4.32}$$

is a dimensionless coupling parameter.
The SCOZA demands (3.28) to be fulfilled: the right hand side of this equation can be written as

$$1-\varrho\,\hat{c}(k=0) = 1-\psi. \tag{4.33}$$

To obtain the left hand side, at first, we need the expression for the pressure according to the virial equation:

$$\left(\frac{\beta P}{\varrho}\right)^{\mathrm{V}} = 1-\frac{2\pi}{3}\beta\varrho\int_0^\infty \frac{\partial v(r)}{\partial r}\,g(r)\,\mathrm{d}r. \tag{4.34}$$

In the given case, this relation results in

$$\left(\frac{\beta P}{\varrho}\right)^{\mathrm{V}} = 1+\frac{\alpha}{2}-\frac{\varepsilon^*}{2\psi}\left[\mathrm{Li}_{5/2}(\psi)-\mathrm{Li}_{3/2}(\psi)\right], \tag{4.35}$$

where α is defined by (4.15). Next, the derivative of the pressure is needed

$$\begin{aligned}\left(\frac{\partial\beta P}{\partial\varrho}\right)^{\mathrm{V}} &= 1+\alpha-\frac{1}{2R^3\pi^{3/2}K(\varrho,\beta)^2}\left\{\frac{K(\varrho,\beta)}{\varrho}\left[\mathrm{Li}_{3/2}(\psi)-\mathrm{Li}_{1/2}(\psi)\right]+\right.\\ &\left.+\frac{\partial K(\varrho,\beta)}{\partial\varrho}\left[2\mathrm{Li}_{3/2}(\psi)-\mathrm{Li}_{5/2}(\psi)-\mathrm{Li}_{1/2}(\psi)\right]\right\}.\end{aligned} \tag{4.36}$$

Then, (3.28) yields

$$\frac{\partial K(\varrho,\beta)}{\partial\varrho} = \frac{K(\varrho,\beta)\left\{2\pi^3\beta\varepsilon R^6\varrho^2 K(\varrho,\beta)\,[K(\varrho,\beta)+1]-\left[\mathrm{Li}_{3/2}(\psi)-\mathrm{Li}_{1/2}(\psi)\right]\right\}}{\varrho\left[2\mathrm{Li}_{3/2}(\psi)-\mathrm{Li}_{5/2}(\psi)-\mathrm{Li}_{1/2}(\psi)\right]}. \tag{4.37}$$

This equation is a partial differential equation for the unknown function $K(\beta,\varrho)$. Its solutions gives via (4.29) the direct correlation function. In this thesis, (4.37) has been solved numerically. For results, see section 7.1.

4.5 The Double Gaussian Core Model

We also consider a family of potentials which we call the *double Gaussian core model* (DGCM) to analyse how the thermodynamic properties change if a second Gaussian located at $r = 0$ is subtracted from the GCM.
The DGCM is defined by

$$v(r) = \varepsilon \left(e^{-(r/R)^2} - \eta e^{-(r/\zeta R)^2} \right), \tag{4.38}$$

where η and ζ are dimensionless real parameters.
The Fourier transform of the potential is given by

$$\hat{v}(k) = \pi^{3/2} \varepsilon R^3 \left(e^{-k^2 R^2/4} - \eta \zeta^3 e^{-\zeta^2 k^2 R^2/4} \right). \tag{4.39}$$

Depending on the values of η and ζ, this potential can have an attractive component (see figure 4.4 and figure 4.5). The proposal of soft potentials with a small attractive part is not completely academic, as it has been shown in [34] that for intermediate densities the effective pair potential between the centres of mass of two polymer coils in a good solvent exhibits a small attractive part at distances of the order of several times the radius of gyration R_{g}. Furthermore, it was found out in [35] that when the polymer coils are no longer in a good solvent, the potential can develop even larger attractive parts.
Out of the mentioned reasons, in this thesis we only consider members of the DGCM family which at first decay monotonically and then have a small attractive part. We do not consider potentials that have a "potential hole" at $r = 0$ followed by a potential hill (see figure 4.4 and 4.5), as they are irrelevant for the physical systems considered in this work.

4.5.1 The Double Gaussian Core Model and Stability

As the DGCM may develop an attractive part for certain values of η and ζ, it is not self-evident that (4.6) is fulfilled. Fortunately, there is a weaker condition than (4.6), namely

$$\hat{v}(0) = \int v(r)\, \mathrm{d}\mathbf{r} > 0, \tag{4.40}$$

which is necessary, but not sufficient for the existence of thermodynamic stability. It is used here as stability criterion, as it is easier to treat, especially for IETs.
For all values of η and ζ which satisfy the condition

$$\eta \zeta^3 < 1, \tag{4.41}$$

Ruelle's stability criterion (4.40) is violated and hence they belong to the class of potentials he refers to as being "catastrophic"[27]. Once again, it has to be emphasised that the stability criterion (4.40) is necessary, yet not sufficient for a thermodynamic limit. This means that even

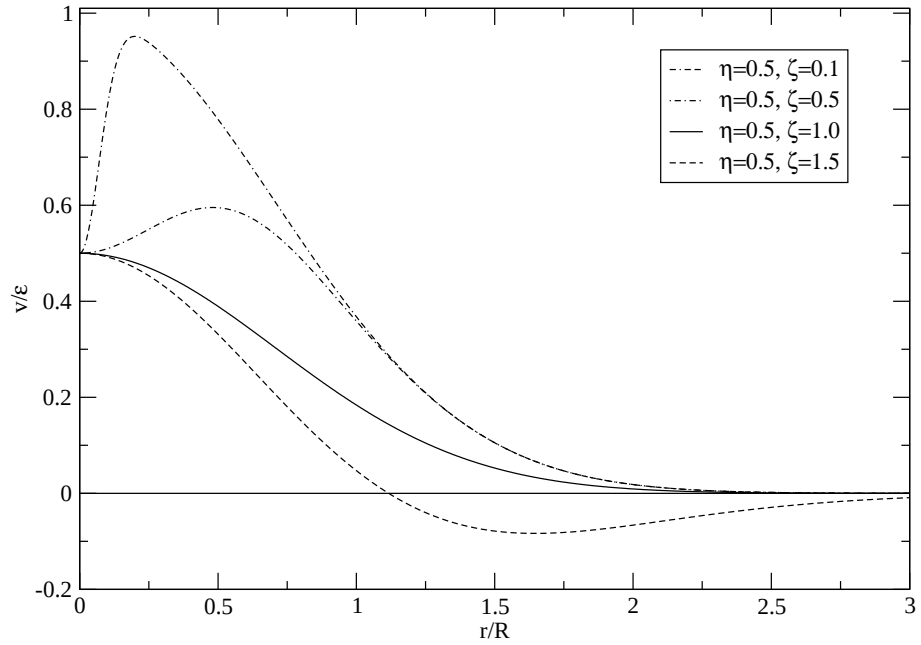

Figure 4.4: The DGCM for fixed value $\eta = 0.5$ and varying ζ

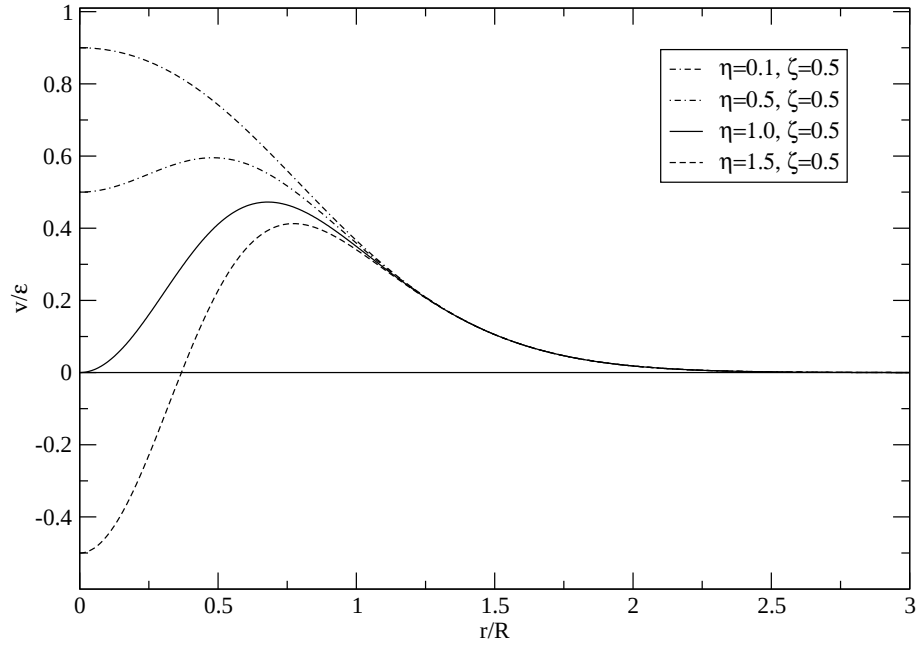

Figure 4.5: The DGCM for fixed value $\zeta = 0.5$ and varying η

for values of η and ζ which satisfy $\eta\zeta^3 < 1$ but are too close to this boundary line the potential can be unstable.

4.5.2 The Double Gaussian Core Model and Q^+ and $Q^\pm$ Potentials

In section 4.3 we discussed that potentials which are bounded, positive semidefinite and monotonically decaying can be divided into two classes: Q^+ and $Q^\pm$ potentials. As the DGCM potentials are not positive semidefinite and not monotonically decaying functions for each arbitrary combination of (η, ζ), this classification cannot be applied to the DGCM. It is not yet clear if the $Q^+/Q^\pm$-classification can be generalised or extended to also properly predict the behaviour of the DGCM potentials. Clarifying this question might be the object of a separate investigation.

4.5.3 The MSA for the Double Gaussian Core Model

For the double Gaussian core model, (3.20) reads

$$\hat{c}(k) = -\beta\hat{v}(k) = -\pi^{3/2}\varepsilon^* R^3 \left(e^{-k^2R^2/4} - \eta\zeta^3 e^{-\zeta^2 k^2 R^2/4}\right). \tag{4.42}$$

Inserting this result into the Fourier transform of the OZE, one obtains

$$\hat{h}(k) = -\frac{\alpha}{\varrho}\left(\alpha + \frac{e^{k^2R^2(1+\zeta^2)/4}}{e^{\zeta^2k^2R^2/4} - \eta\zeta^3 e^{k^2R^2/4}}\right)^{-1}, \tag{4.43}$$

where α is given by (4.15).
Now, the structure factor $S(k)$ can easily be obtained as

$$S(k) = 1 + \varrho\hat{h}(k) = \frac{1}{1 + \alpha\left(e^{-k^2R^2/4} - \eta\zeta^3 e^{-\zeta^2k^2R^2/4}\right)}. \tag{4.44}$$

Thermodynamic Properties

The equation of state according to the compressibility route is given by (4.20). For the proposed model, this yields

$$\left(\frac{\beta P}{\varrho}\right)^{\mathrm{C}} = 1 + \frac{1}{2}\alpha\left(1 - \eta\zeta^3\right). \tag{4.45}$$

Both the virial and the energy route are mathematically too complicated to be solved analytically.

4.6 The Generalised Gaussian Core Model with Index n

In the last step, we propose a family of bounded potentials $v_n(r)$ depending on a tunable parameter n

$$v_n(r) = \varepsilon\, e^{-(r/R)^n} \tag{4.46}$$

and we call this class of potentials *generalised Gaussian core model with index n* (GGCM-n). The case $n = 2$ yields the GCM. As n increases, the slope of the potential becomes steeper and finally, for $n \to \infty$, the penetrable sphere model is recovered.

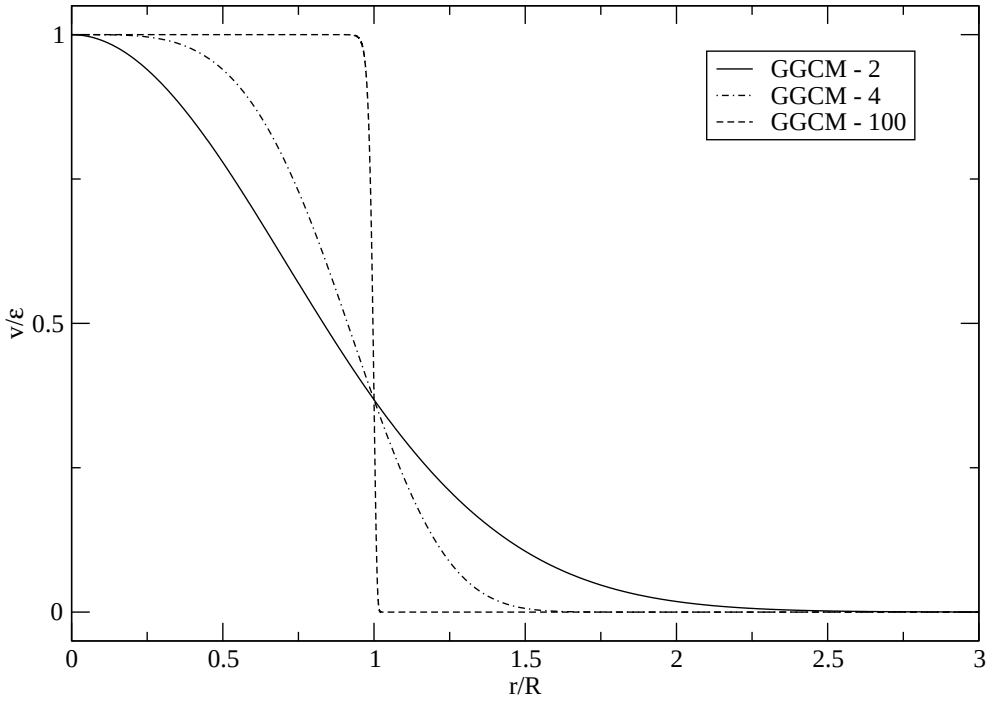

Figure 4.6: The GGCM for $n = 2$, $n = 4$ and $n = 100$.

A closed expression for the Fourier transform of the general GGCM does not exist. For $n = 4$, however, the Fourier transform is given by

$$\hat{v}(k) = -\frac{1}{24}kR^3\left\{-8\Gamma\left(\frac{7}{4}\right){}_0F_2\left(;\frac{1}{2},\frac{5}{4};\frac{k^4R^4}{256}\right) + k^2R^2\,\Gamma\left(\frac{5}{4}\right){}_0F_2\left(;\frac{3}{2},\frac{7}{4};\frac{k^4R^4}{256}\right)\right\}, \qquad (4.47)$$

where $\Gamma(z)$ is the Gamma function and ${}_pF_q(a_1, ..., a_p; b_1, ...b_q; z)$ are the generalised hypergeometric functions [36] given by

$${}_pF_q(a_1, ..., a_p; b_1, ...b_q; z) = \sum_{k=0}^{\infty} \frac{(a_1)_k \ldots (a_p)_k}{(b_1)_k \ldots (b_q)_k} \frac{z^k}{k!} \qquad (4.48)$$

and $(a)_k$ is the *Pochhammer symbol* or *rising factorial*

$$(a)_k = \frac{\Gamma(a+k)}{\Gamma(a)} = a\,(a+1)\ldots(a+k-1). \qquad (4.49)$$

4.6.1 The Generalised Gaussian Core Model and Q^+ and $Q^\pm$ Potentials

As the GCM belongs to the class of Q^+ potentials, whereas the PSM is a $Q^\pm$ potential, there has to be a critical parameter n_c, with members of the GGCM with $n \leq n_c$ belonging to the Q^+ class and members with $n > n_c$ belonging to the $Q^\pm$ one. Calculations which determine whether the Fourier transformation of the potential is positive or equal to zero for all wave vectors k or not,

have shown that

$$n_c = 2, \tag{4.50}$$

so for increasing n the GCM should be the last potential showing re-entrant melting. In this thesis, we studied the case $n = 4$ as a counterpart to the GCM.

Chapter 5

Implementation

5.1 Integral Equation Theories

5.1.1 The Broyles Algorithm

One numerical solution method for conventional IETs, like the HNC and PY approximation, is an iterative procedure based on a Picard iteration, called *Broyles' algorithm* [37]:
Introducing the function

$$\gamma(r) = h(r) - c(r) \tag{5.1}$$

the direct correlation function according to the HNC approximation can be rewritten as

$$c_{\mathrm{HNC}}(r) = e^{-\beta v(r)+\gamma(r)} - \gamma(r) - 1 \tag{5.2}$$

and in case of the PY closure it becomes

$$c_{\mathrm{PY}}(r) = (e^{-\beta v(r)} - 1)(\gamma(r) + 1). \tag{5.3}$$

Using the Fourier transform of the OZE (3.14), we get the following relation in terms of $\widehat{\gamma}(k)$

$$\widehat{\gamma}(k) = \frac{\varrho\,\hat{c}^2(k)}{1 - \varrho\,\hat{c}(k)}. \tag{5.4}$$

As a first ansatz of $c(r)$ one can, for instance, use $c(r) = c_0(r)$ according to the MSA. Then, $c_0(r)$ is Fourier transformed to obtain $\widehat{c}_0(k)$ according to the closure. An inverse Fourier
$\gamma_1(r)$ is [illegible]
on provides an estimate for $\gamma_1(r)$, which is used as input for (5.2) or (5.3). As a
t $c_1(r)$. This elementary cycle is repeated with $c_1(r)$ replacing $c_0(r)$, thus leading to
f functions $c_n(r)$. The cycle is iterated until the difference between $c_n(r)$ and $c_{n+1}(r)$
he desired accuracy (typically about 10^{-8}).
s, this iterative method does not converge, but a simple modification of the algorithm

fixes the problem:
Instead of using

$$c_{\text{new}}^{\text{HNC}}(r) = e^{-\beta v(r)+\gamma_{n+1}(r)} - \gamma_{n+1}(r) - 1 \tag{5.5}$$

or respectively

$$c_{\text{new}}^{\text{PY}}(r) = (e^{-\beta v(r)} - 1)(\gamma_{n+1}(r) + 1) \tag{5.6}$$

as an input for a new cycle, one mixes the new and the old result:

$$c_{n+1}(r) = \lambda\, c_{\text{new}}(r) + (1 - \lambda)\, c_n(r), \tag{5.7}$$

where $0 < \lambda < 1$ is a fixed real parameter that has to be chosen empirically to achieve maximum stability of the algorithm.
The numerical procedure requires the use of a finite grid of points in r-space over which the functions are to be defined. Consequently, this implies that also the k-space is discretised, and the accuracy of the final solution strongly depends both on the overall extent of those grids and on their spacings. In this work, the discretisations of r-space and k-space were defined by the use of a Fast Fourier transformation procedure.

5.2 Monte Carlo Simulations

5.2.1 Boundary Conditions

MC simulations aim to provide information about the thermodynamic and structural properties of a macroscopic sample of the system of interest. Unfortunately, the number of degrees of freedom that can conveniently be handled in present-day computer simulations ranges from a few thousand to a few million. Most simulations probe the structural and thermodynamic behaviour of a system of a few hundred to a few thousand particles. Clearly, this number is still far from the thermodynamic limit. For such small systems it cannot be safely assumed that the choice of boundary conditions has a negligible effect on the properties of the system. For instance, in a three-dimensional N-particle system with free boundaries, the fraction of particles that is at the surface is proportional to $N^{-1/3}$. In a simple cubic crystal of 1 000 atoms, some 49% of all atoms are at the surface, whereas for 10^6 atoms this fraction has decreased to roughly 6%. So for the simulation of only a few hundred particles it is decisive to choose boundary conditions in a way that the simulations are not biased by surface effects.
Therefore, in order to correctly simulate bulk phases it is essential to choose boundary conditions that mimic the presence of an infinite bulk surrounding the N-particle system. This is usually achieved by imposing *periodic boundary conditions*. The box containing the N particles is treated as a primitive cell of an infinite periodic lattice of identical cells. A given particle i now interacts

with all other particles in this infinite periodic system, i.e. all other particles in the same cell and all particles, including its own periodic image, in all other cells (see figure 5.1). If we assume the interactions to be pairwise additive, then the total potential energy of the N particles is

$$\Phi = \frac{1}{2} \sum_{i,j;\mathbf{n}}{}' v\left(|\mathbf{r}_{ij} + \mathbf{n}L|\right) \tag{5.8}$$

where L is the edge length of the periodic, cubic box and $\mathbf{n}$ is an arbitrary vector of three integer numbers, while the prime over the sum indicates that the term $i = j$ is excluded when $\mathbf{n} = \mathbf{0}$.
In this general form, periodic boundary conditions are not very useful, as the potential energy has to be rewritten as an infinite sum rather than a finite one as in (3.3) to simulate bulk behaviour. Moreover, although the use of periodic boundary conditions proves to be an effective method to simulate homogeneous bulk systems, one has to be aware that such boundary conditions may lead to spurious correlations not present in a truly macroscopic bulk system. On the other side, the use of these boundary conditions inhibits the occurrence of long-wavelength fluctuations, as the periodicity will suppress any density waves with a wavelength greater than L.

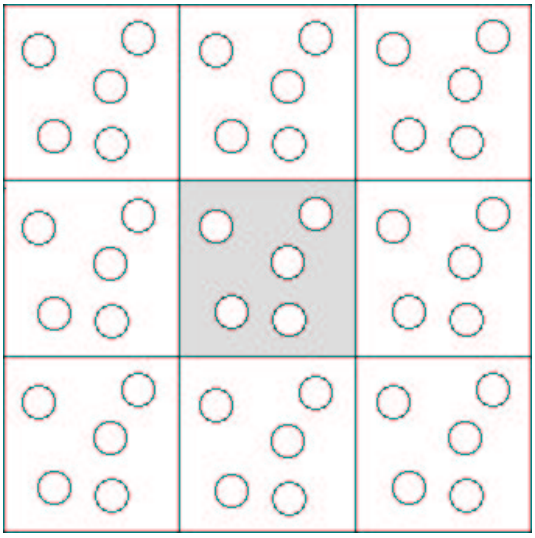

Figure 5.1: Schematic representation of periodic boundary conditions.

5.2.2 Potential Truncation

As already discussed in the previous section, at first sight, truly periodic boundary conditions would appear to be intractable as an infinite number of interactions has to be summed. Often, however, MC simulations deal only with short-range interactions. These are interactions where the potential decays faster than r^{-3} for $r \to \infty$, which means that the potential energy of a given particle i is dominated by interactions with neighbouring particles that are closer than some *cutoff distance* r_c. In particular, the case $r_c \leq L/2$ means that that for a given particle i interactions with

the nearest periodic image of at most any other particle j have to be considered. This so-called *minimum image convention* is shown in figure 5.2.

If the intermolecular potential is not rigorously zero for $r > r_c$, truncation of the intermolecular interactions at r_c will result in a systematic bias in the calculation of thermodynamic properties. This bias can be corrected by adding *tail corrections*; for instance, the expression for the potential energy becomes:

$$\Phi = \sum_{i<j} v_c(r_{ij}) + \frac{N\varrho}{2} \int_{r_c}^{\infty} 4\pi r^2 v(r)\, dr \tag{5.9}$$

where $v_c(r)$ denotes the truncated potential energy function. As can be seen from the second term in the previous equation, the tail correction implicitly assumes that

$$g(r) = 1 \quad \text{for } r > r_c. \tag{5.10}$$

This means that for $r \geq r_c$ the tail correction replaces the discrete particle system by an infinite continuum.

The simplest method to truncate a potential is to ignore all interactions beyond the spherical cutoff r_c. The potential simulated can then be written as

$$v_c(r) = \begin{cases} v(r) & r \leq r_c \\ 0 & r > r_c \end{cases} \tag{5.11}$$

To obtain the pressure, the calculation of the virial has to be corrected in a similar way as the potential energy:

$$W^{\text{tail}} = \sum_{\substack{i<j \\ r<r_c}} r_{ij} \frac{\partial v(r)}{\partial r}\Big|_{r=r_{ij}} + \frac{N\varrho}{2} \int_{r_c}^{\infty} 4\pi\varrho r^2 r \frac{\partial v(r)}{\partial r}\, dr. \tag{5.12}$$

5.2.3 Initialisation

To start the simulation, initial positions have to be assigned to all particles in the system. As the equilibrium properties of the system do not depend on the choice of initial conditions, all reasonable initial conditions are acceptable. When simulating a liquid, usually one either starts from any convenient crystal structure which melts during the simulation[1], or from some arbitrary (i.e. random) gas configuration. If available, it is preferable to use the final, well-equilibrated configuration of an earlier simulation at a nearby state point as the starting configuration for a new run and to adjust the temperature and density to the desired values.

No matter which of the mentioned starting configurations is used, it is normally not "in equilibrium", i.e. this configuration is usually not a typical one for the given macroscopic thermodynamic

[1] This starting configuration has to be used with some care as the crystal structure may be meta-stable - even if it is not absolutely stable - if simulating a system close to the freezing curve.

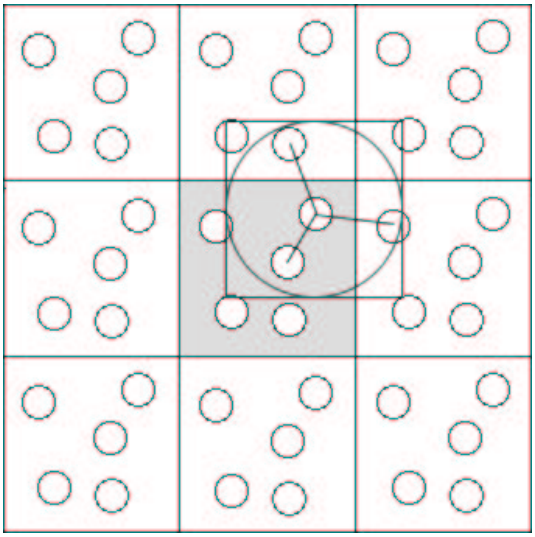

Figure 5.2: Schematic representation of the minimum image convention. The box around one of the particles contains the same number of particles as the central box. The circle represents a potential cutoff, i.e. only those particles that are connected by a line interact directly with the particle in the centre.

parameters. Starting the simulation, the system moves towards equilibrium and reaches it within a number of passes depending on the system and on the given circumstances.[2] Thus, initially, a rather large number of configurations the system has passed through has to be neglected when calculating ensemble averages, as those configurations are untypical for the equilibrium probability distribution function.

[2] A pass consists of N trial moves, i.e. on average each particle has been subjected to a trial move once.

Chapter 6

Technical Details

In this thesis, we have concentrated on energies relevant for polymer solutions ($\varepsilon^* \sim 2$) [32]. In particular, we have analysed the GCM and the DGCM for $\varepsilon^* = 0.1$ and $\varepsilon^* = 2$ and have limited our attention to the reduced density region $\varrho^* \in [0, 2.5]$. Furthermore, we have also studied the radial distribution function $g(r)$ for the DGCM at $\varepsilon^* = 5$ and $\varrho^* = 0.1$ and $\varrho^* = 10$. We have analysed the GGCM-4 for $\varepsilon^* = 0.1$ in the reduced density region $\varrho^* \in [0, 2.5]$ and for $\varepsilon^* = 2$ we have limited our attention to the reduced density region $\varrho^* \in [0, 7]$.

6.1 Integral Equation Theories

We have discretised the correlation functions in r-space and k-space on a grid of 1024 points. The maximum radius was chosen to be $r_{\max} = 20R$ and thus, the grid-size in k-space is given by $\Delta k = \pi / r_{\max}$. The mixing parameter in the Broyles algorithm was chosen to be $\lambda = 0.5$ for both the HNC and the PY approximation.

To obtain the pressure according to the different routes, i.e. virial, compressibility and energy equation, we have used the following parameters:

- For the **MSA** and the GCM, the solution for all three routes was obtained analytically. For the DGCM, the compressibility equation was integrated analytically. To obtain the pressure according to the virial route, we have evaluated the following equation

$$\frac{\beta P}{\varrho} = 1 - \frac{2\pi}{3} \beta \varrho \int g(r)\, r^2 \left(r \frac{d}{dr} v(r) \right) \mathrm{d}r. \tag{6.1}$$

  For this, we chose 1024 r-grid points for distances up to $r_{\max} = 20R$ and evaluated this equation for 500 reduced densities ϱ^* up to $\varrho^*_{\max} = 2.5$ using the Simpson integration algorithm. For the energy route, one needs to calculate the free energy as an integral over the

internal energy with respect to the reduced energy ε^*:

$$\frac{\beta F^{\mathrm{ex}}}{N} = \int_0^{\varepsilon^*} \frac{\beta U^{\mathrm{ex}}}{N} \frac{\mathrm{d}\tilde{\varepsilon}^*}{\tilde{\varepsilon}^*}. \tag{6.2}$$

This integral was also evaluated numerically with $n_{\varepsilon^*} = 1\,000$ grid points up to the reduced energy ε^* characterising the system. To evaluate the derivative

$$\left(\frac{\beta P^{\mathrm{ex}}}{\varrho}\right)^{\mathrm{E}} = \varrho \frac{\partial \beta F^{\mathrm{ex}}/N}{\partial \varrho} \tag{6.3}$$

we chose a reduced density grid $n_{\varrho^*} = 250$ and $\varrho^*_{\mathrm{max}} = 2.5$.
In the case of the GGCM-4, the virial and energy route were treated analogously to the DGCM. To solve the compressibility equation, we have calculated $\hat{c}(0)$, which in the case of the MSA is independent of ϱ^*, and have used this result in the subsequent step to analytically solve the following (general) equation:

$$(\beta P)^{\mathrm{C}} = \int_0^{\varrho} [1 - \varrho' \hat{c}(k = 0; \varrho')] \, \mathrm{d}\varrho'. \tag{6.4}$$

- For all potentials considered in this thesis, the solutions for the virial and energy route of both the **HNC** and **PY** approximation were obtained analogously to the case of the MSA and the DGCM. To solve the compressibility equation, we have calculated $\hat{c}(0)$ at 100 000 ϱ^* points, as $\hat{c}(0)$ is density-dependent for these closures. As numerical inaccuracies have to be minimised when performing the integral in (6.4), we have discretised the reduced density interval into 100 000 subintervals and have calculated the pressure only for $n_{\varrho^*} = 500$ uniformly distributed points by integrating over the intermediate 200 points in each subinterval. Furthermore, it has to be mentioned that we have analysed the pressure for reduced densities up to $\varrho^*_{\mathrm{max}} = 2.5$ or to the maximum reduced density where the Broyles algorithm still converges for the different closures.

- For the **SCOZA** and the GCM, we chose $n_{\varrho^*} = 2048$ and ϱ^*_{max} depends upon the convergence of the solution algorithm for (4.37): for $\varepsilon^* = 0.1$, $\varrho^*_{\mathrm{max}} = 2.5$ and for $\varepsilon^* = 2$, $\varrho^*_{\mathrm{max}} = 0.78$.

6.2 Monte Carlo Simulations

6.2.1 The Gaussian Core Model and the Double Gaussian Core Model

We have carried out MC simulations in the canonical ensemble for $\varepsilon^* = 0.1$ and $\varepsilon^* = 2.0$ for the reduced density values $\varrho^* = \{0.1, 0.5, 1, 1.5, 2, 2.5\}$. Starting from a random configuration of 1 000 particles, the system was first allowed to equilibrate for 10 000 passes, where a pass consists

of N trial moves, i.e. on average each particle has been subjected to a trial move once; after that, we have carried out a production run of another 150 000 passes to calculate the desired ensemble averages. For the GCM and $\varrho^* = 0.1$ and $\varrho^* = 2$ at $\varepsilon^* = 0.1$ we have doubled the number of passes to 300 000 to get more reliable results for $g(r)$.

6.2.2 The Generalised Gaussian Core Model with Index n

We have simulated the GGCM-4 at $\varepsilon^* = 0.1$ for the reduced density values $\varrho^* = \{0.1, 0.5, 1, 1.5, 2, 2.5\}$ and at $\varepsilon^* = 2.0$ for the reduced densities $\varrho^* = \{0.1, 0.5, 1, 1.5, 2, 2.5, 3, 3.5, 4, 5, 6, 7\}$. Starting from a random configuration of 1 000 particles, the system was first allowed to equilibrate for 10 000 passes and after that, we have carried out a production run of another 150 000 passes. As will be shown in section 7.3, for reduced densities $\varrho^* \gtrsim 2.0$ and $\varepsilon^* = 2$, the particles arrange themselves in clusters during the simulation. Taking the position of the first minimum of $g(r)$ as a measure of the average dimensions of a cluster, we have counted the mean number of particles belonging to a cluster. These values have been used to start MC simulations with a number of particles chosen such that, for the given reduced density, an fcc crystal of clusters may form in the simulation box, i.e.

$$N = 4m^3 s_{\mathrm{cl}} \qquad m = 1, 2, 3, ..., \tag{6.5}$$

where N is the number of particles in the simulation box and s_{cl} is the mean cluster size as obtained from the previous MC simulations. The resulting particle numbers were:

ϱ^*	2.5	3	3.5	4	5	6	7
s_{cl}	4.5	5.7	6.9	8.2	9.7	11.5	13.0
N	1 152	620	750	885	1 049	1 241	1 403

We have started the simulations from random configurations and the equilibration and production phases have been analogous to the previous simulations.

Chapter 7

Results

7.1 The Gaussian Core Model

7.1.1 The Radial Distribution Function $g(r)$

This section is organised as follows: First, we verbally discuss the results for $g(r)$ as acquired by the previously discussed methods in detail. Next, we present plots of our results for the SCOZA and afterwards, we show plots of $g(r)$ obtained by the different closures and compare these results to the data obtained by MC simulations for $\varepsilon^* = 0.1$ and $\varepsilon^* = 2$ at a low reduced density $\varrho^* = 0.1$ and a high reduced density $\varrho^* = 2$; in the captions of the figures we comment on the observed phenomenona.

In general, at low densities $g(r)$ for the GCM looks like a sigmoid function [38] rising from a non-zero value $g(0)$ to the asymptotic value 1, i.e. it is a monotonous curve and lacks an oscillating structure.

As already discussed in section 4.5.3, the MSA can be solved analytically for the GCM. For $\varepsilon^* < 1$, $g_{\mathrm{MSA}}(0)$ is positive for all reduced densities ϱ^*. However, when $\varepsilon^* > 1$, there is always a reduced density ϱ^*_{MSA} below which $g_{\mathrm{MSA}}(0) < 0$, i.e. g_{MSA} becomes unphysical (see figure 7.2). Nevertheless, even for $\varrho^* < \varrho^*_{\mathrm{MSA}}$, the pressure is still reasonably well described by the MSA, as deficiencies or even an unphysical behaviour of $g(r)$ at small r do not strongly affect P [see (3.4)].

The HNC approximation yields very good results for all energies and densities in the case of the GCM, which can be seen by comparing the HNC data to the results of MC simulations. HNC converges everywhere in the energy-density area considered in this work ($\varepsilon^* \leq 95$ and $\varrho^* < 100$[1]).

Though the PY closure is usually not a favourable choice for soft potentials, it yields nearly the same results as the HNC closure for low energies and low densities. However, for energies $\varepsilon^* \gtrsim 5$ and low densities, the PY closure breaks down, as it requires a large number of iterations in the Broyles algorithm until the PY approximation converges, and the solution obtained for $g(r)$ is oscillatory rather than a monotonous curve. Finally, for high densities, PY does not converge at

[1] It has to be remembered that for $\varepsilon^* \gtrsim 100$ re-entrant crystallisation sets in [29].

all.

In the case of the SCOZA closure, the differential equation (4.37) has to be solved. In this thesis, this was done by using *Mathematica* [39] as it implements the polylogarithm in an efficient way. *Mathematica*'s built-in function `NDSolve` was used to obtain a numerical solution for the differential equation. Unfortunately, as the reduced energy ε^* is increased, a solution can only be obtained for decreasing density intervals.

As (4.37) is singular for $\varrho = 0$, we have to investigate its behaviour for small densities. Assuming that $K(\varrho, \beta)$ remains finite as $\varrho \to 0$, we perform a series expansion of all other terms in terms of ϱ around zero up to order ϱ^{-1}:

$$\frac{\partial K(\varrho,\beta)}{\partial \varrho} = \frac{-2\beta\varepsilon K(\varrho,\beta) - 8\sqrt{2}\,[1 + K(\varrho,\beta)]}{\beta\varepsilon\,\varrho} + \mathcal{O}\left(\varrho^0\right). \tag{7.1}$$

Solving this differential equation for low densities, one obtains

$$K(\varrho,\beta) = -\frac{4\sqrt{2}}{4\sqrt{2}+\beta\varepsilon} + C\,\varrho^{-2(4\sqrt{2}+\beta\varepsilon)/\beta\varepsilon}, \tag{7.2}$$

where C is an integration constant. Therefore, for $\varrho = 0$

$$K(\varrho,\beta) = -\frac{4\sqrt{2}}{4\sqrt{2}+\beta\varepsilon}. \tag{7.3}$$

$K(\varrho, \beta)$ can be seen in figure 7.1 for different values of the reduced energy ε^*.

Just as for the MSA, for the SCOZA, there is also a reduced density $\varrho^*_{\mathrm{SCOZA}}$, below which $g_{\mathrm{SCOZA}}(0) < 0$. However, $\varrho^*_{\mathrm{SCOZA}} < \varrho^*_{\mathrm{MSA}}$, which can be seen in figure 7.2.

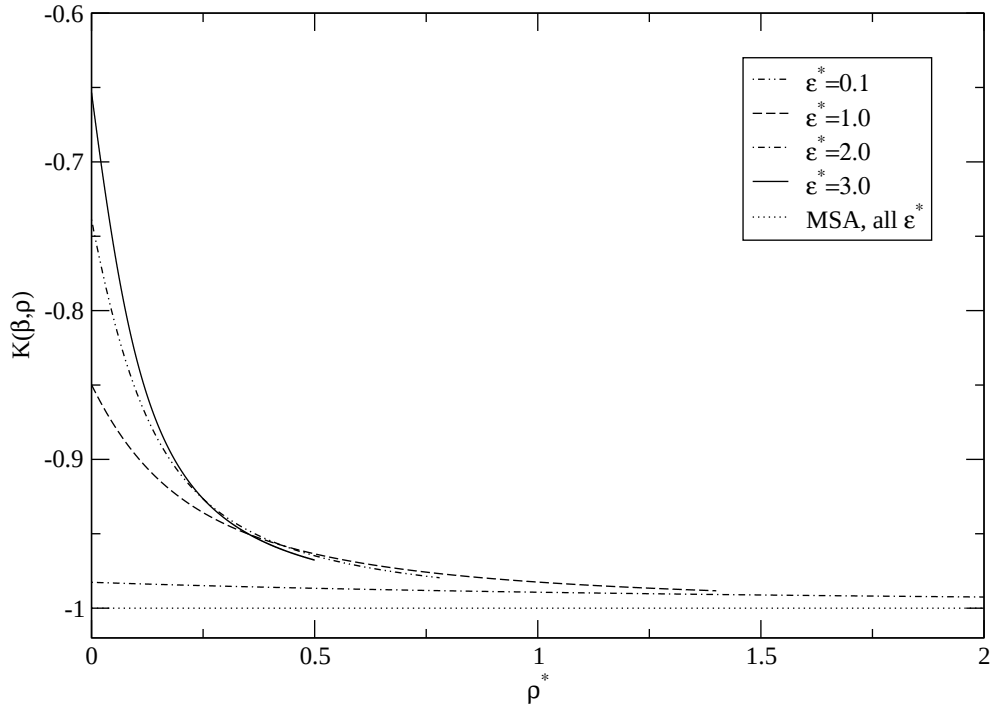

Figure 7.1: $K(\beta, \varrho)$ as a function of ϱ^* as a result of (4.37) for different values of the reduced energy ε^* compared to the MSA.

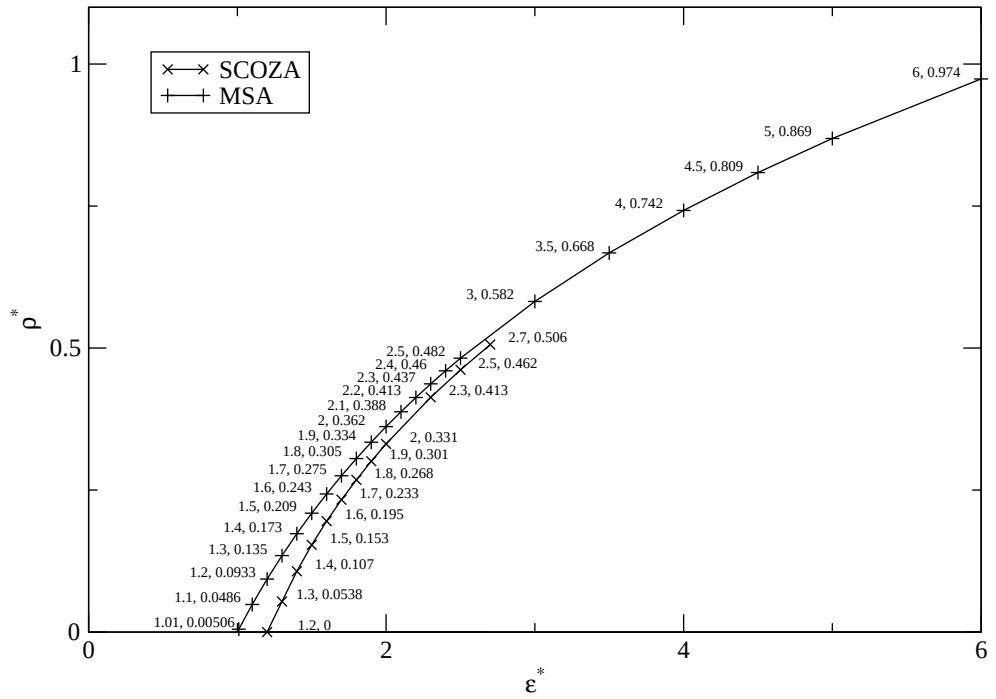

Figure 7.2: The ϱ^*-ε^*-region where the MSA and the SCOZA yield unphysical results for $g(0)$. For every reduced energy $\varepsilon^* > \varepsilon_{\text{lim}}$ there is a reduced density ϱ^*_{lim} below which $g(0) < 0$. For the MSA, $\varepsilon^*_{\text{lim}} = 1.0$, for the SCOZA, $\varepsilon^*_{\text{lim}} \approx 1.2$. Values of $(\varepsilon^*, \varrho^*_{\text{lim}})$ are denoted in the plot.

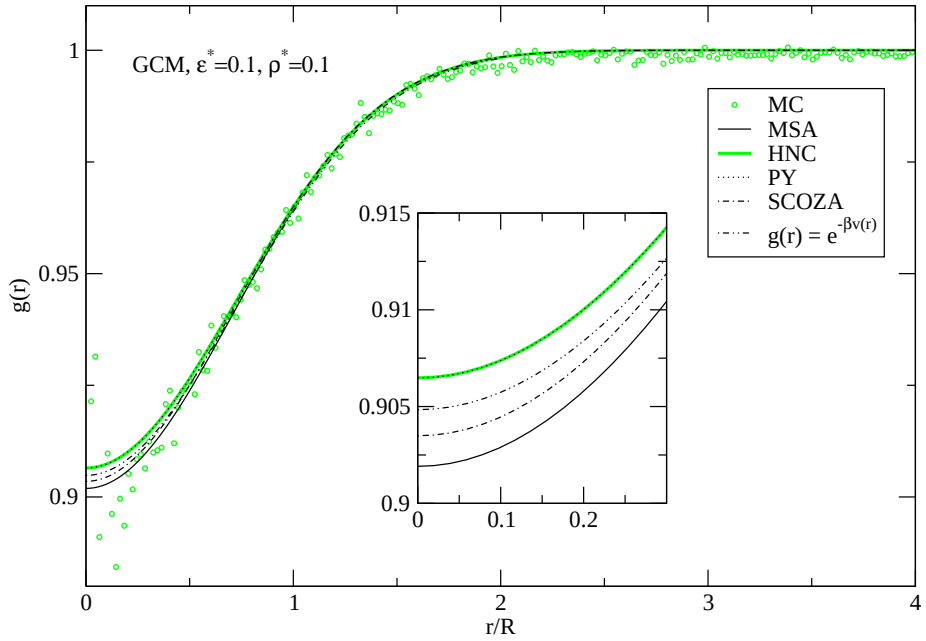

Figure 7.3: The radial distribution function $g(r)$ as a function of r/R: comparison of a MC simulation and solutions of the MSA, HNC, PY and SCOZA closures for the GCM at $\varepsilon^* = 0.1$ and $\varrho^* = 0.1$ as labelled. Here, the results of HNC and PY coincide. At such low reduced energies ε^* and reduced densities ϱ^*, the MC simulations are rather inefficient, and the results are strongly affected by statistical noise, especially at $r = 0$. Also, it can be seen that for the MC simulations $g(r) \to 1 - 1/N$. In this energy and density region, even the Boltzmann factor $e^{-\beta v(r)}$ is a good approximation for $g(r)$. The insert shows a detail of the plot for small r.

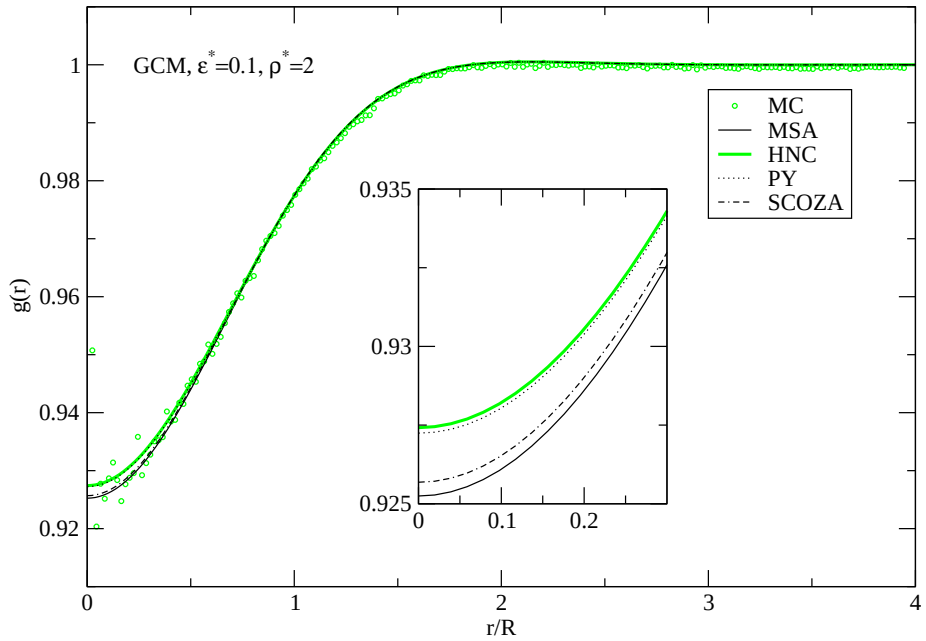

Figure 7.4: The same as figure 7.3 for the GCM at $\varepsilon^* = 0.1$ and $\varrho^* = 2$.

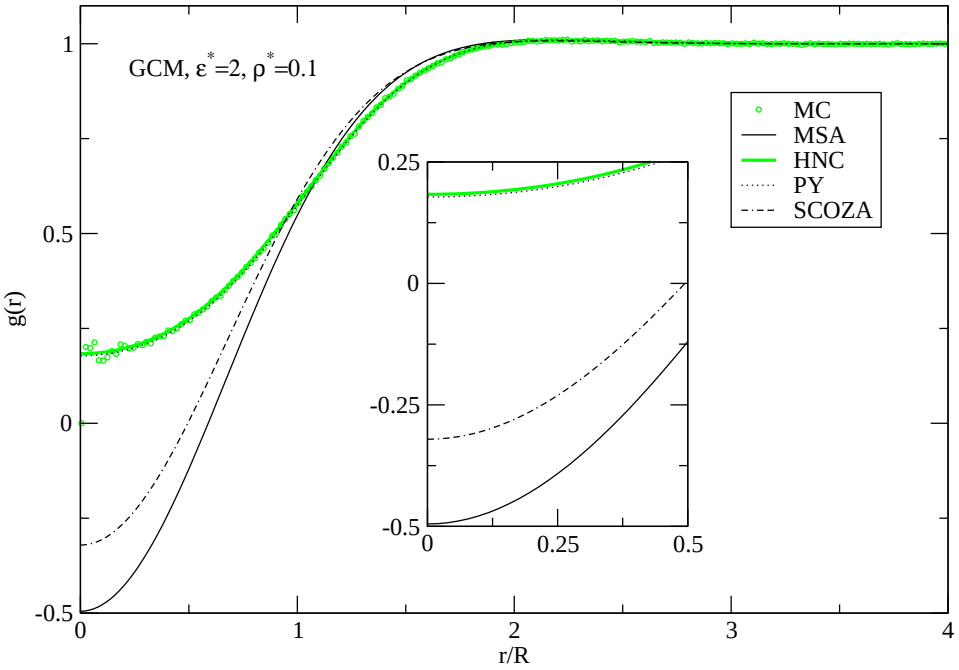

Figure 7.5: The same as figure 7.3 for the GCM at $\varepsilon^* = 2$ and $\varrho^* = 0.1$. Once again, the results of HNC and PY coincide. Note that for this energy and density, the MSA and SCOZA give unphysical results.

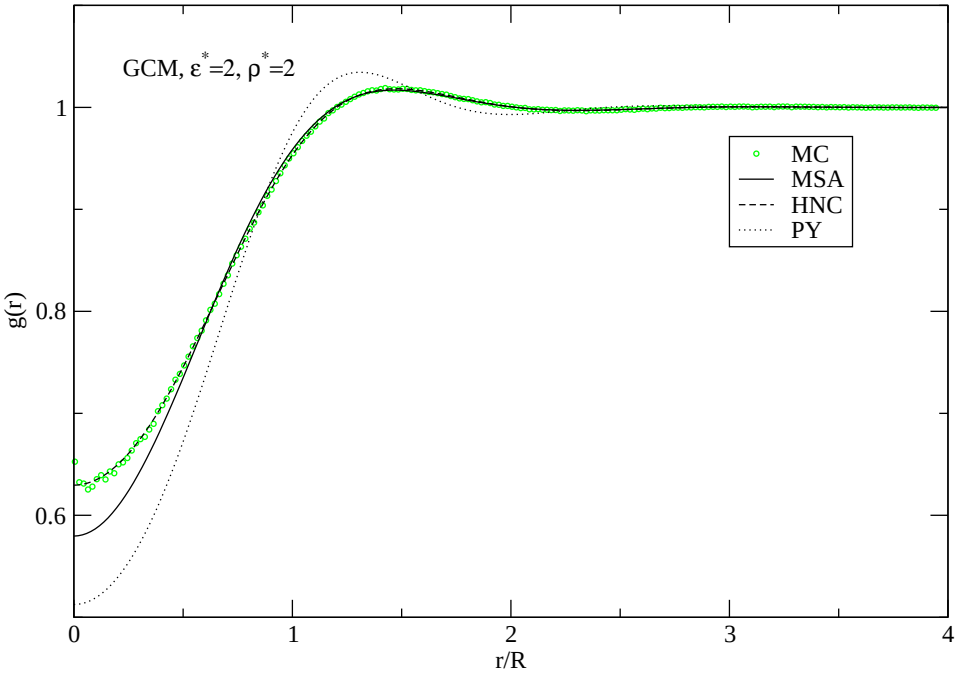

Figure 7.6: The same as figure 7.3 for the GCM at $\varepsilon^* = 2$ and $\varrho^* = 2$. Here it can be seen that the solution of $g(r)$ according to PY has oscillatory behaviour. For this value of ε^* and ϱ^*, no solution was obtained for the SCOZA.

7.1.2 The Dimensionless Equation of State Z

This section is organised as follows: First, we are going to take a detailed look at the results for the dimensionless equation of state $Z = \beta P/\varrho$ obtained by the different thermodynamic routes of the considered IETs. After this, we show the plots of a comparison of the results for Z obtained by the MSA compared to the data from MC simulations at $\varepsilon^* = 0.1$ and $\varepsilon^* = 2$ and varying ϱ^*, followed by an analogous comparison of the HNC closure, the PY approximation and the SCOZA with the MC data. We then present the results of the closures at a high reduced energy $\varepsilon^* = 10$ and very low reduced densities $\varrho^* \leq 0.05$. Finally, we show a plot of Z according to the different thermodynamic routes of all closures considered in this thesis. In the captions of the figures we comment on observed phenomenona.

Despite its simple form, the MSA yields good results for the calculation of $Z = \beta P/\varrho$ for low energies and high densities. The virial and energy route are thermodynamically consistent for the GCM in the case of the MSA [see (4.23) and (4.28)], and for low energies the results of these two routes are in good agreement with the results obtained by MC simulations. For higher energies ($\varepsilon^* \gtrsim 7$) and very low densities ($\varrho^* \lesssim 0.05$), the virial and energy route yield qualitatively incorrect results, i.e. for *increasing* density the pressure *decreases*. Upon further increasing the density, the pressure then starts to increase and the MSA results approach the HNC results. Compared to MC simulations, the compressibility route overestimates the pressure, but it never generates qualitatively wrong results (see figure 7.15).

Out of the closures studied in this thesis, the HNC closure yields the best results for the GCM in comparison to the MC data. The energy and virial route appear to be thermodynamically consistent and differences are probably due to slight numerical inaccuracies. The compressibility route underestimates the pressure.

PY provides very good results for low energies. The results for virial and energy route are once again very close. On increasing the energy and the density, the compressibility route tends to gradually overestimate the pressure.

The SCOZA closure yields results very close to the results of the MSA virial route.

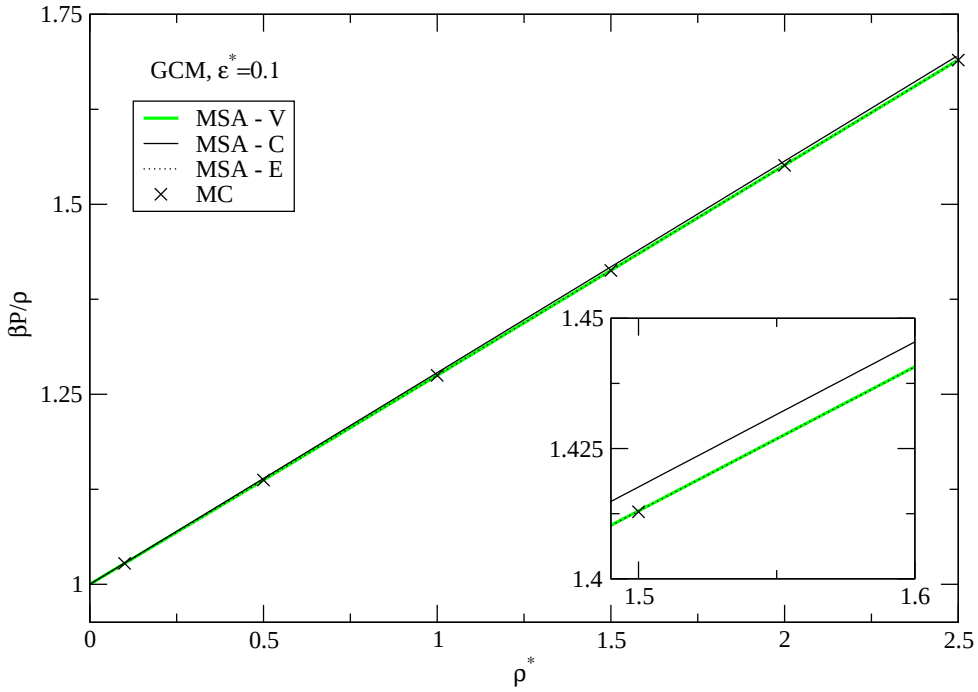

Figure 7.7: Comparison of $\beta P/\varrho$ as a function of ϱ^* for the GCM according to virial (V), compressibility (C) and energy (E) route of the MSA and according to MC simulations for $\varepsilon^* = 0.1$ as labelled. The compressibility route overestimates the pressure. The insert shows a detail of the plot.

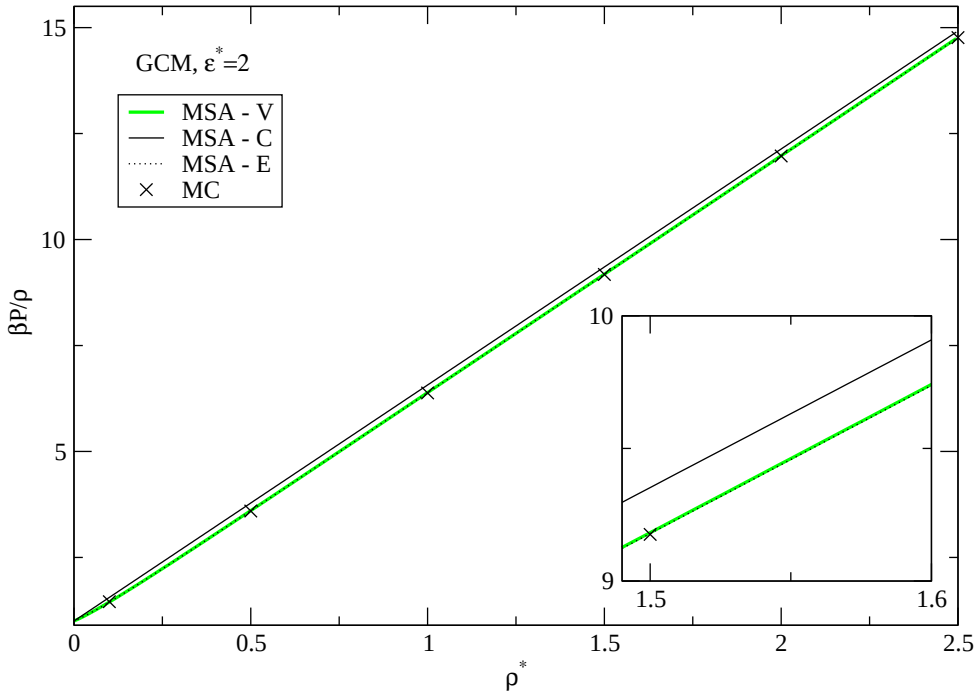

Figure 7.8: The same as figure 7.7 for $\varepsilon^* = 2$.

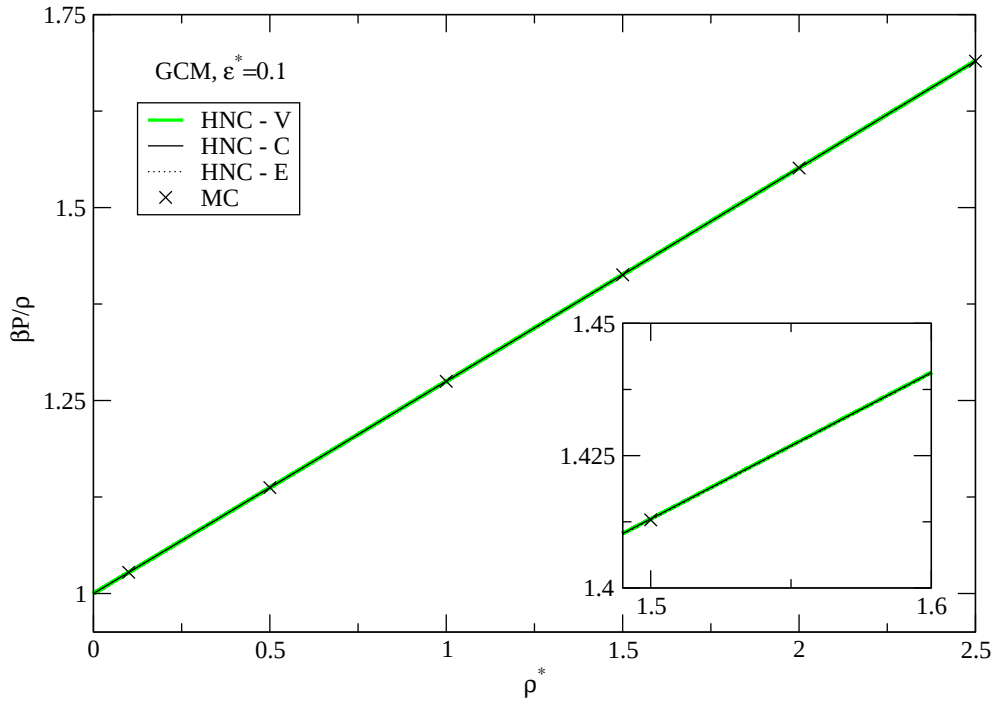

Figure 7.9: Comparison of $\beta P/\varrho$ as a function of ϱ^* for the GCM according to virial (V), compressibility (C) and energy (E) route of the HNC closure and according to MC simulations for $\varepsilon^* = 0.1$ as labelled. For such low energies, the results of the three routes coincide.

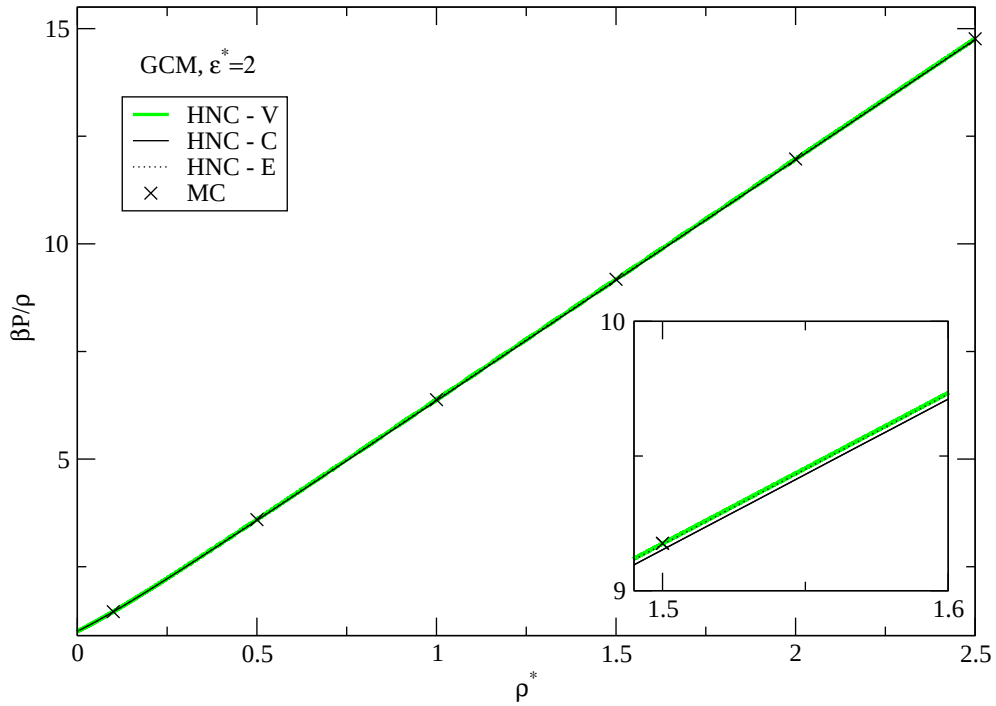

Figure 7.10: The same as figure 7.9 for $\varepsilon^* = 2$. Here, the compressibility route slightly underestimates $\beta P/\varrho$.

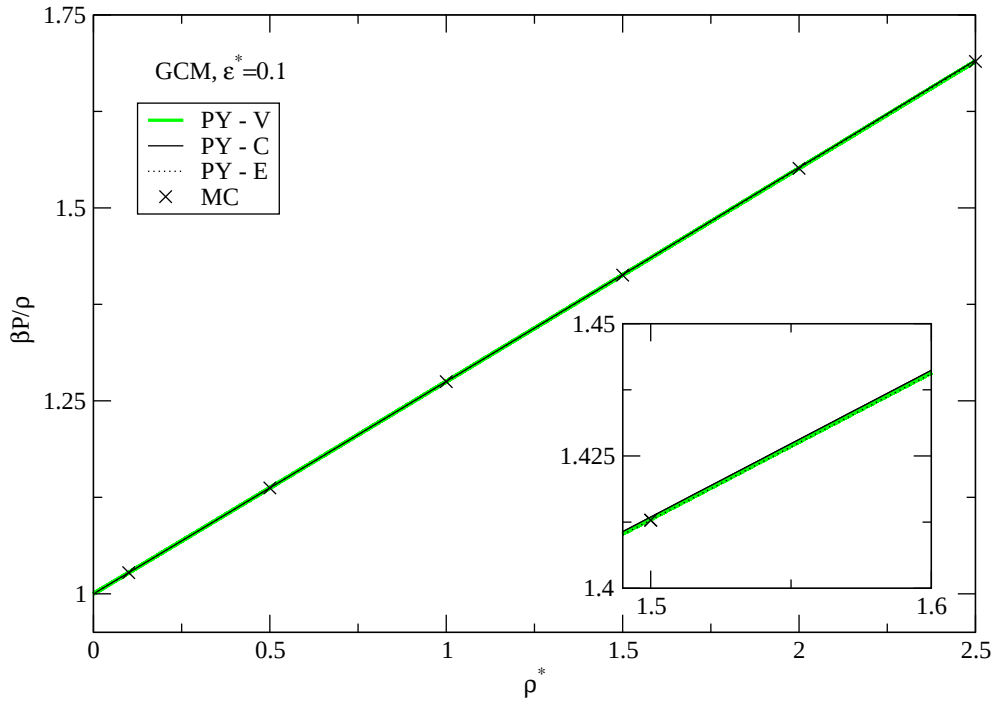

Figure 7.11: Comparison of $\beta P/\varrho$ as a function of ϱ^* for the GCM according to virial (V), compressibility (C) and energy (E) route of the PY closure and according to MC simulations for $\varepsilon^* = 0.1$ as labelled. For such low energies, the results nearly coincide.

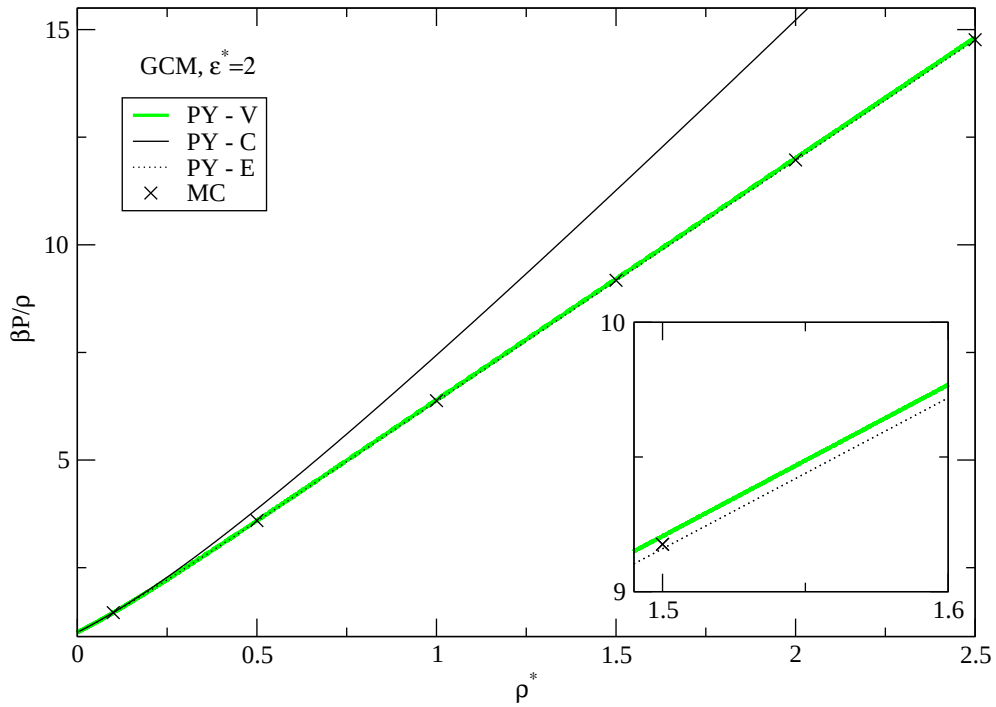

Figure 7.12: The same as figure 7.11 for $\varepsilon^* = 2$. In this energy region, the compressibility route yields poor results.

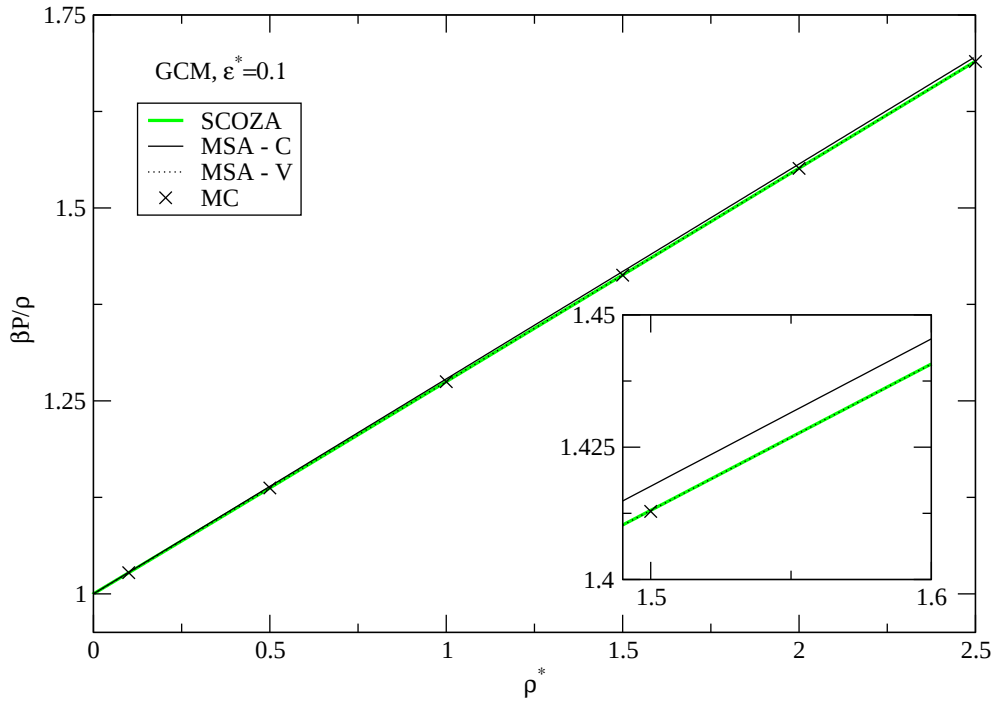

Figure 7.13: Comparison of $\beta P/\varrho$ as a function of ϱ^* for the GCM according to the SCOZA, the compressibility (C) and virial (V) route of the MSA and MC simulations for $\varepsilon^* = 0.1$.

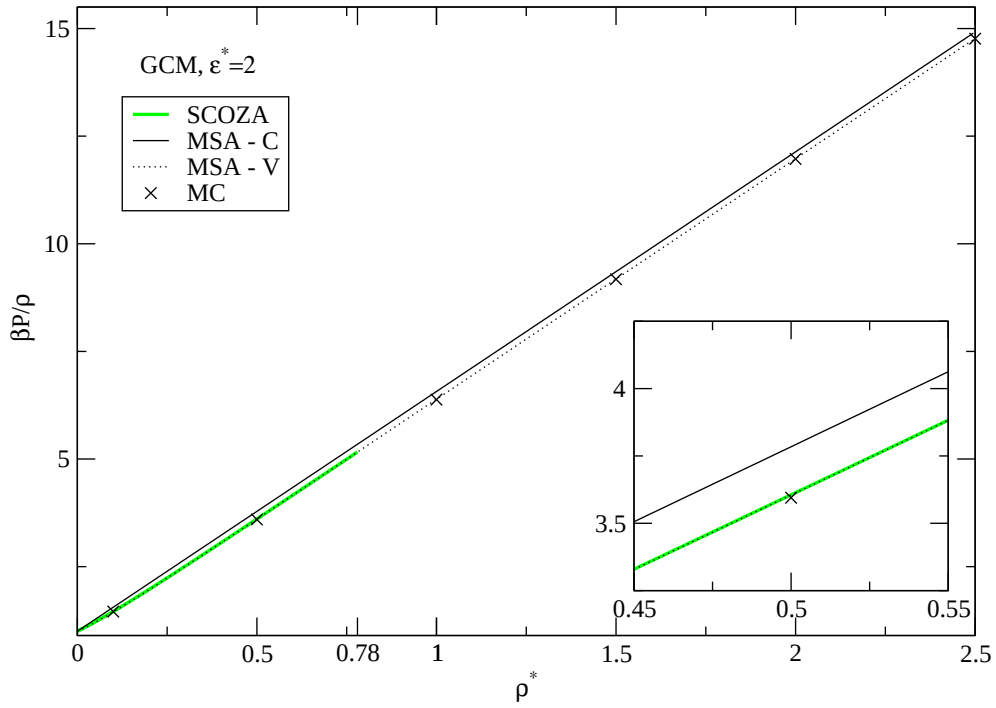

Figure 7.14: The same as figure 7.13 for $\varepsilon^* = 2$. The results of the SCOZA and of the virial route of the MSA coincide. For the SCOZA, a solution could only be obtained up to a reduced density $\varrho^* = 0.78$.

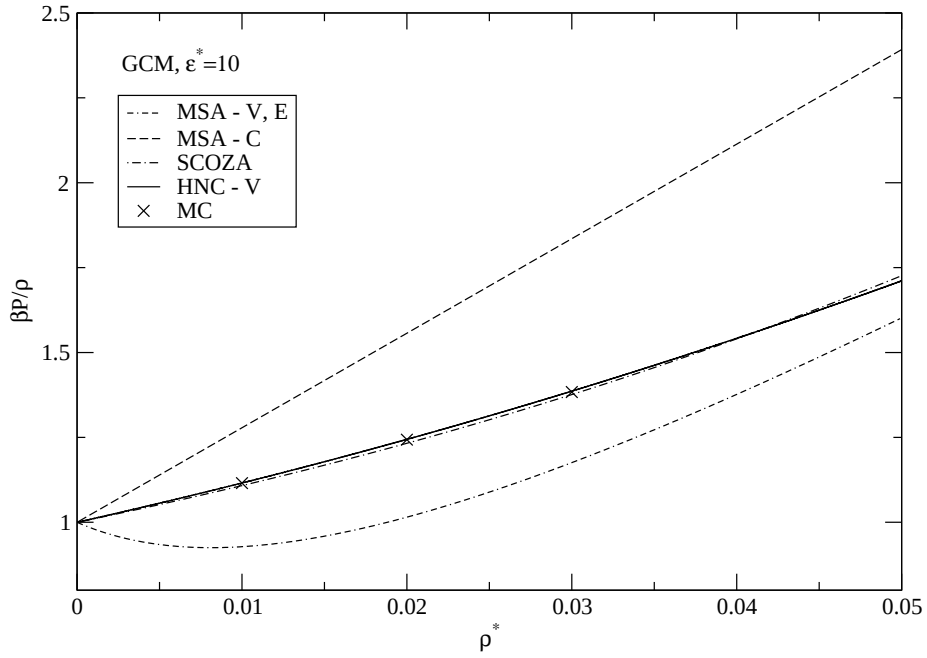

Figure 7.15: The results of $\beta P/\varrho$ as a function of ϱ^* of the compressibility, virial and energy route according to the MSA compared to the data obtained by the SCOZA, the virial route of the HNC approximation and MC simulations for $\varepsilon^* = 10$ and very low densities. In this region, the virial resp. the energy route of the MSA yield qualitatively wrong results.

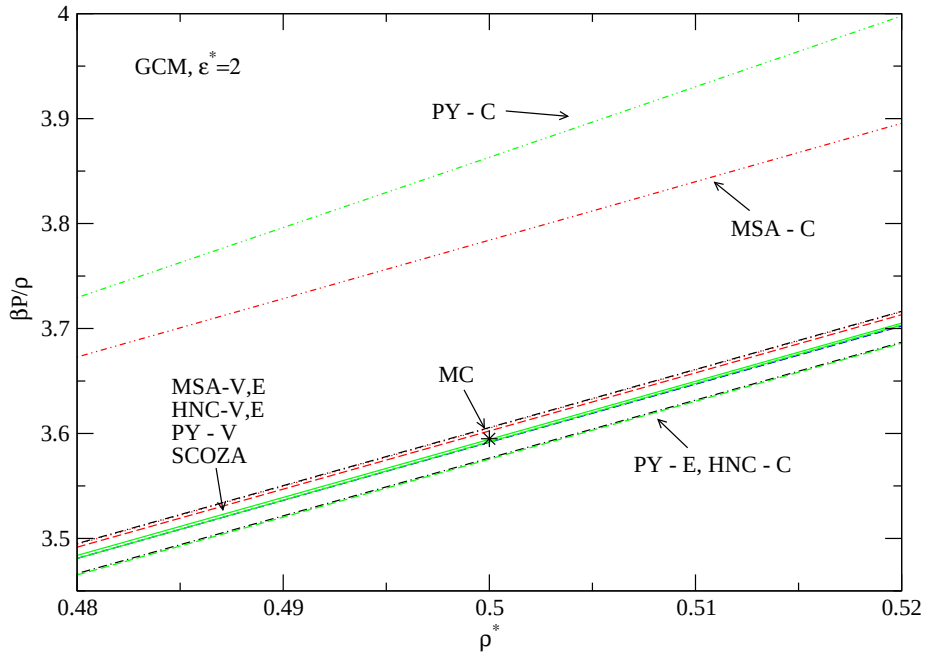

Figure 7.16: A detail of the plot of $\beta P/\varrho$ as a function of ϱ^* for the different routes of MSA, HNC, PY and SCOZA as labelled. The result of a MC simulation is plotted for comparison. It can be seen that most of the results are very close together. Differences might not only stem from the diversity of the approximations but also from numerical errors that emerge for instance when having to numerically integrate already numerically integrated results.

7.2 The Double Gaussian Core Model

In this thesis, we studied the DGCM potential with $\eta = 0.5$ and $\zeta = 1.1$, i.e.

$$v(r) = \varepsilon \left[e^{-(r/R)^2} - 0.5\, e^{-(r/1.1R)^2} \right], \tag{7.4}$$

which has a very small attractive part (see figure 7.17).
As $\eta\zeta^3 = 0.6655$, the stability criterion (4.41) is fulfilled for this potential.[2]

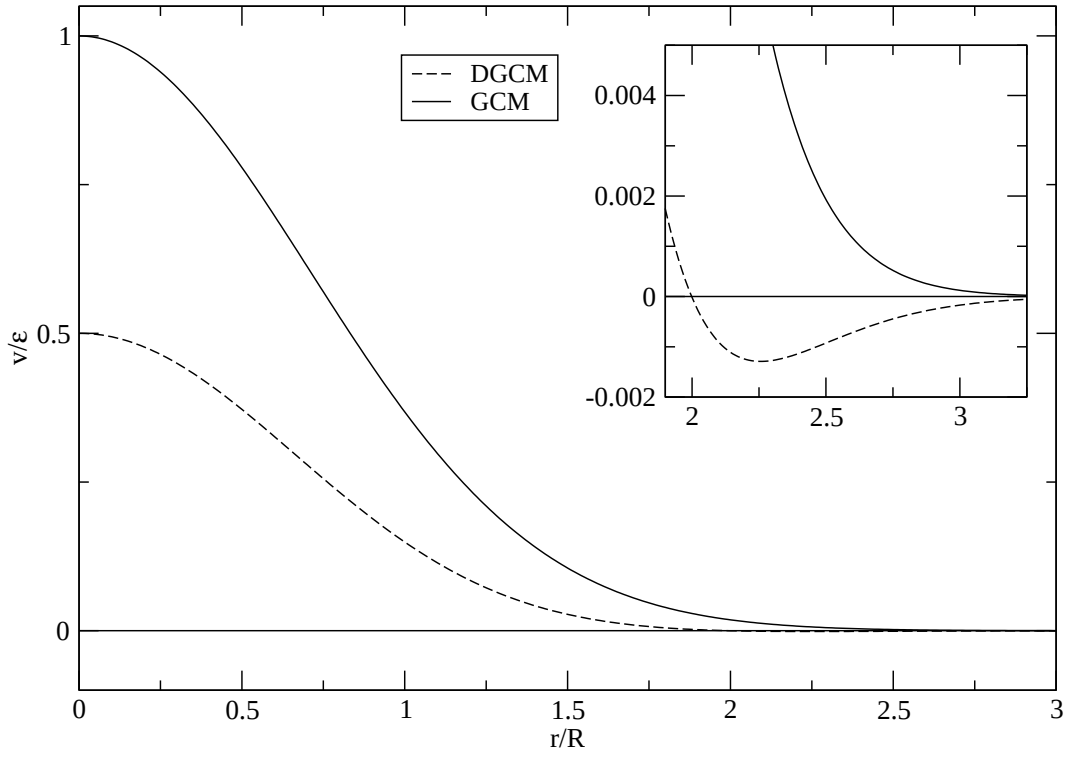

Figure 7.17: The DGCM [see (7.4)] with $\eta = 0.5$ and $\zeta = 1.1$ compared to the GCM.

7.2.1 The Radial Distribution Function $g(r)$

This section is organised as follows: First, we verbally present the results obtained for $g(r)$ by the different closures in detail. After this, we show plots of $g(r)$ obtained by the different closures and compare these results to the data obtained by MC simulations for $\varepsilon^* = 0.1$ and $\varepsilon^* = 2$ at a low reduced density $\varrho^* = 0.1$ and a high reduced density $\varrho^* = 2$ and for $\varepsilon^* = 5$ at $\varrho^* = 0.1$ and $\varrho^* = 10$. In the captions of the figures we comment on observed phenomenona.

For the DGCM, the MSA yields its best results for $g(r)$ for high densities and high energies while it is unphysical - just as in the case of the GCM - for high energies and low densities.

[2] However, this does not rigorously prove that this potential is in fact stable.

Out of the studied closures, the HNC results agree best with the MC simulations. The HNC approximation converges everywhere in the energy-density area tested in this thesis ($\varepsilon^* \leq 95$ and $\varrho^* \leq 100$).

The PY closure yields nearly the same results as the HNC closure for low energies and low densities, while for high energies and high densities its solution for $g(r)$ has an oscillating structure and is worse than the solution according to the MSA. On further increasing the energy, the Broyles algorithm for the PY approximation ceases to converge and it is impossible to obtain a solution for $g(r)$ even when starting from the HNC solution for $g(r)$ as an initial guess for the Broyles iteration.

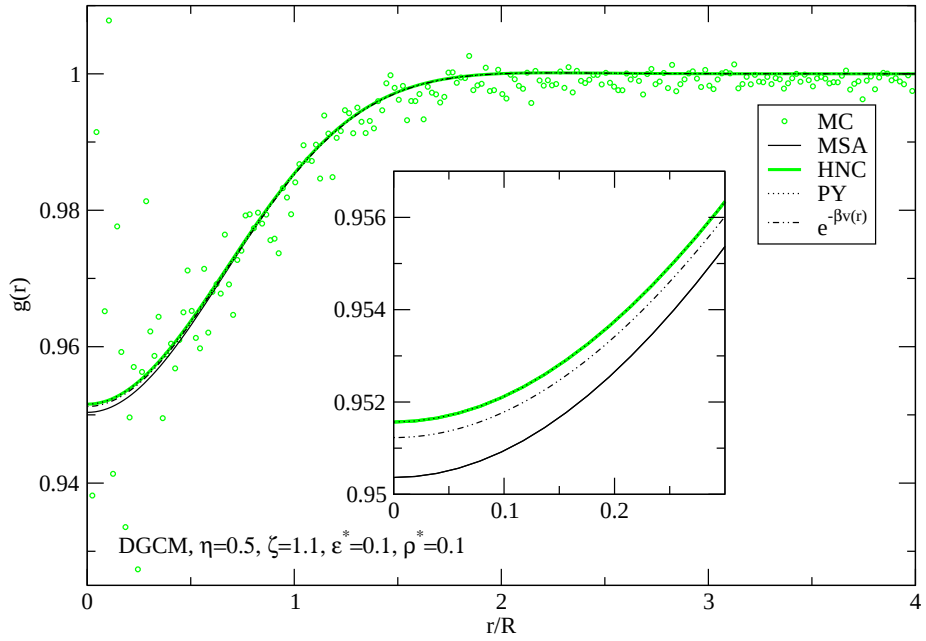

Figure 7.18: Comparison of $g(r)$ as a function of r/R according to MC simulations and solutions of the MSA, HNC and PY closures for the DGCM with $\eta = 0.5$ and $\zeta = 1.1$ at $\varepsilon^* = 0.1$ and $\varrho^* = 0.1$ as labelled. The results obtained by PY and HNC coincide. At such low reduced energies ε^* and reduced densities ϱ^*, the MC simulations are rather inefficient, and the results are strongly affected by statistical noise, especially at $r = 0$. Also, it can be seen that for the MC simulations $g(r) \to 1 - 1/N$. In this energy and density region, the Boltzmann factor $e^- \beta v(r)$ is a good approximation for $g(r)$. The insert shows a detail of the plot for small r.

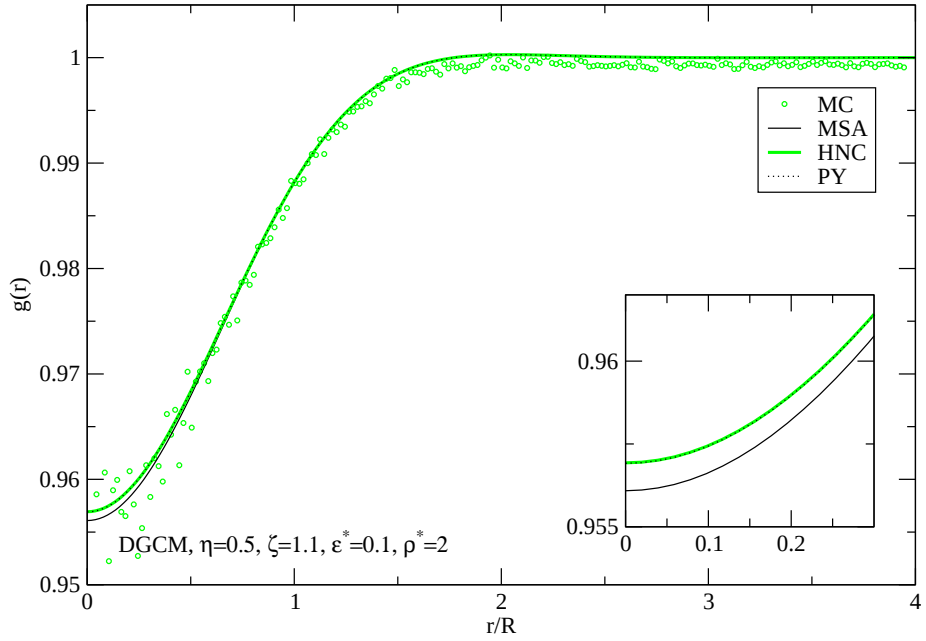

Figure 7.19: The same as figure 7.18 for $\varepsilon^* = 0.1$ and $\varrho^* = 2$.

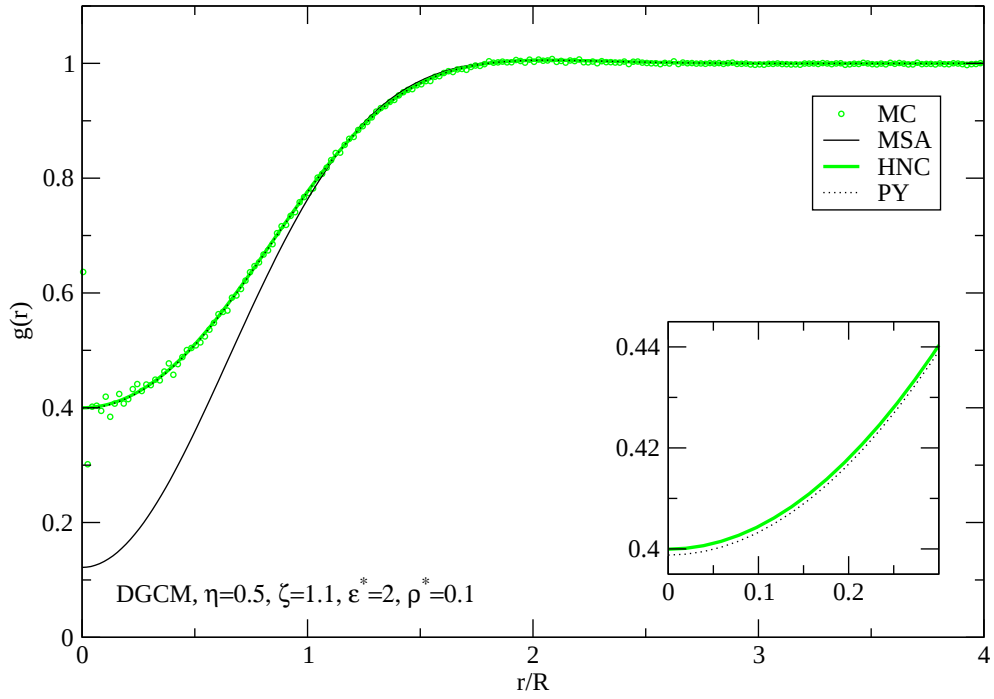

Figure 7.20: The same as figure 7.18 at $\varepsilon^* = 2$ and $\varrho^* = 0.1$. Here, the MSA is a rather poor approximation.

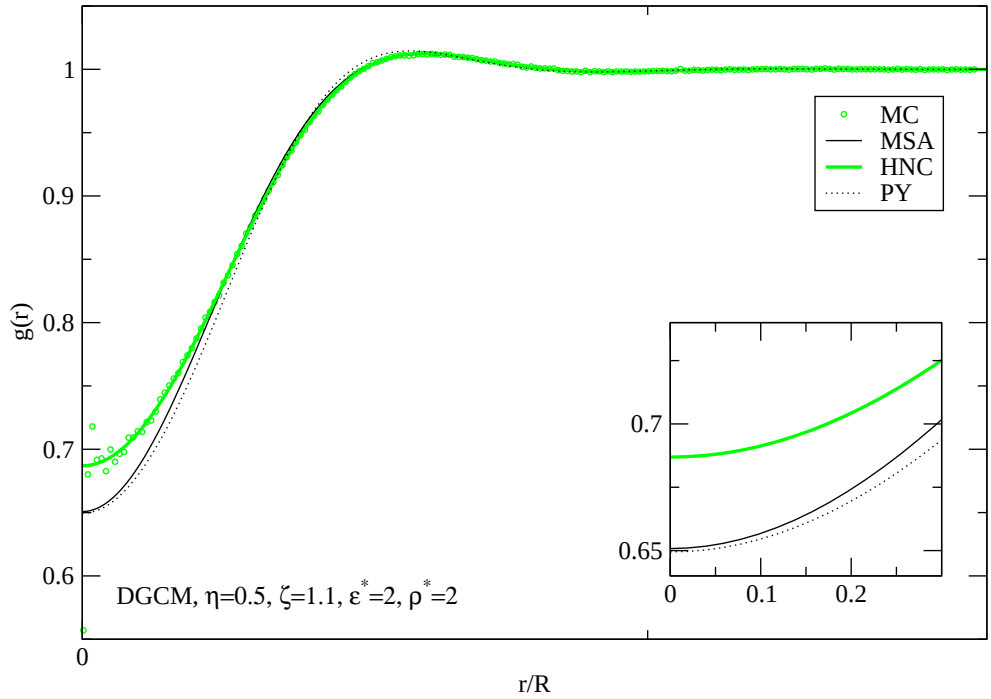

Figure 7.21: The same as figure 7.18 at $\varepsilon^* = 2$ and $\varrho^* = 2$. At this reduced energy and reduced density, the HNC and the PY solution for $g(r)$ do not coincide anymore.

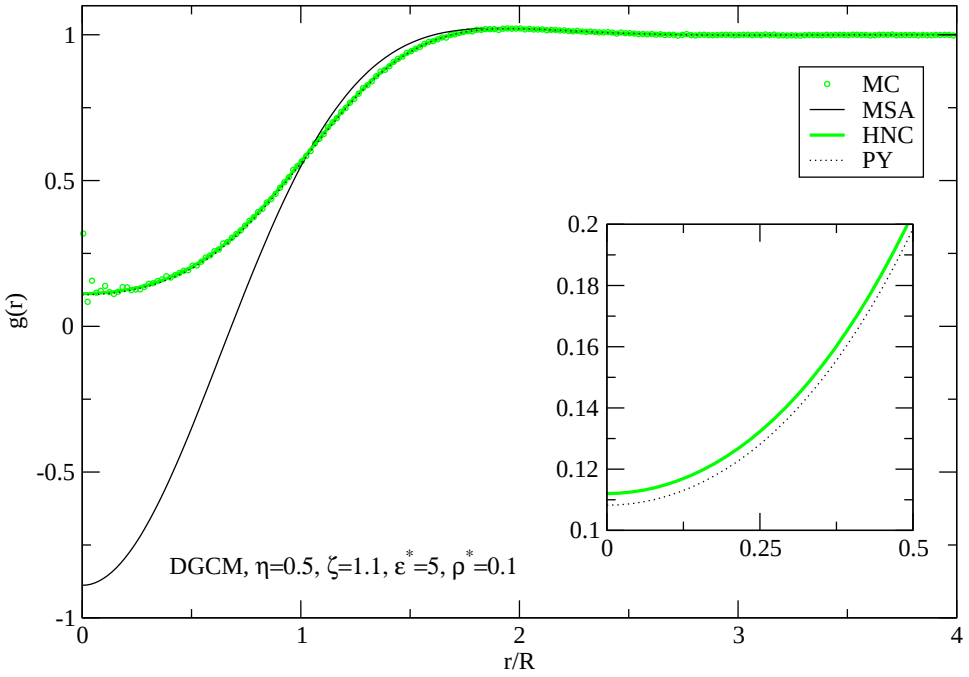

Figure 7.22: The same as figure 7.18 at $\varepsilon^* = 5$ and $\varrho^* = 0.1$. Here, the MSA yields unphysical results, whereas the results obtained by PY and HNC are very close together.

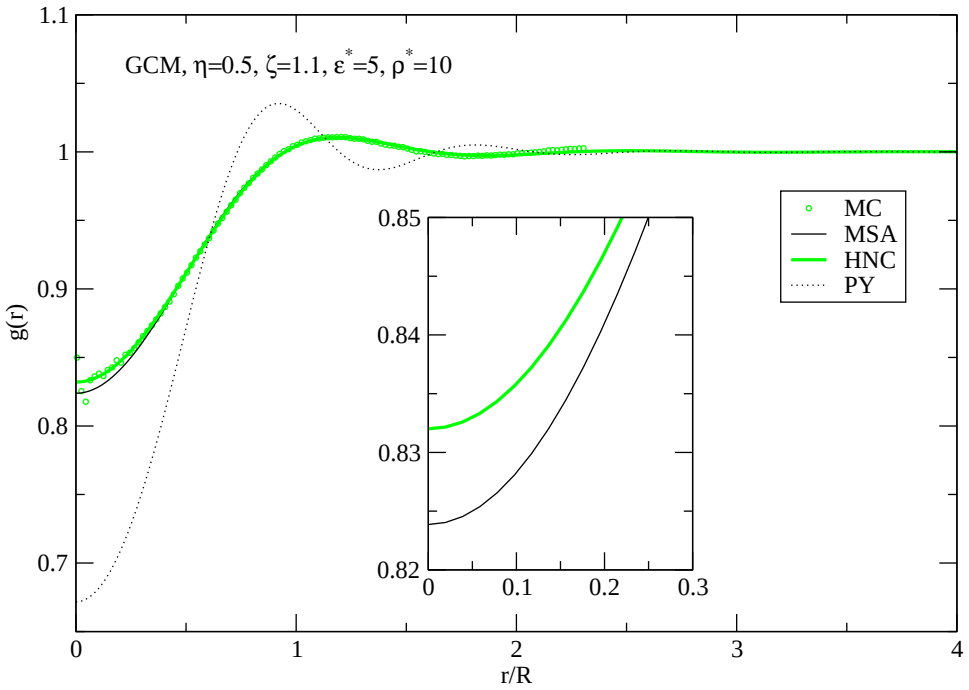

Figure 7.23: The same as figure 7.18 at $\varepsilon^* = 5$ and $\varrho^* = 10$. At this high reduced energy ε^* and high reduced density ϱ^*, the MSA is in good accordance with the results of the HNC approximation, whereas PY yields an qualitatively incorrect, oscillating structure in $g(r)$.

7.2.2 The Dimensionless Equation of State Z

This section is organised as follows: First, we are going to verbally explain the results for the dimensionless equation of state $Z = \beta P/\varrho$ according to the different IETs in detail. After this, we show the following plots: A comparison of the results for Z of the MSA compared to the data from MC simulations at $\varepsilon^* = 0.1$ and $\varepsilon^* = 2$ and varying ϱ^* followed by an analogous comparison of the HNC and the PY approximation with the MC data.

Though the virial and the energy equation according to the MSA cannot be solved analytically for the DGCM, these two routes appear to be thermodynamically consistent with differences only stemming from numerical inaccuracies, and for the parameters considered in this thesis they yield reasonable results. Just as with the GCM, the compressibility route overestimates the pressure in case of the MSA closure.

Compared to the results of MC simulations, the HNC closure yields the best results. The three routes appear to be nearly thermodynamically consistent.

PY works well for low energies and low densities. However, for higher energies, the compressibility route tends to overestimate the pressure for increasing density. Still, the energy and virial equation give good results.

Summarising, the DGCM potential with $\eta = 0.5$ and $\zeta = 1.1$ qualitatively shows the same behaviour as the GCM, and the IETs work just as well as for the GCM.

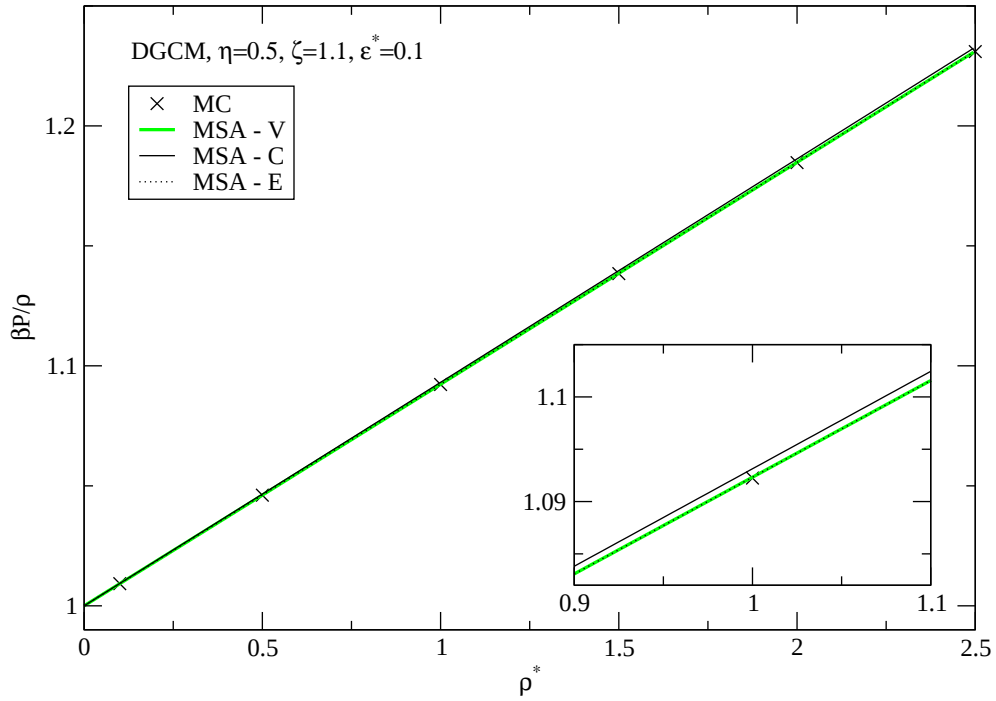

Figure 7.24: Comparison of $\beta P/\varrho$ as a function of ϱ^* for the DGCM with $\eta = 0.5$ and $\zeta = 1.1$ according to the MSA and MC simulations for $\varepsilon^* = 0.1$. The compressibility route overestimates the pressure.

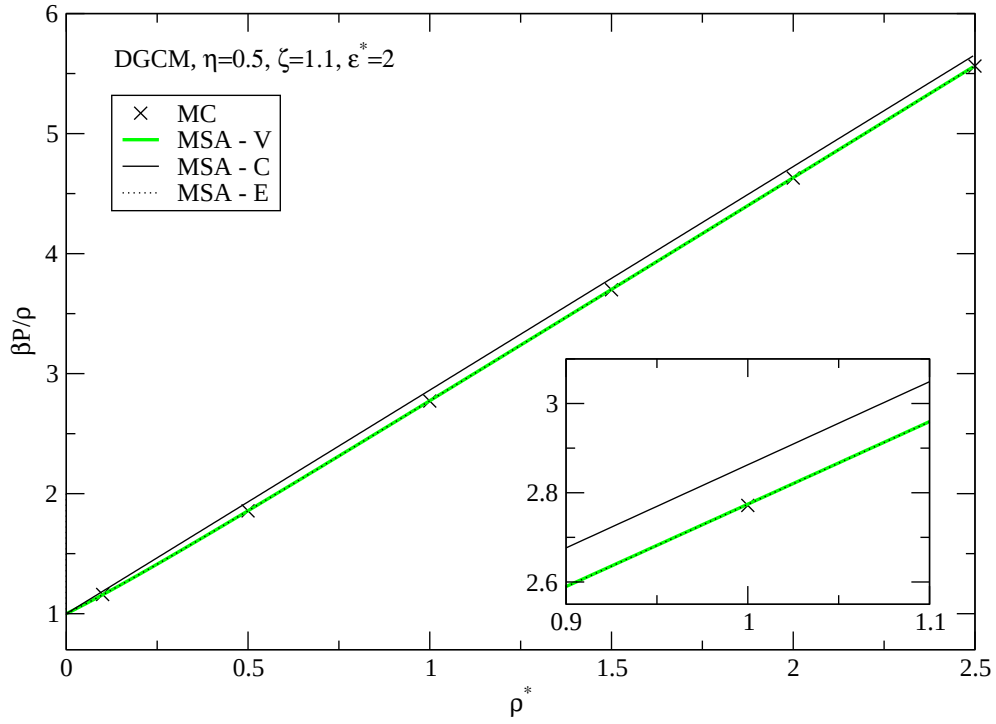

Figure 7.25: The same as figure 7.24 for $\varepsilon^* = 2$.

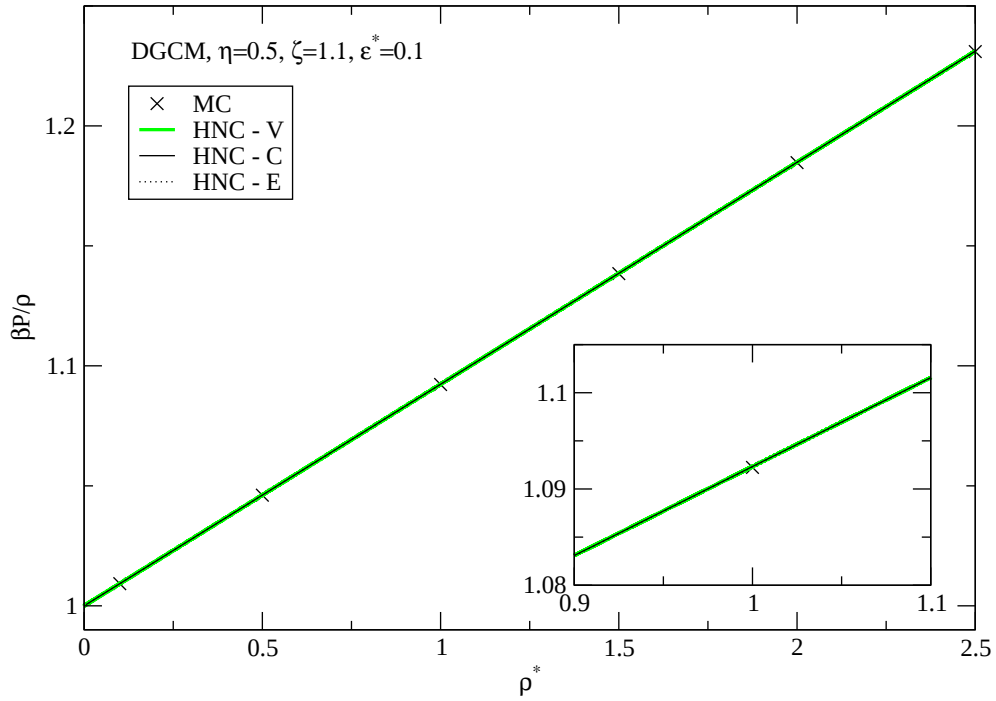

Figure 7.26: Comparison of $\beta P/\varrho$ as a function of ϱ^* for the DGCM with $\eta = 0.5$ and $\zeta = 1.1$ according to the HNC and MC simulations for $\varepsilon^* = 0.1$. The results of the three routes coincide.

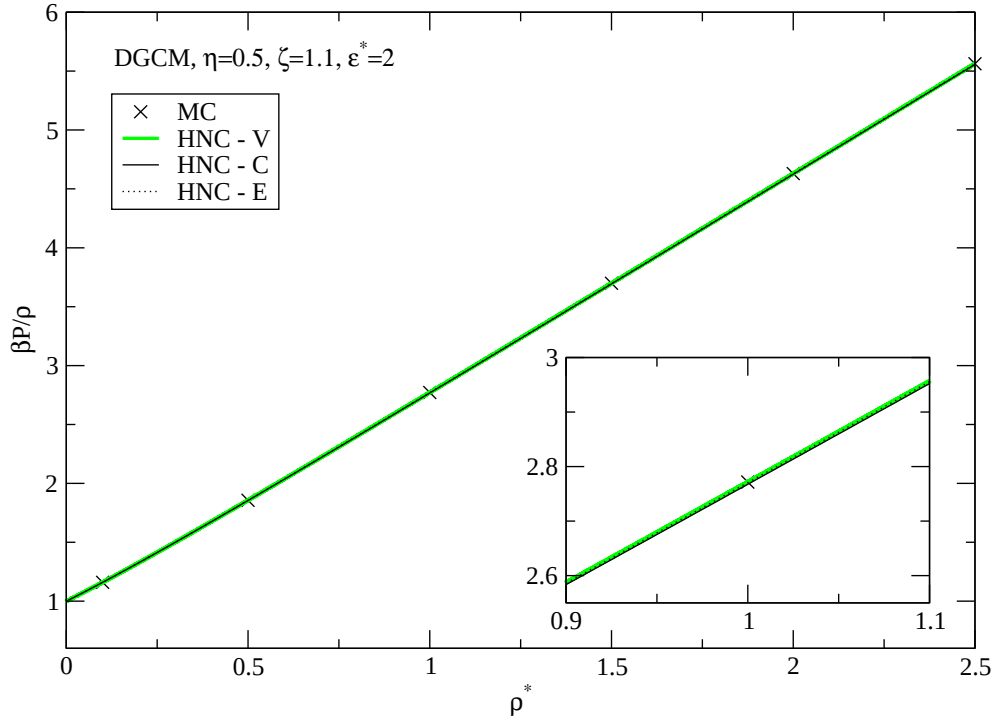

Figure 7.27: The same as figure 7.26 for $\varepsilon^* = 2$.

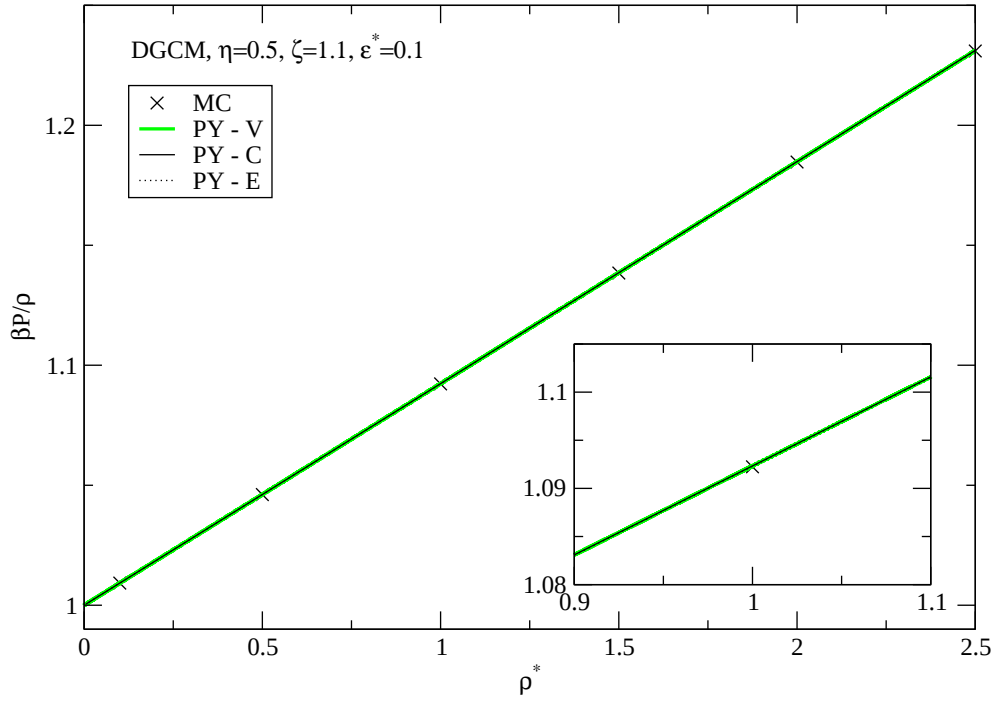

Figure 7.28: Comparison of $\beta P/\varrho$ as a function of ϱ^* for the DGCM with $\eta = 0.5$ and $\zeta = 1.1$ according to the PY and MC simulations for $\varepsilon^* = 0.1$. At this low reduced energy ε^*, the results of the three routes coincide.

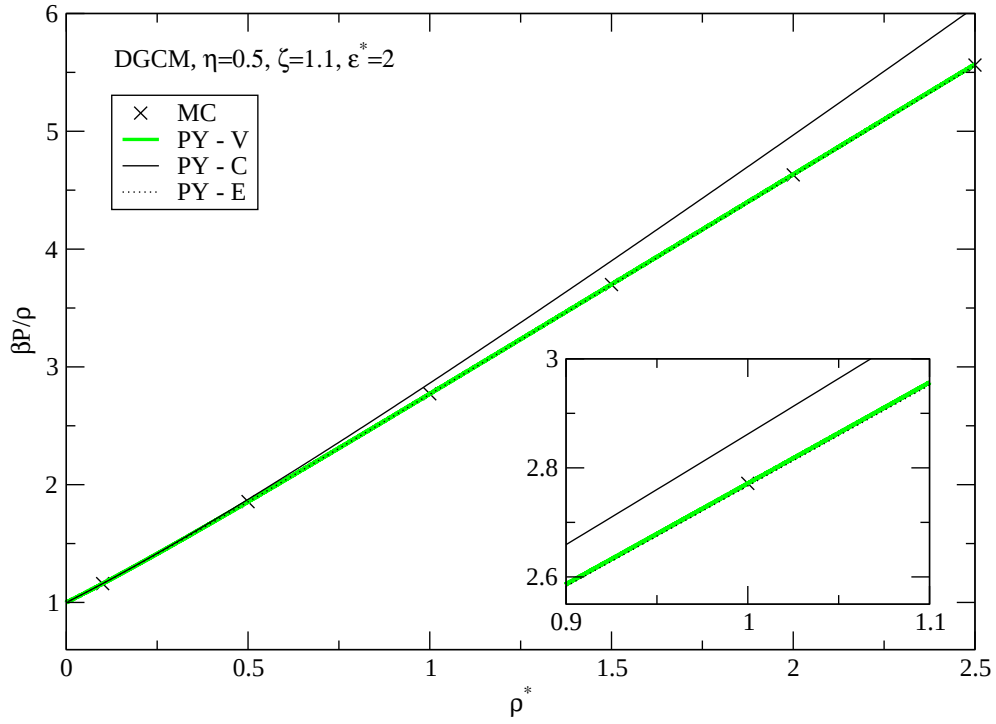

Figure 7.29: The same as figure 7.28 for $\varepsilon^* = 2$. In this energy region, the compressibility route yields poor results. Nevertheless, the other two routes still give reasonable results.

7.3 The Generalised Gaussian Core Model with Index n

To gain a better understanding of the decisive role of the detailed shape of the repulsive part of a bounded potential and as a counterpart to the GCM, which belongs to the Q^+-class, we have studied the GGCM-4 potential, which - according to section 4.6.1 - belongs to the $Q^{\pm}$-class:

$$v(r) = \varepsilon e^{-(r/R)^4}. \tag{7.5}$$

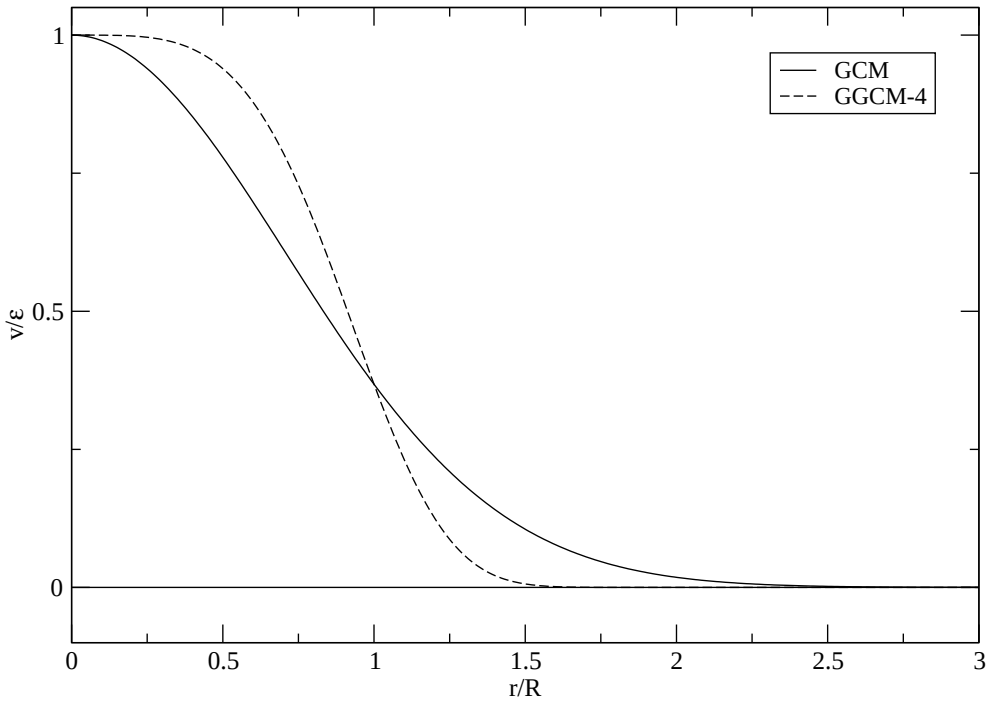

Figure 7.30: The GGCM-4 compared to the GCM.

Thus, as a main difference to the GCM which shows re-entrant melting, we expect clustering for this potential at every energy. According to our studies, for $\varepsilon^* = 0.1$, clustering only sets in at very high densities not analysed in this thesis and for $\varepsilon^* = 2$, the particles start to form clusters at $\varrho^* \sim 2.5$. This phenomenon can be seen, for instance, in figure 7.36 in the continuous rise of $g(0)$ for increasing density.

7.3.1 The Radial Distribution Function $g(r)$

This section is organised as follows: First, we are going to verbally discuss the results for $g(r)$ acquired by the different methods discussed in this thesis in detail. After this, we present plots of $g(r)$ obtained by the different closures and compare these results to the data obtained by MC

simulations for $\varepsilon^* = 0.1$ and $\varepsilon^* = 2$ at a low reduced density $\varrho^* = 0.1$ and a high reduced density $\varrho^* = 2$. Furthermore, we show a comparison of the MC results and data obtained by the MSA and the PY approximation for $g(r)$ for values of the reduced energy and reduced density where the system forms clusters ($\varepsilon^* = 2$ and $\varrho^* = 3.5$) and finally, we present a comparison of $g(r)$ as obtained by MC simulations for $\varepsilon^* = 2$ at various densities. In the captions of the figures we comment on observed phenomenona.

As can be seen from the MC simulations, for a fixed reduced energy the $r = 0$ value of $g(r)$ tends to increase with increasing density, and eventually $g(r)$ develops a very strong peak at the origin whose height may reach values much greater than 1. Apparently, since the interaction potential does not forbid particles to overlap, the system can lower its free energy by arranging the particles so that they form clusters in which more and more particles sit on top of each other as the density is raised.

As the GCM also allows close approaches or even overlaps between particles but does not show clustering, the reasons for this phenomenon apparently depend in some subtle way upon the functional form of the repulsion of the bounded potentials as reflected in the $Q^+/Q^\pm$ criterion.

For the GGCM-4, the MSA yields very good results in the homogeneous liquid phase. As soon as clustering sets in, the MSA at first tends to overestimate this phenomenon, whereas for strong clustering it underestimates $g(r)$ at small separations.

The HNC closure gives very good results as long as there is no clustering. As soon as this phenomenon sets in, the Broyles iteration does not converge any more (e.g. for $\varepsilon^* = 2$, no solution can be obtained for $\varrho^* \gtrsim 2.7$).

For low energies and low densities, the PY closure obtains nearly the same results as the HNC closure. When clustering sets in, the Broyles algorithm still converges, but the solution for $g(r)$ is qualitatively wrong as it is not able to reproduce the clustering.[3] For strong clustering, the Broyles algorithm ceases to converge (e.g. for $\varepsilon^* = 2$, no solution can be obtained for $\varrho^* \gtrsim 3.9$).

In order to understand why the IETs studied in this thesis break down for the GGCM-4, we have to consider the following: these IETs were applied very successfully to systems with strongly repulsive interactions, which forbid close approaches between particles (whereas the GGCM-4 potential permits close approaches and even overlaps). For the case of unbounded interactions that diverge at the origin, inaccuracies in the bridge function $B(r)$ especially for low r cause no serious problems, because if $v(r) \to \infty$ as $r \to 0$, we see that the exponential in (3.16) is dominated by the interaction and $g(r) \to 0$ for short separations. For bounded potentials on the other hand, $v(r)$ remains finite at all distances, so an accurate knowledge of the bridge function is essential to bring about an accurate theory of these systems. This is why especially for those regions of phase space where the particles form clusters, one has to resort to computer simulations in order to calculate the structure and thermodynamics of the system in a reliable way.

[3] It is not surprising that the PY approximation is unable to reproduce the clustering as it is a simple theory that was developed to describe the homogeneous and unordered fluid phase. Thus, it cannot be expected that this closure is even able to *qualitatively* describe this effect.

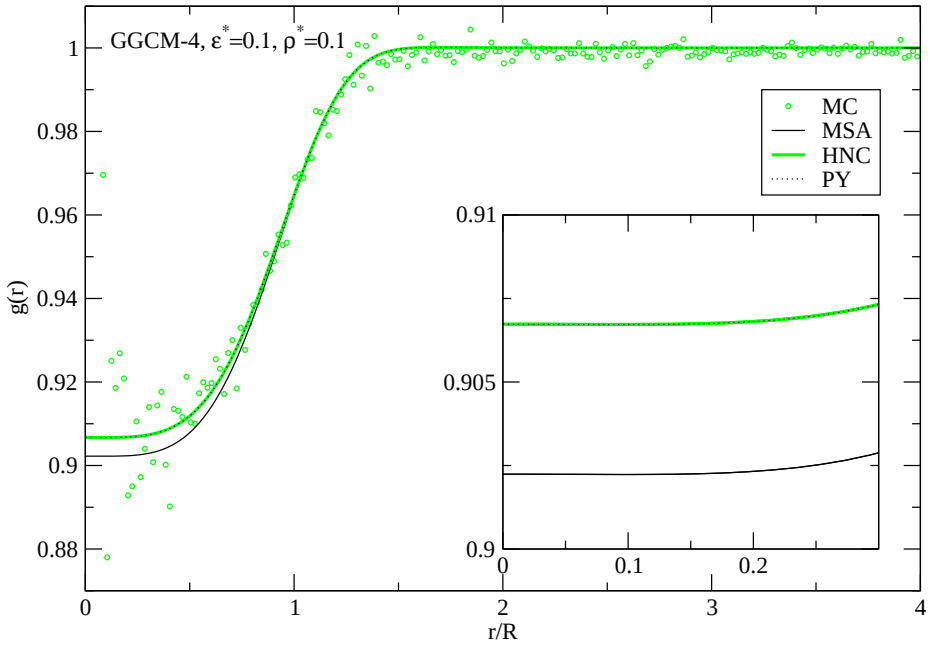

Figure 7.31: Comparison of the radial distribution function $g(r)$ as a function of r/R according to MC simulations and to the MSA, HNC and PY closures for the GGCM-4 at $\varepsilon^* = 0.1$ and $\varrho^* = 0.1$. The HNC and PY results coincide. At such low reduced energies ε^* and reduced densities ϱ^*, the MC simulations are rather inefficient, and the results are strongly affected by statistical noise, especially at $r = 0$. Also, it can be seen that for the MC simulations $g(r) \to 1 - 1/N$. The insert shows a detail of the plot for small r.

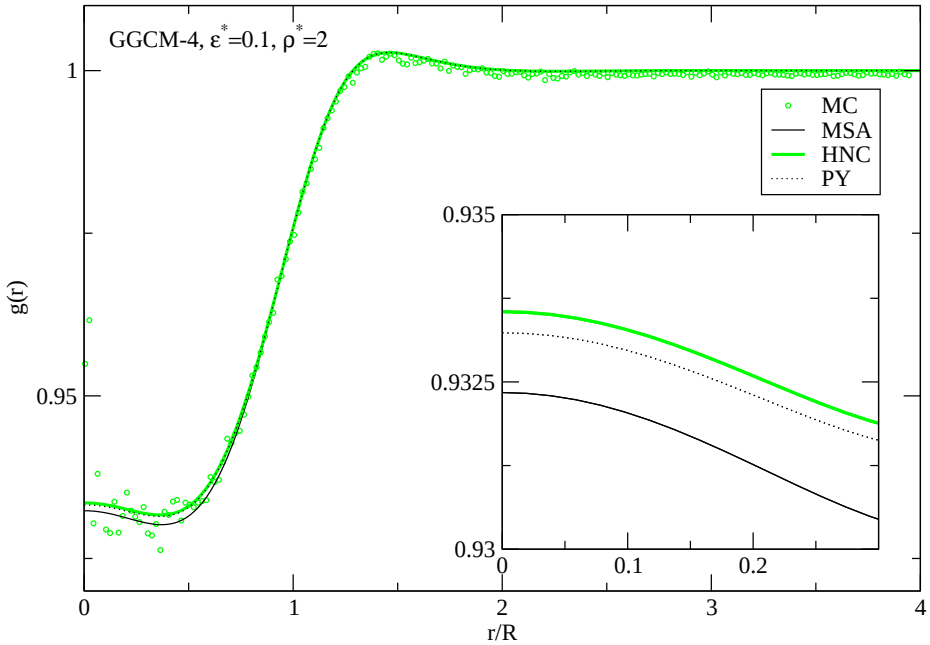

Figure 7.32: The same as figure 7.31 at $\varepsilon^* = 0.1$ and $\varrho^* = 2$.

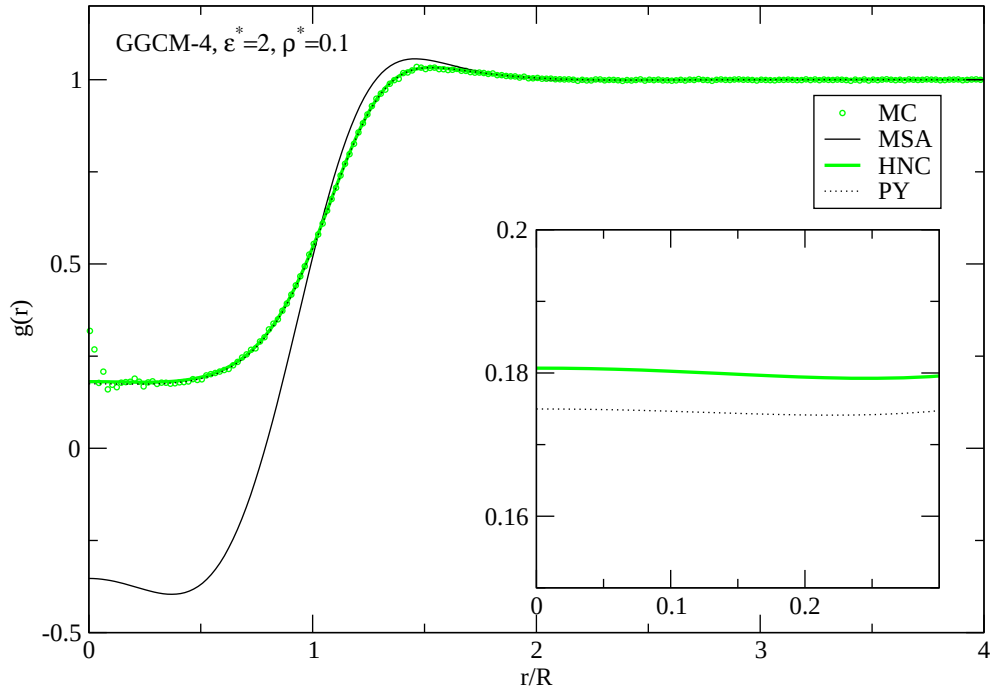

Figure 7.33: The same as figure 7.31 at $\varepsilon^* = 2$ and $\varrho^* = 0.1$. Here, the MSA obtains unphysical results.

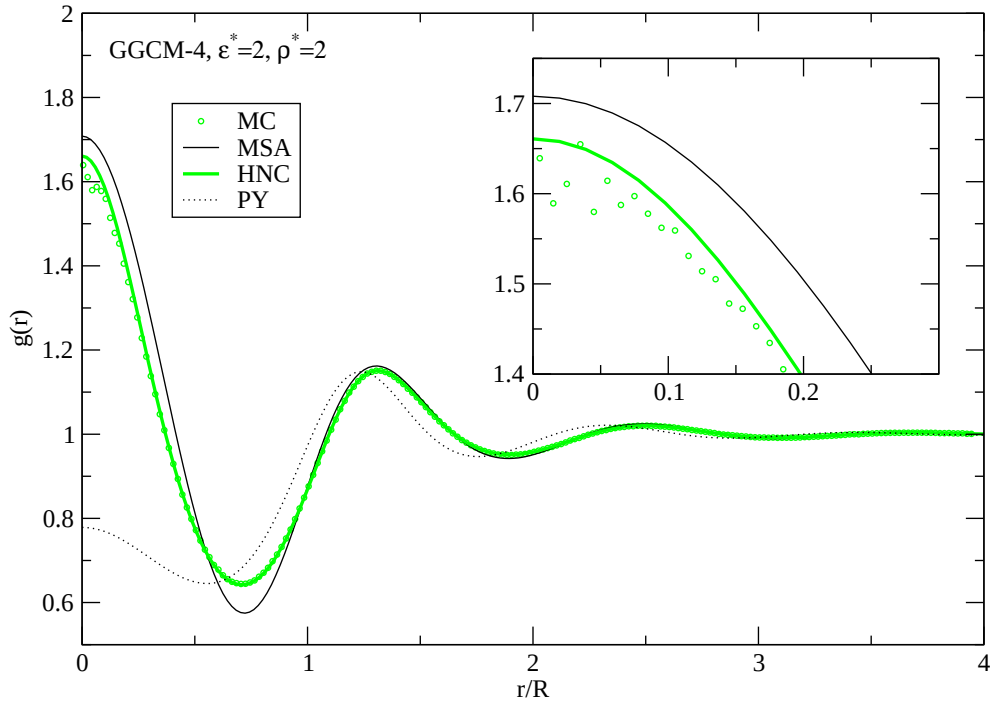

Figure 7.34: The same as figure 7.31 at $\varepsilon^* = 2$ and $\varrho^* = 2$. The MSA overestimates the onset of clustering a little bit, whereas PY underestimates it.

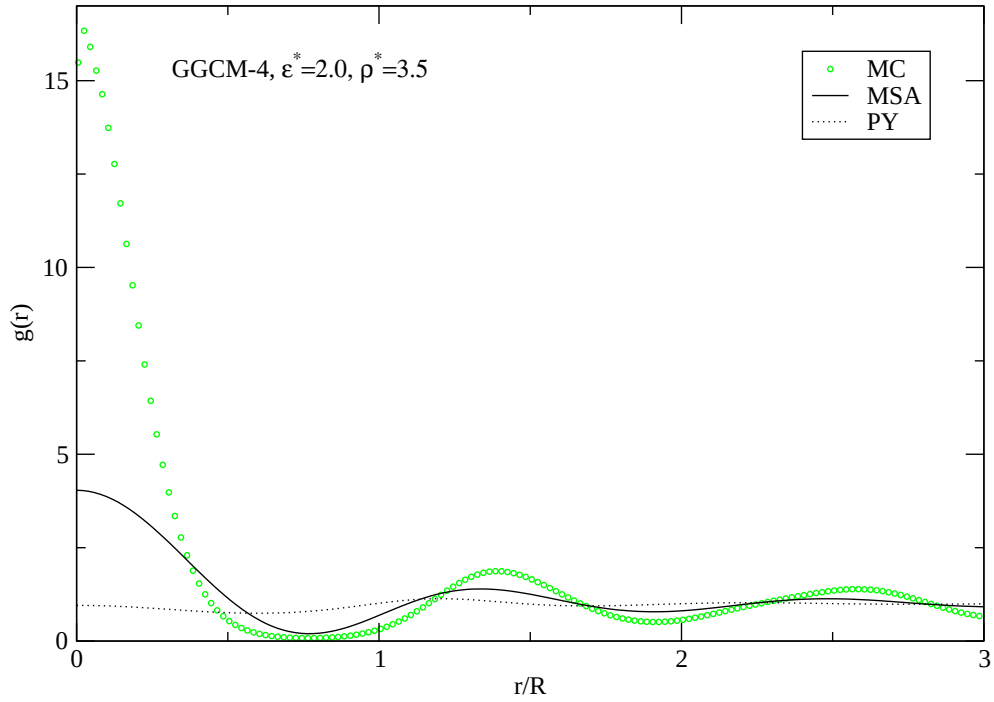

Figure 7.35: Comparison of the radial distribution function $g(r)$ as a function of r/R according to MC simulations and to the MSA and PY closures for the GGCM-4 at $\varepsilon^* = 2$ and $\varrho^* = 3.5$. Both the MSA and the PY approximation yield qualitatively wrong results.

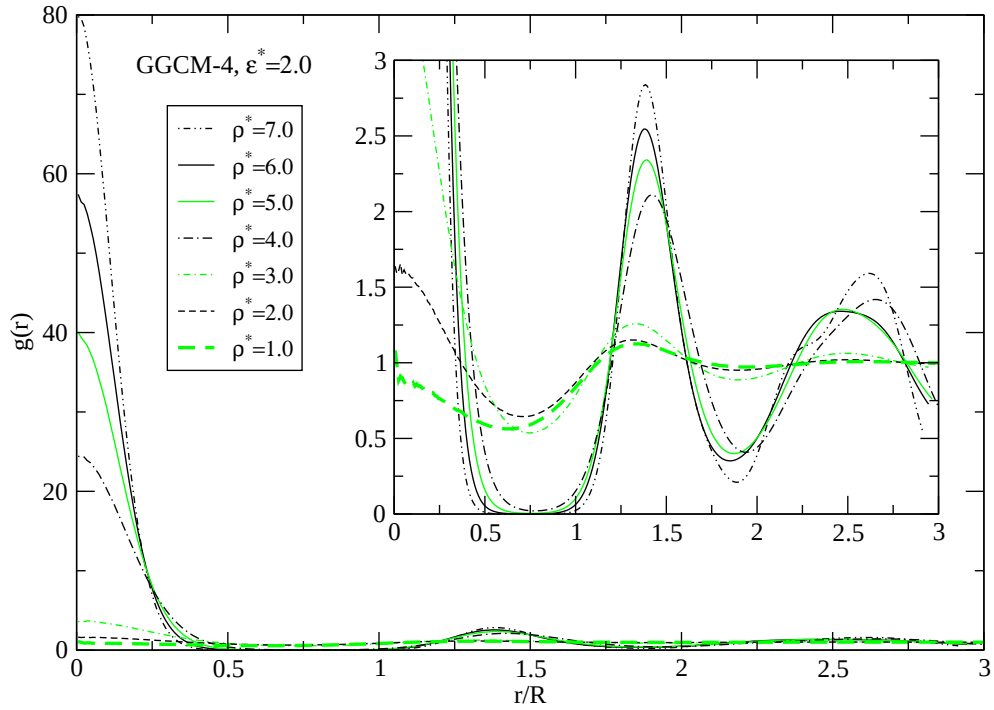

Figure 7.36: $g(r)$ as a function of r/R according to MC simulations at $\varepsilon^* = 2$ for different values of the reduced density ϱ^*. The rise in $g(0)$ for increasing density reflects the phenomenon of clustering, which starts at $\varrho^* \sim 2$. The insert shows a detail of the structure of $g(r)$.

7.3.2 Clustering

This section is organised as follows: First, we are going to verbally discuss the phenomenon of clustering. After this, we present a plot of the mean cluster size as obtained by MC simulations for different values of the reduced density ϱ^* and $\varepsilon^* = 2$. Next, we show the distribution of the cluster size at $\varepsilon^* = 2$ for various densities, followed by a series of snapshots of the particles in the MC simulations. In the captions of the figures we comment on observed phenomena.

Since IETs obviously fail to describe clustering in a quantitative way, MC simulations are the only reliable way to explore the region of the ε^*-ϱ^*-plane where the particles form clusters.

Likos showed in [25] that for $Q^{\pm}$-potentials it is estimated that the mean cluster size depends linearly on the density. Taking the r-value of the first minimum of $g(r)$ as a measure of distance for the average dimensions of a cluster and thus evaluating the mean size of the clusters in the MC simulations, linear regression analysis shows that Likos' assumption is justified for the data we obtained by simulations for the GGCM-4 (see figure 7.37).

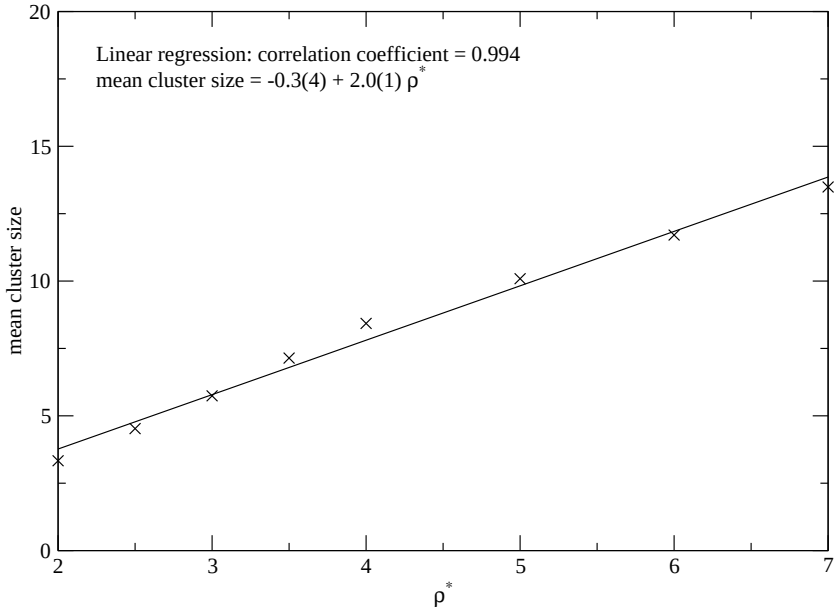

Figure 7.37: Linear regression for the mean cluster-size as a function of the reduced energy ϱ^* at $\varepsilon^* = 2$ for the GGCM-4.

The distribution of the cluster size at reduced energy $\varepsilon^* = 2$ is shown in figure 7.38 for different values of the reduced density ϱ^*.

Our simulations showed that for high densities the clusters tend to arrange themselves into regular, i.e. crystal structures. From the data obtained by the MC simulations, we speculate that the clusters "freeze" into fcc lattices. It is not yet clear if a crystal structure is the stable configuration for the clusters at all densities, as we also found fluid-like phases for values of the reduced density in between densities where crystal structures where found. Regarding this result, it has still to be

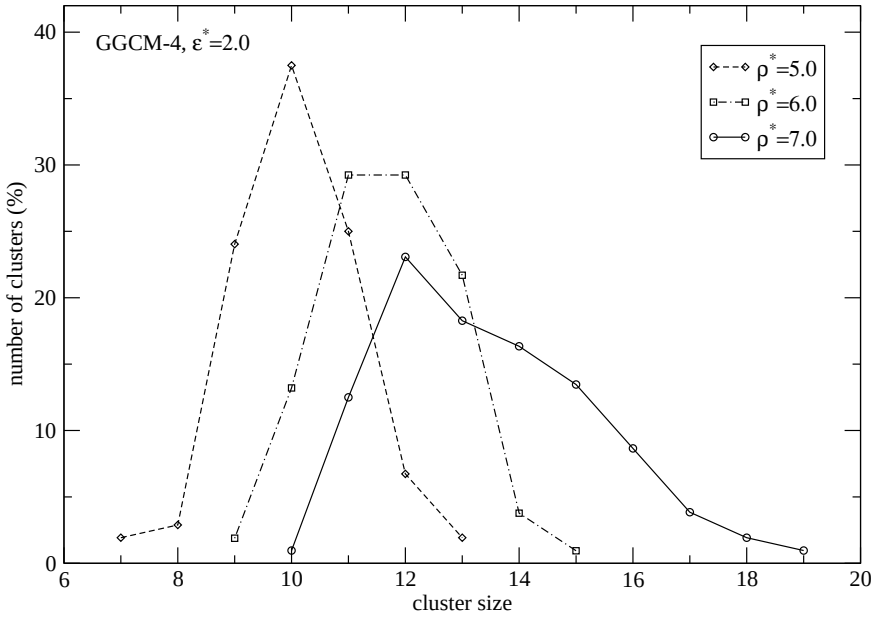

Figure 7.38: The distribution of the cluster size for the GGCM with $n = 4$ at reduced energy $\varepsilon^* = 2$ for different values of the reduced density ϱ^*.

clarified whether this was an artefact of the simulation or if it is a genuine physical phenomenon of the system. Also, it is not clear if the fcc lattice is the crystal structure with the lowest free energy. These questions are the object of future investigations, as they go beyond the scope of this work.

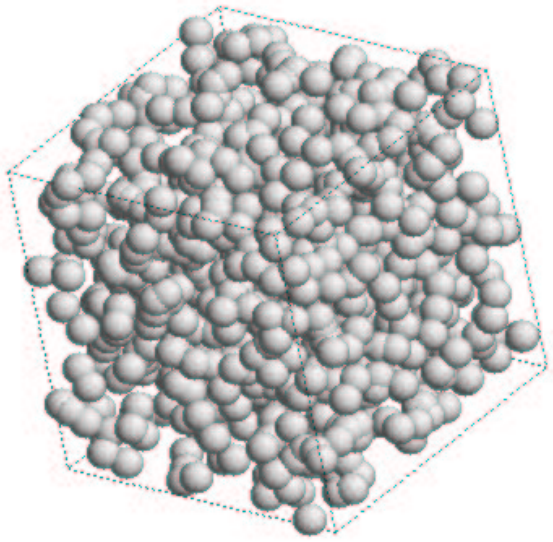

Figure 7.39: Snapshot of a MC simulation of 1 000 particles at $\varrho^* = 4$ and $\varepsilon^* = 0.1$ for the GGCM-4. For this energy and this density, no clustering takes place. Overlaps are purely incidental. For this and all following figures, the particles are displayed as spheres of an radius that was chosen arbitrarily so that one can easily see the discussed phenomenona.

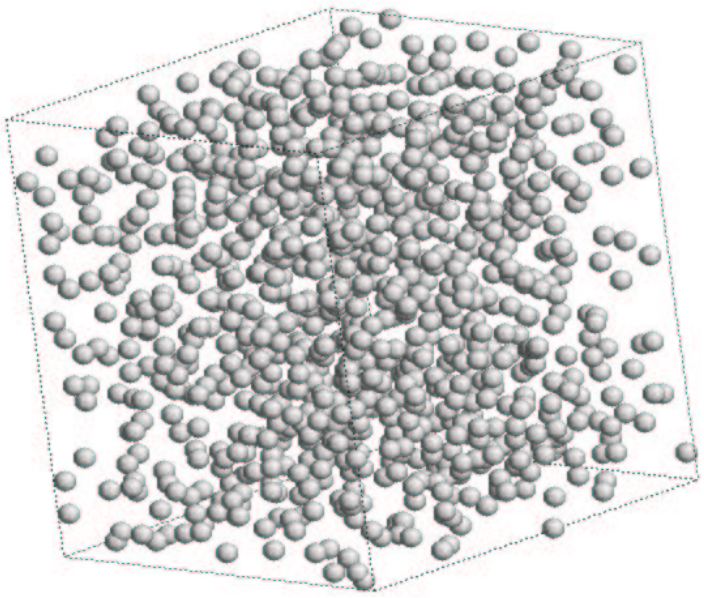

Figure 7.40: Snapshot of a MC simulation of 1 000 particles at $\varrho^* = 0.5$ and $\varepsilon^* = 2$ for the GGCM-4. For this energy and this density, no clustering takes place.

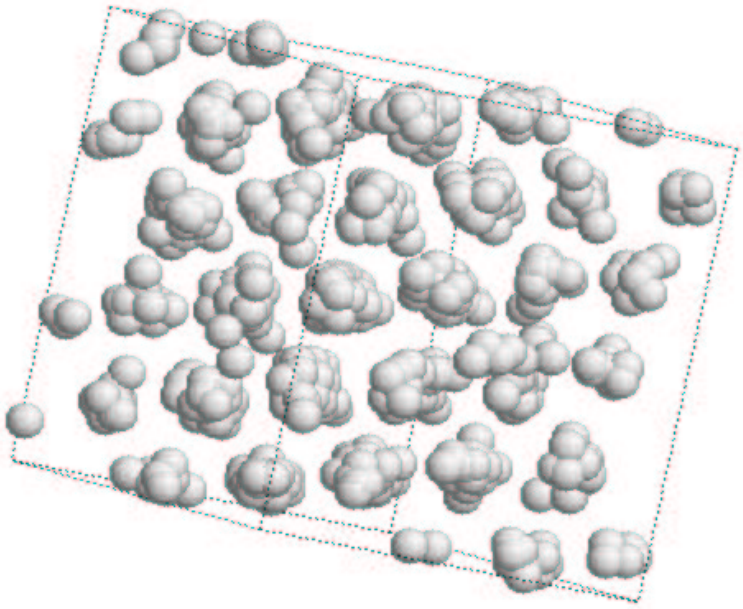

Figure 7.41: Snapshot of a MC simulation of 750 particles at $\varrho^* = 3.5$ and $\varepsilon^* = 2$ for the GGCM-4. Here, clustering has already set in. Symmetry can be found, although no readily identifiable, lattice structure has formed yet.

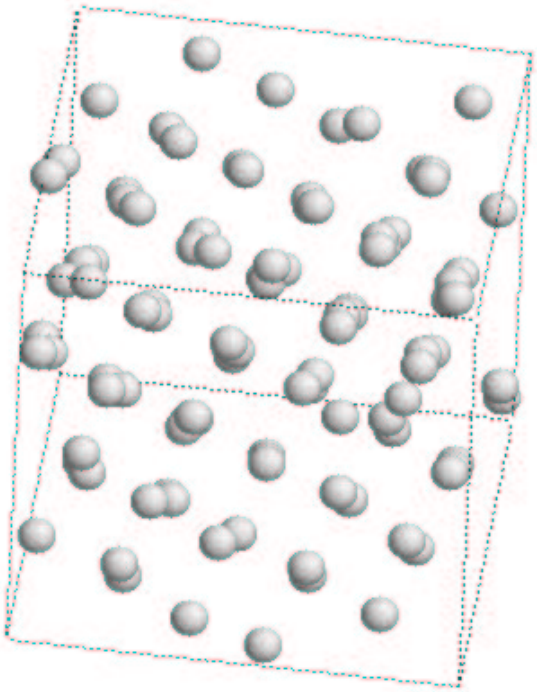

Figure 7.42: The centres of gravity of the same system displayed in figure 7.41.

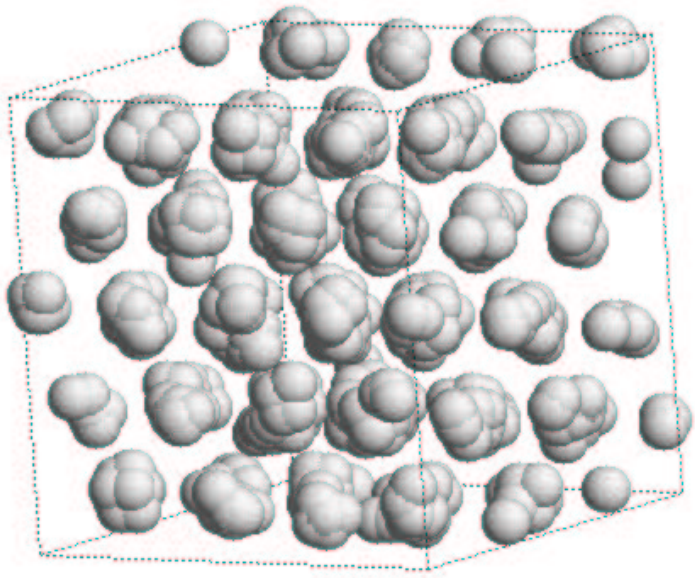

Figure 7.43: Snapshot of a MC simulation of 885 particles at $\varrho^* = 4.0$ and $\varepsilon^* = 2$ for the GGCM-4. The clusters appear to form a rather perfect lattice.

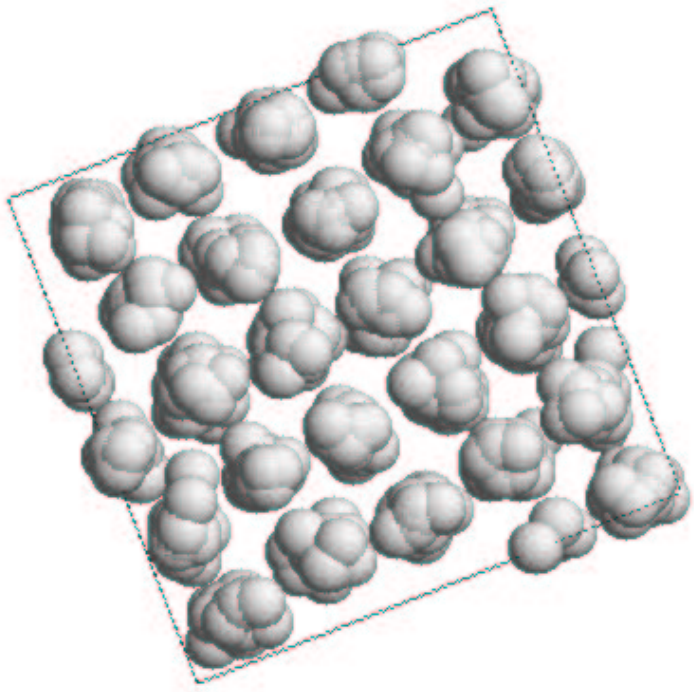

Figure 7.44: Another view of the snapshot of the MC simulation at $\varrho^* = 4.0$ and $\varepsilon^* = 2$ for the GGCM-4.

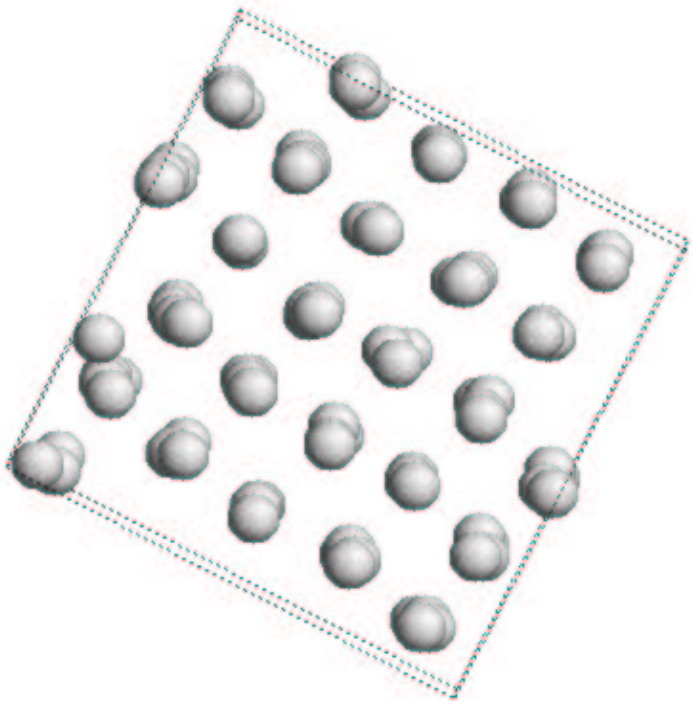

Figure 7.45: The centres of gravity of the same system displayed in figure 7.43 and figure 7.44.

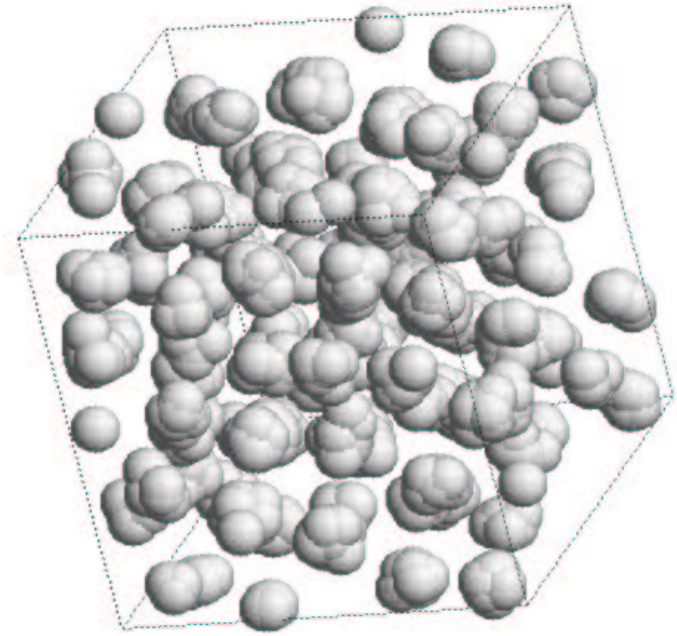

Figure 7.46: Snapshot of a MC simulation of 1 241 particles at $\varrho^* = 6.0$ and $\varepsilon^* = 2$ for the GGCM-4. No regular arrangement can be discerned.

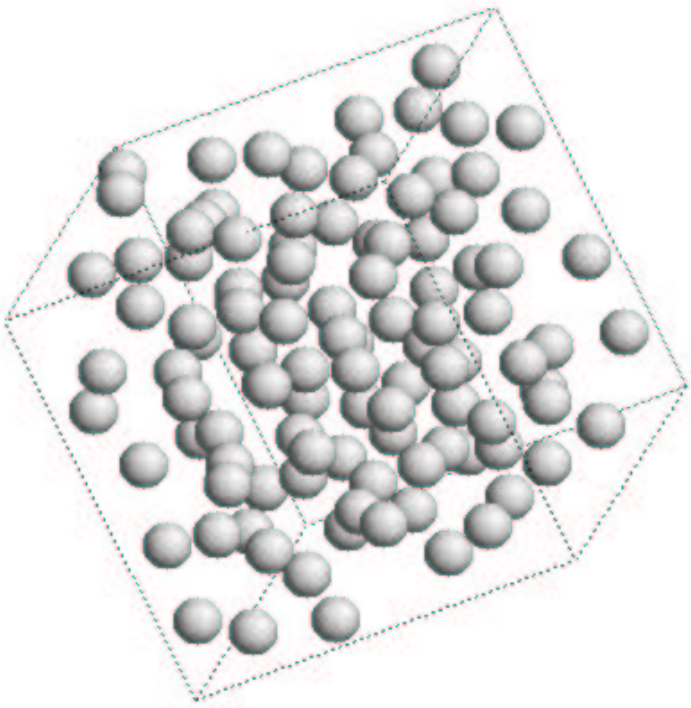

Figure 7.47: The centres of gravity of the same system displayed in figure 7.46.

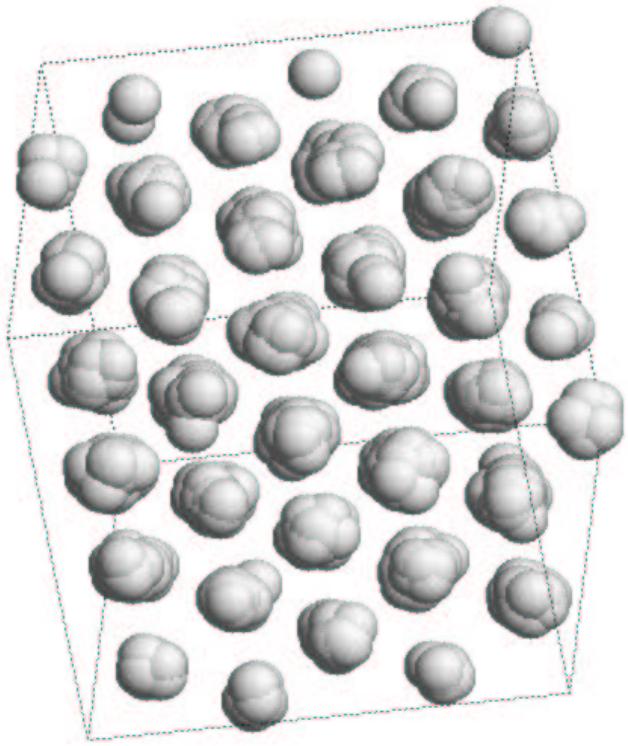

Figure 7.48: Snapshot of a MC simulation of 1403 particles at $\varrho^* = 7.0$ and $\varepsilon^* = 2$ for the GGCM-4. For this density, the system seems to form a perfect fcc crystal.

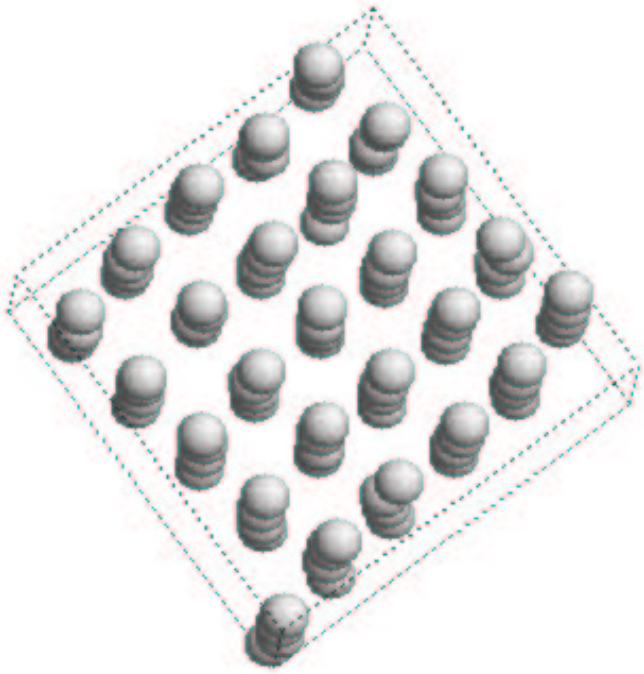

Figure 7.49: The centres of gravity of the same system displayed in figure 7.48.

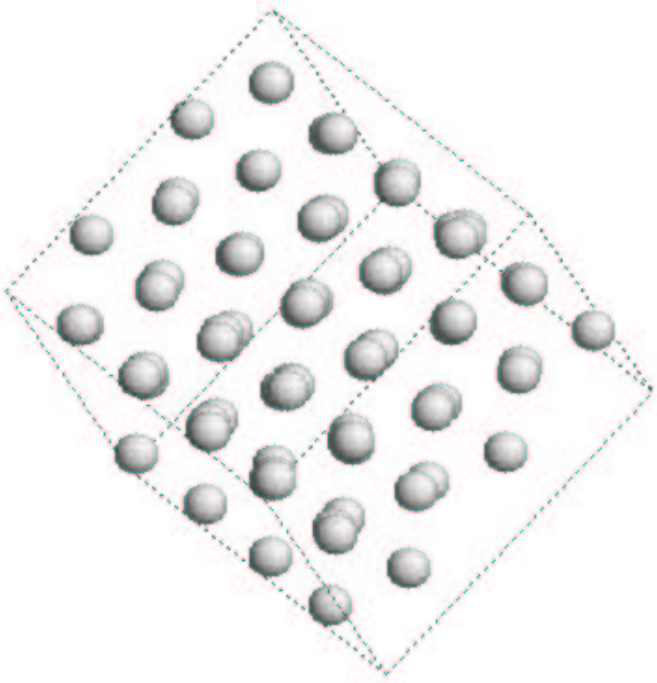

Figure 7.50: Another view of the centres of gravity of the same system displayed in figure 7.48.

7.3.3 The Dimensionless Equation of State Z

This section is organised as follows: First, we are going to verbally examine the results for the dimensionless equation of state $Z = \beta P/\varrho$ as obtained by the different thermodynamic routes of the closure relations considered in this thesis. After this, we show the following plots: A comparison of the results for Z of the MSA compared to the data obtained by the MC simulations at $\varepsilon^* = 0.1$ and varying ϱ^* followed by the same plots for the HNC and the PY approximation. Furthermore, we present a plot of Z according to the MSA, HNC and PY approximations compared to the data from MC simulations for $\varepsilon^* = 2$ and varying ϱ^*.

Compared with the data of MC simulations, the MSA only yields satisfactory results for $\beta P/\varrho$ for low energies and low densities. As soon as clustering sets in, the virial and the energy equation cease to produce meaningful solutions (see figure 7.54), whereas the results obtained via the compressibility route are in disagreement with the data of the MC simulations.

Once again, the HNC closure yields very good results for the homogeneous liquid phase. For the GGCM, the energy route overestimates the pressure, whereas the solutions of the compressibility and the virial route are indistinguishable. As soon as clustering sets in, the Broyles algorithm does not converge any more and no solution can be obtained.

For the homogeneous liquid phase, the results obtained by the PY closure are similar to those calculated by HNC. Once again, the energy route overestimates the pressure, whereas the results

of the compressibility and virial route are in good accordance with the MC simulations. For high energies and high densities, the compressibility route strongly overestimates the pressure. For small clusters, the PY closure is still able to provide results, but they are not in accordance with the results of MC simulations. However, no solution can be obtained in the region where the system forms larger clusters.

Summarising, for the fluid phase without clustering the results of the IETs are in good accordance with the data obtained by MC simulations and the dimensionless equation of state Z is a linear function of the reduced density ϱ^*. As soon as clustering starts, the results of Z deviate from this straight line (i.e. they are below the line), which is an indication of the sequence of clustering transitions taking place.

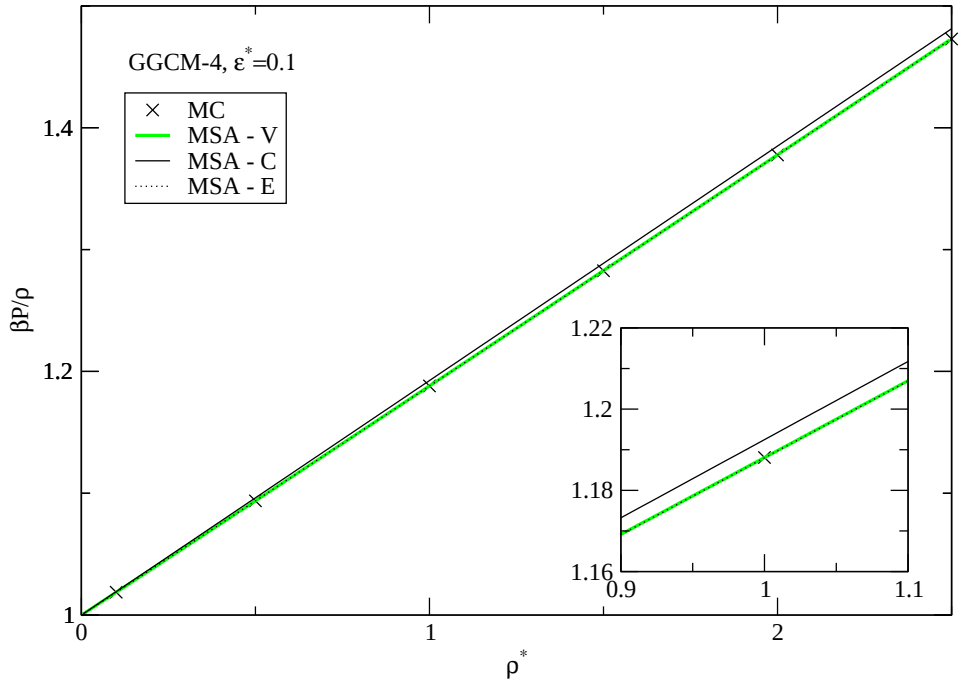

Figure 7.51: Comparison of $\beta P/\varrho$ as a function of ϱ^* for the GGCM-4 according to the MSA and MC simulations for $\varepsilon^* = 0.1$. The compressibility route overestimates the pressure.

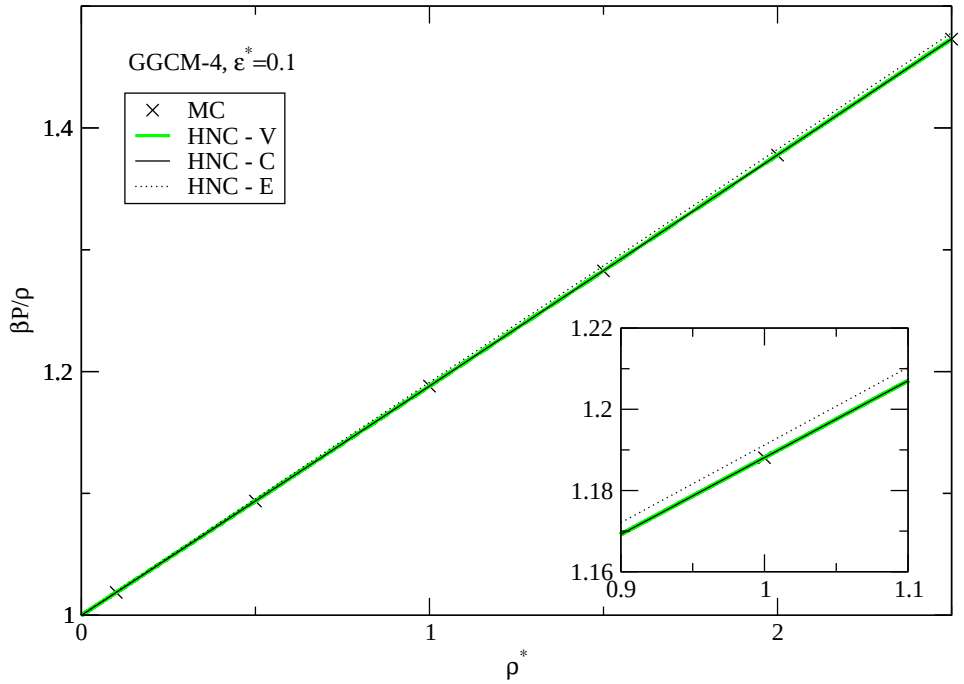

Figure 7.52: Comparison of $\beta P/\varrho$ as a function of ϱ^* for the GGCM-4 according to the HNC approximation and MC simulations for $\varepsilon^* = 0.1$. The energy equation overestimates the pressure.

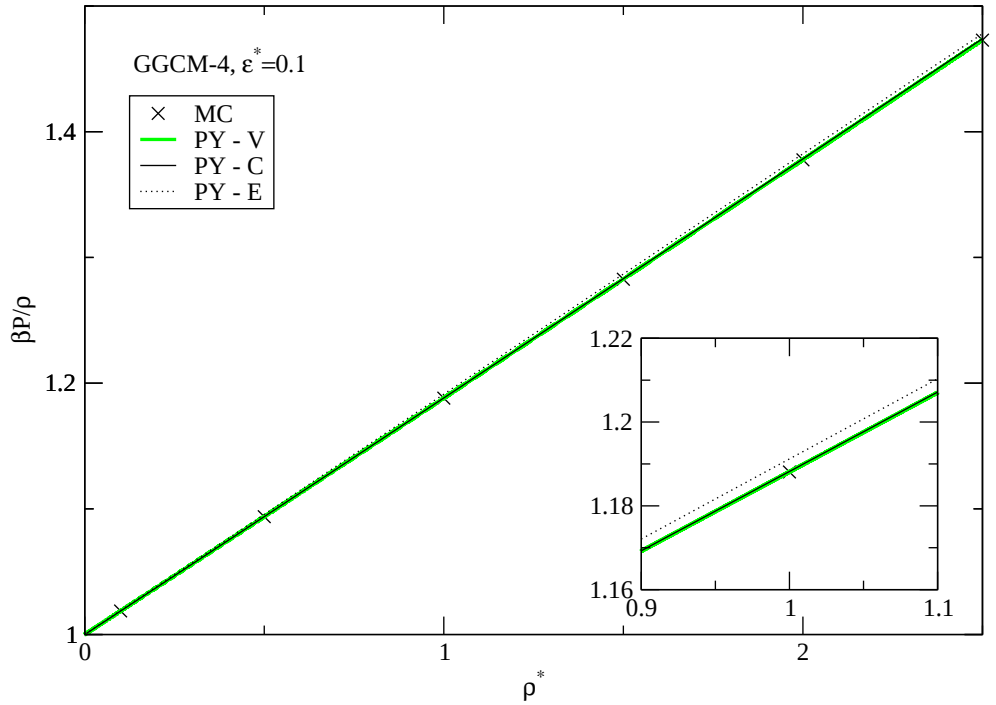

Figure 7.53: Comparison of $\beta P/\varrho$ as a function of ϱ^* for the GGCM-4 according to the PY closure and MC simulations for $\varepsilon^* = 0.1$. The energy route overestimates the pressure.

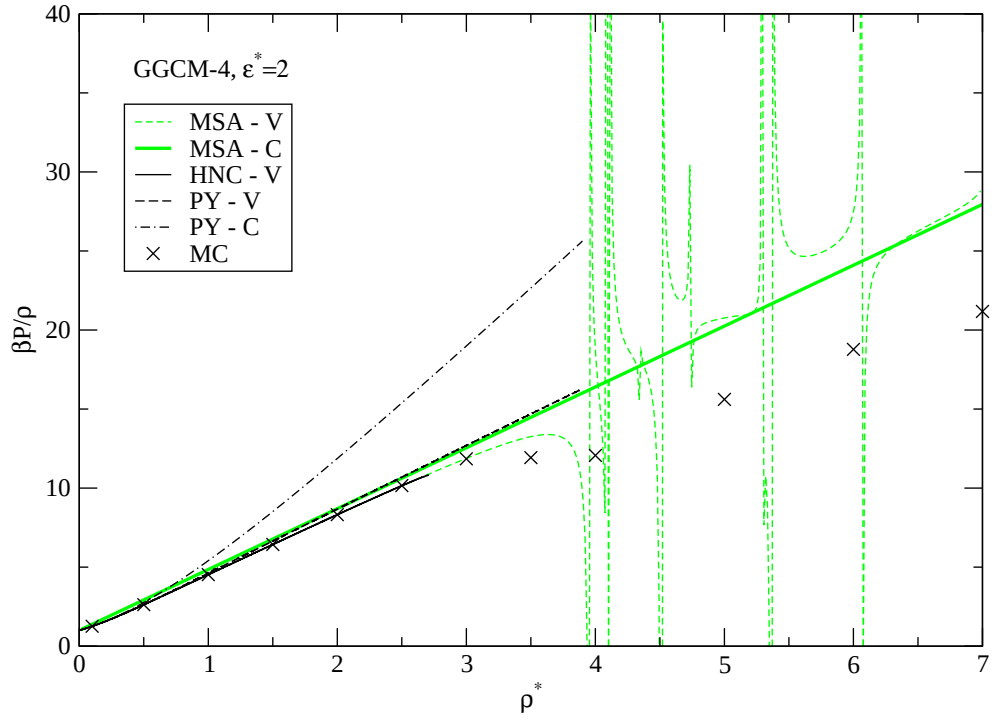

Figure 7.54: Comparison of the results for $\beta P/\varrho$ as a function of ϱ^* for the GGCM-4 at $\varepsilon^* = 2$ as obtained by the virial and compressibility routes of the MSA and PY closures, the virial route of the HNC approximation and MC simulations.

Chapter 8

Summary

In this work we have studied the Gaussian core model, the double Gaussian core model and the generalised Gaussian core model which can all be considered simple model potentials for soft matter. We have analysed the radial distribution function $g(r)$ and the dimensionless equation of state $Z = \beta P/\varrho$ for these systems by means of simple integral equation theories, i.e. the mean spherical, the hypernetted chain and the Percus-Yevick approximation and have checked the results against data from Monte Carlo computer simulations. For the GCM, we have also solved the self-consistent Ornstein-Zernike approximation, which is an advanced IET enforcing thermodynamic self-consistence between the virial and the compressibility route to the equation of state. We have seen that bounded potentials which decay monotonically and lack an attractive part can be classified into two kinds of potentials, namely Q^+ potentials which - upon increasing the density - show re-entrant melting and $Q^\pm$ potentials where - for any value of the reduced energy ε^* - particles collapse into clusters above a certain density.

In the fluid region, a comparison between the results obtained by the IETs and the MC simulation data shows that the IETs yield reasonable results especially for low energies and low densities. Out of the IETs considered, the HNC approximation produces the most reliable results. For systems in the $Q^\pm$-class, the IETs break down in those energy and density regions, where the particles arrange themselves in clusters. This can be understood by taking into account that IETs were developed to describe the homogeneous fluid state and may not be expected to reproduce the translational symmetry of the solid phase. Our investigations have shown that the MSA is able to at least qualitatively predict the onset of clustering, even if it underestimates this effect; however, it is not clear whether this is just a coincidence or not. Thus, of all methods considered in this thesis, only the MC simulations yield reliable results for the clustering phenomenon encountered for $Q^\pm$-potentials.

The IETs used in this thesis were originally applied to hard core systems or systems with a strong repulsion at $r = 0$ and have since proven to be very successful and reliable tools in the prediction of thermodynamic properties of these systems. Inaccuracies in the bridge function $B(r)$, especially

for small r, did not cause problems, because if $v(r) \to \infty$, the exponential in

$$g(r) = e^{-\beta v(r)+h(r)-c(r)+B(r)}$$

is dominated by the interaction and $g(r) \to 0$ for short separations.
On the other hand, when these IETs are applied to bounded potentials, they do not work as well, since these potentials remain finite at $v(0)$ so that an accurate knowledge of the bridge function is essential to bring about a successful theory of the behaviour of these systems. The application of simple IETs showed that their approximations for the bridge function are sometimes rather poor and for instance in the case of the MSA, not only qualitatively false but even unphysical results such as a negative $g(0)$ occurred. Advanced liquid state theories, which enforce self-consistency between different thermodynamic routes to the equation of state, were also applied to soft potential systems, however, even in this case unphysical results were found. Furthermore, it is known from several system studies [23, 40] that soft potentials lead to considerably more rich and exotic phase diagrams than hard core potentials: these potentials allow the particles to overlap, so phenomenona like clustering or freezing into complex structures occur and simple IETs have neither been conceived nor are they able to predict this behaviour.
Thus, one has to admit that conventional IETs developed for hard core systems are not as suitable for bounded potentials as one might wish: they may be very successful for strongly repulsive interactions, but they do not in general yield reliable results for soft potentials. Detailed investigations for all sorts of potentials, as for instance the penetrable sphere model, the GCM and the Fermi distribution model [25, 26, 41] showed that no general prediction can be made about the regions of density and energy where the different IETs yield reasonable results for a chosen system. Therefore, the enhancement of existing theories, the development of new ones and further system studies will be required to bring about a deeper understanding of the general principles that classify the thermodynamic behaviour of soft potentials and which allow to reliably predict the thermodynamics of arbitrary soft matter systems.

Appendix A

Fourier Transformation

In this thesis, we define the Fourier transform of a function $f(\mathbf{r}) : \mathbb{R}^3 \to \mathbb{R}^3$ as follows

$$\hat{f}(\mathbf{k}) = \int_{\mathbb{R}^3} e^{i\mathbf{kr}} f(\mathbf{r}) \, \mathrm{d}^3 r, \tag{A.1}$$

and the inverse Fourier transform reads as

$$f(\mathbf{r}) = \frac{1}{(2\pi)^3} \int_{\mathbb{R}^3} e^{-i\mathbf{kr}} \hat{f}(\mathbf{k}) \, \mathrm{d}^3 k. \tag{A.2}$$

For radially symmetric functions, the last two equations simplify to the following

$$\hat{f}(k) = \frac{4\pi}{k} \int_0^\infty r \sin(kr) f(r) \, \mathrm{d}r \tag{A.3}$$

$$f(r) = \frac{1}{(2\pi)^3} \frac{4\pi}{r} \int_0^\infty k \sin(kr) \hat{f}(k) \, \mathrm{d}k \tag{A.4}$$

Appendix B

The Mean Spherical Approximation

B.1 The Gaussian Core Model

Fourier Transformation of the Potential

The Fourier transform of the potential is given by

$$\begin{aligned} \hat{v}(k) &= \frac{4\pi}{k}\int_0^\infty r\sin(kr)\,v(r)\;\mathrm{d}r = \\ &= \frac{4\pi\varepsilon}{k}\int_0^\infty r\sin(kr)\,e^{-(r/R)^2}\;\mathrm{d}r = \\ &= \pi^{3/2}\varepsilon\,R^3 e^{-k^2R^2/4}. \end{aligned} \tag{B.1}$$

Fourier Transformation of $c(r)$

The Fourier transform of the direct correlation function reads as

$$\begin{aligned} \hat{c}(k) &= -\beta\hat{v}(k) = \\ &= -\pi^{3/2}\beta\,\varepsilon\,R^3 e^{-k^2R^2/4} = \\ &= -\pi^{3/2}\varepsilon^* R^3 e^{-k^2R^2/4}. \end{aligned} \tag{B.2}$$

Ornstein-Zernike Equation and $\hat{h}(k)$

The Fourier transform of the OZE is defined by (3.14). Hence,

$$\begin{aligned}\hat{h}(k) &= \frac{-\pi^{3/2}\varepsilon^* R^3 e^{-k^2R^2/4}}{1+\pi^{3/2}\varepsilon^* R^3 e^{-k^2R^2/4}} = \\ &= -\frac{\alpha}{\varrho}\frac{1}{e^{k^2R^2/4}+\alpha},\end{aligned} \tag{B.3}$$

where $\alpha = \pi^{3/2}\varrho^*\varepsilon^*$.

The Radial Distribution Function

The radial distribution function at $r = 0$ is given by

$$\begin{aligned}g(0) &= 1+h(0) = \\ &= 1-\frac{\alpha}{\varrho}\frac{1}{8\pi^3}\int e^{-i\mathbf{kr}}\frac{1}{e^{k^2R^2/4}+\alpha}\,\mathrm{d}^3k = \\ &= 1-\frac{\alpha}{\varrho}\frac{1}{8\pi^3}\int \frac{1}{e^{k^2R^2/4}+\alpha}\,\mathrm{d}^3k = \\ &= 1-\frac{\alpha}{\varrho}\frac{1}{8\pi^3}\iiint k^2\sin\vartheta\,\frac{1}{e^{k^2R^2/4}+\alpha}\,\mathrm{d}\varphi\,\mathrm{d}\vartheta\,\mathrm{d}k = \\ &= 1-\frac{\alpha}{2\pi^2\varrho}\int_0^\infty k^2\frac{1}{e^{k^2R^2/4}+\alpha}\,\mathrm{d}k \overset{(D.1)}{=} \\ &= 1+\frac{\varepsilon^*}{\alpha}\,\mathrm{Li}_{3/2}(-\alpha).\end{aligned} \tag{B.4}$$

Virial Route

The pressure P according to the virial equation (3.4) is determined by

$$\left(\frac{\beta P}{\varrho}\right)^{\mathrm{V}} = 1+\frac{1}{2}\varrho\beta\hat{v}(k=0)-\frac{2\pi}{3}\varrho\int_0^\infty r^3\,\frac{\partial\beta v(r)}{\partial r}\,h(r)\,\mathrm{d}r. \tag{B.5}$$

The last term of this equation can be rewritten as

$$\begin{aligned}-\frac{2\pi}{3}\varrho\int_0^\infty r^3\,\frac{\partial\beta v(r)}{\partial r}\,h(r)\,\mathrm{d}r &= -\frac{2\pi}{3}\varrho\frac{1}{4\pi}\int r\frac{\partial\beta v(r)}{\partial r}\left\{\frac{1}{8\pi^3}\int e^{-i\mathbf{kr}}\hat{h}(k)\,\mathrm{d}^3k\right\}\,\mathrm{d}^3r = \\ &= \frac{\varrho\varepsilon^*}{24R^2\pi^3}\int \hat{h}(k)\left\{\int r^2e^{-(r/R)^2}e^{-i\mathbf{kr}}\,\mathrm{d}^3r\right\}\,\mathrm{d}^3k = \\ &= \frac{\varrho\varepsilon^*}{24R^2\pi^3}\int \hat{h}(k)\frac{4\pi}{k}\left\{\int_0^\infty r^3e^{-(r/R)^2}\sin(kr)\,\mathrm{d}r\right\}\,\mathrm{d}^3k =\end{aligned}$$

$$
\begin{aligned}
&= -\frac{\varrho^* \varepsilon^*}{96\pi^{3/2}} \int \hat{h}(k)\, e^{-k^2 R^2/4} \left(k^2 R^2 - 6\right)\, \mathrm{d}^3 k = \\
&= -\frac{\alpha\, \varepsilon^* R^3}{24\pi^{1/2}} \int_0^\infty \frac{k^2 \left(k^2 R^2 - 6\right)}{e^{k^2 R^2/4} \left(\alpha + e^{k^2 R^2/4}\right)}\, \mathrm{d}k = \\
&= \frac{\varepsilon^*}{2\alpha} \left\{ \mathrm{Li}_{5/2}(-\alpha) - \mathrm{Li}_{3/2}(-\alpha) \right\}. \qquad \text{(B.6)}
\end{aligned}
$$

This finally leads to

$$
\left(\frac{\beta P}{\varrho}\right)^{\mathrm{V}} = 1 + \frac{1}{2}\,\alpha - \frac{\varepsilon^*}{2\alpha} \left\{ \mathrm{Li}_{3/2}(-\alpha) - \mathrm{Li}_{5/2}(-\alpha) \right\}. \qquad \text{(B.7)}
$$

Compressibility Route

According to the compressibility route, the pressure can be written as

$$
\begin{aligned}
(\beta P)^{\mathrm{C}} &= \int_0^\infty \frac{\partial \beta P(\varrho')}{\partial \varrho'}\, \mathrm{d}\varrho' = \\
&= \int_0^\varrho \left[1 - \varrho' \hat{c}(k=0, \varrho')\right] \mathrm{d}\varrho' = \\
&= \int_0^\varrho \left[1 + \pi^{3/2} \varrho' \varepsilon^* R^3\right] \mathrm{d}\varrho' = \\
&= \varrho + \frac{\varrho^2}{2}\, \hat{c}(k=0). \qquad \text{(B.8)}
\end{aligned}
$$

One obtains

$$
\left(\frac{\beta P}{\varrho}\right)^{\mathrm{C}} = 1 + \frac{1}{2}\,\alpha. \qquad \text{(B.9)}
$$

Energy Route

The excess internal energy per particle U^{ex}/N is given by

$$
\begin{aligned}
\frac{\beta U^{\mathrm{ex}}}{N} &= 2\pi\varrho\beta \int_0^\infty v(r)\, g(r)\, r^2\, \mathrm{d}r = \\
&= 2\pi\varrho\beta \int_0^\infty v(r) \left[1 + h(r)\right] r^2\, \mathrm{d}r = \\
&= 2\pi\varrho\varepsilon^* \int_0^\infty e^{-(r/R)^2} r^2\, \mathrm{d}r + 2\pi\varrho\varepsilon^* \frac{1}{4\pi} \int e^{-(r/R)^2} \left\{ \frac{1}{8\pi^3} \int \hat{h}(k) e^{-i\mathbf{kr}}\, \mathrm{d}^3 k \right\} \mathrm{d}^3 r = \\
&= \frac{\alpha}{2} + \frac{\varrho\varepsilon^*}{16\pi^3} \int \hat{h}(k) \left\{ \frac{4\pi}{k} \int_0^\infty r \sin(kr)\, e^{-(r/R)^2}\, \mathrm{d}r \right\} \mathrm{d}^3 k =
\end{aligned}
$$

$$
\begin{aligned}
&= \frac{\alpha}{2} + \frac{\varrho^* \varepsilon^*}{16\pi^{3/2}} \int \hat{h}(k)\, e^{-k^2 R^2/4}\, \mathrm{d}^3 k = \\
&= \frac{\alpha}{2} + \frac{\varrho^* \varepsilon^*}{4\pi^{1/2}} \int_0^\infty k^2\, \hat{h}(k)\, e^{-k^2 R^2/4}\, \mathrm{d}k = \\
&= \frac{\alpha}{2} - \frac{\alpha \varepsilon^* R^3}{4\pi^{1/2}} \int_0^\infty \frac{k^2\, e^{-k^2 R^2/4}}{\alpha + e^{k^2 R^2/4}}\, \mathrm{d}k = \\
&= \frac{\alpha}{2} - \frac{\varepsilon^*}{2\alpha} \left[\alpha + \mathrm{Li}_{3/2}(-\alpha)\right]. \qquad \text{(B.10)}
\end{aligned}
$$

Then, the excess free energy per particle F^{ex}/N is obtained by

$$
\begin{aligned}
\frac{\beta F^{\mathrm{ex}}}{N}(\varrho) &= \int_0^\infty \frac{\beta' U^{\mathrm{ex}}}{N}(\beta', \varrho)\, \frac{\mathrm{d}\beta'}{\beta'} = \\
&= \int_0^{\varepsilon^*} \frac{\beta U^{\mathrm{ex}}}{N}\, \frac{\mathrm{d}\tilde{\varepsilon}^*}{\tilde{\varepsilon}^*} = \\
&= \int_0^{\varepsilon^*} \left\{ \frac{\pi^{3/2} \varrho^*}{2} - \frac{1}{2} - \frac{1}{2\tilde{\alpha}} \mathrm{Li}_{3/2}(-\tilde{\alpha}) \right\} \mathrm{d}\tilde{\varepsilon}^* = \\
&= \frac{\alpha}{2} - \frac{\varepsilon^*}{2} - \frac{\varepsilon^*}{2\alpha} \mathrm{Li}_{5/2}(-\alpha) = \\
&= \frac{\alpha}{2} - \frac{\varepsilon^*}{2\alpha} \left[\alpha + \mathrm{Li}_{5/2}(-\alpha)\right]. \qquad \text{(B.11)}
\end{aligned}
$$

The excess pressure P^{ex} of the system is given as a derivative of the excess free energy F^{ex}

$$
\begin{aligned}
\left(\frac{\beta P^{\mathrm{ex}}}{\varrho}\right)^{\mathrm{E}} &= \varrho \frac{\partial \beta F^{\mathrm{ex}}/N}{\partial \varrho} = \\
&= \varrho \frac{\partial}{\partial \varrho} \left\{ \frac{\alpha}{2} - \frac{\varepsilon^*}{2} - \frac{\varepsilon^*}{2\alpha} \mathrm{Li}_{5/2}(-\alpha) \right\} = \\
&= \frac{\alpha}{2} - \frac{\varepsilon^*}{2\alpha} \left\{ \mathrm{Li}_{3/2}(-\alpha) - \mathrm{Li}_{5/2}(-\alpha) \right\}. \qquad \text{(B.12)}
\end{aligned}
$$

Finally, the pressure P according to the energy route yields

$$
\left(\frac{\beta P}{\varrho}\right)^{\mathrm{E}} = 1 + \left(\frac{\beta P^{\mathrm{ex}}}{\varrho}\right)^{\mathrm{E}} = 1 + \frac{1}{2}\alpha - \frac{\varepsilon^*}{2\alpha} \left\{ \mathrm{Li}_{3/2}(-\alpha) - \mathrm{Li}_{5/2}(-\alpha) \right\}. \qquad \text{(B.13)}
$$

B.2 The Double Gaussian Core Model

Fourier Transformation of the Potential

The Fourier transform of the potential is given by

$$\begin{aligned}\hat{v}(k) &= \frac{4\pi}{k}\int_0^\infty r\sin(kr)\,v(r)\,\mathrm{d}r = \\ &= \frac{4\pi\varepsilon}{k}\int_0^\infty r\sin(kr)\,\left(e^{-r^2/R^2}-\eta e^{-r^2/\zeta^2R^2}\right)\,\mathrm{d}r = \\ &= \pi^{3/2}\varepsilon R^3\left(e^{-k^2R^2/4}-\eta\zeta^3 e^{-\zeta^2k^2R^2/4}\right).\end{aligned} \tag{B.14}$$

Fourier Transformation of $c(r)$

The Fourier transform of the direct correlation function reads as

$$\begin{aligned}\hat{c}(k) &= -\beta\hat{v}(k) = \\ &= -\pi^{3/2}\varepsilon^* R^3\left(e^{-k^2R^2/4}-\eta\zeta^3 e^{-\zeta^2k^2R^2/4}\right).\end{aligned} \tag{B.15}$$

Ornstein-Zernike Equation and $\hat{h}(k)$

The Fourier transform of the OZE is defined by (3.14). Thus,

$$\begin{aligned}\hat{h}(k) &= \frac{-\pi^{3/2}\varepsilon^* R^3\left(e^{-k^2R^2/4}-\eta\zeta^3 e^{-\zeta^2k^2R^2/4}\right)}{1+\pi^{3/2}\varrho^*\varepsilon^*\left(e^{-k^2R^2/4}-\eta\zeta^3 e^{-\zeta^2k^2R^2/4}\right)} = \\ &= -\frac{\alpha}{\varrho}\left(\alpha+\frac{e^{k^2R^2(1+\zeta^2)/4}}{e^{\zeta^2k^2R^2/4}-\eta\zeta^3 e^{k^2R^2/4}}\right)^{-1}.\end{aligned} \tag{B.16}$$

Compressibility Route

The pressure P according to the compressibility route is given by

$$\begin{aligned}(\beta P)^{\mathrm{C}} &= \int_0^\infty \frac{\partial\beta P(\varrho')}{\partial\varrho'}\,\mathrm{d}\varrho' = \\ &= \int_0^\varrho [1-\varrho'\hat{c}(k=0,\varrho')]\,\mathrm{d}\varrho' = \\ &= \int_0^\varrho [1+\pi^{3/2}\varrho'\varepsilon^* R^3\left(1-\eta\zeta^3\right)]\,\mathrm{d}\varrho' = \\ &= \varrho+\frac{\varrho^2}{2}\,\hat{c}(k=0).\end{aligned} \tag{B.17}$$

This equations leads to

$$\left(\frac{\beta P}{\varrho}\right)^{\mathrm{C}} = 1 + \frac{1}{2}\,\alpha\left(1 - \eta\zeta^3\right). \tag{B.18}$$

Virial Route

According to the virial equation, the pressure is given by

$$\left(\frac{\beta P}{\varrho}\right)^{\mathrm{V}} = 1 + \frac{1}{2}\varrho\beta\hat{v}(k=0) - \frac{2\pi}{3}\varrho\int_0^\infty r^3\,\frac{\partial\beta v(r)}{\partial r}\,h(r)\;\mathrm{d}r. \tag{B.19}$$

The last term of this equation can be rewritten as

$$\begin{aligned}
& -\frac{2\pi}{3}\varrho\int_0^\infty r^3\,\frac{\partial\beta v(r)}{\partial r}\,h(r)\;\mathrm{d}r = \\
= \;& -\frac{2\pi}{3}\varrho\frac{1}{4\pi}\int r\frac{\partial\beta v(r)}{\partial r}\left\{\frac{1}{8\pi^3}\int e^{-i\mathbf{kr}}\hat{h}(k)\;\mathrm{d}^3k\right\}\;\mathrm{d}^3r = \\
= \;& -\frac{\varrho}{48\pi^3}\iint r\left\{-\frac{2\varepsilon^* r}{R^2}\left(e^{-r^2/R^2} - \frac{\eta}{\zeta^2}e^{-r^2/\zeta^2R^2}\right)\right\}e^{-i\mathbf{kr}}\hat{h}(k)\;\mathrm{d}^3k\mathrm{d}^3r = \\
= \;& \frac{\varrho\varepsilon^*}{24R^3\pi^3}\int\hat{h}(k)\frac{4\pi}{k}\left\{\int_0^\infty r^3\sin(kr)\;\left(e^{-r^2/R^2} - \frac{\eta}{\zeta^2}e^{-r^2/\zeta^2R^2}\right)\mathrm{d}r\right\}\;\mathrm{d}^3k = \\
= \;& -\frac{\varrho\varepsilon^* R^3}{96\pi^{3/2}}\int\hat{h}(k)\left(\frac{k^2R^2-6}{e^{k^2R^2/4}} - \eta\zeta^3\frac{\zeta^2k^2R^2-6}{e^{\zeta^2k^2R^2/4}}\right)\;\mathrm{d}^3k = \\
= \;& \frac{\alpha\varepsilon^* R^3}{24\sqrt{\pi}}\int_0^\infty k^2\left(\alpha + \frac{e^{k^2R^2(1+\zeta^2)/4}}{e^{\zeta^2k^2R^2/4} - \eta\zeta^3 e^{k^2R^2/4}}\right)^{-1}\left(\frac{k^2R^2-6}{e^{k^2R^2/4}} - \eta\zeta^3\frac{\zeta^2k^2R^2-6}{e^{\zeta^2k^2R^2/4}}\right)\;\mathrm{d}k.
\end{aligned} \tag{B.20}$$

This integral is too complicated to be evaluated analytically.

Appendix C

The Self Consistent Ornstein-Zernike Approximation

In the following, we'll use following abbreviation

$$K(\varrho, \beta) =: K. \tag{C.1}$$

The SCOZA starts from the following ansatz for $c(r)$

$$c(r) = \beta K\, v(r). \tag{C.2}$$

The Fourier transform of the direct correlation function $c(r)$ is given by

$$\hat{c}(k) = \pi^{3/2} \varepsilon^* R^3 K\, e^{-k^2 R^2/4}. \tag{C.3}$$

Using the OZE (3.14), one obtains

$$\begin{aligned} \hat{h}(k) &= \frac{\pi^{3/2} \varepsilon^* R^3 K e^{-k^2 R^2/4}}{1 - \pi^{3/2} \varrho^* \varepsilon^* R^3 K e^{-k^2 R^2/4}} \\ &= \frac{\psi}{\varrho} \frac{1}{e^{k^2 R^2/4} - \psi}, \end{aligned} \tag{C.4}$$

where $\psi = \pi^{3/2} \varepsilon^* \varrho^* K$. For the SCOZA, the following equation has to be fulfilled

$$\left(\beta \frac{\partial P}{\partial \varrho} \right)_T^V = 1 - \varrho\, \hat{c}(k = 0). \tag{C.5}$$

The right hand side is given by

$$1 - \varrho\, \hat{c}(k = 0) = 1 - \pi^{3/2} \varrho^* \varepsilon^* K e^{-k^2 R^2/4}|_{k=0} = 1 - \psi \tag{C.6}$$

For the left hand side, the pressure according to the virial route has to be determined

$$\begin{aligned}
\left(\frac{\beta P}{\varrho}\right)^{\mathrm{V}} &= 1-\frac{2\pi}{3}\beta\varrho\int_0^\infty \frac{\partial v(r)}{\partial r}\,g(r)r^3\;\mathrm{d}r = \\
&= 1-\frac{2\pi}{3}\beta\varrho\int_0^\infty \frac{\partial v(r)}{\partial r}r^3\;\mathrm{d}r-\frac{2\pi}{3}\beta\varrho\int_0^\infty \frac{\partial v(r)}{\partial r}\,h(r)r^3\;\mathrm{d}r = \\
&= 1+\frac{\alpha}{2}-\frac{\beta\varrho}{48\pi^3}\iint r\left\{-\frac{2r\varepsilon}{R^2}e^{-r^2/R^2}\right\}e^{-i\mathbf{kr}}\hat{h}(k)\;\mathrm{d}^3r\mathrm{d}^3k = \\
&= 1+\frac{\alpha}{2}-\frac{\varrho\varepsilon^*}{24R^2\pi^3}\int \hat{h}(k)\frac{4\pi}{k}\left\{\int_0^\infty r^3\sin(kr)\,e^{-r^2/R^2}\mathrm{d}r\right\}\mathrm{d}^3k = \\
&= 1+\frac{\alpha}{2}-\frac{R^3\varrho\varepsilon^*}{96\pi^{3/2}}\int \hat{h}(k)e^{-k^2R^2/4}\left(k^2R^2-6\right)\mathrm{d}^3k = \\
&= 1+\frac{\alpha}{2}-\frac{\psi R^3\varepsilon^*}{96\pi^{3/2}}\,4\pi\int_0^\infty \frac{k^2\left(k^2R^2-6\right)}{e^{k^2R^2/4}\left(e^{k^2R^2/4}-\psi\right)}\;\mathrm{d}k = \\
&= 1+\frac{\alpha}{2}-\frac{\varepsilon^*}{2\psi}\left\{\mathrm{Li}_{5/2}(\psi)-\mathrm{Li}_{3/2}(\psi)\right\}. \qquad \text{(C.7)}
\end{aligned}$$

Consequently,

$$(\beta P)^{\mathrm{V}} = \varrho+\frac{\alpha\varrho}{2}-\frac{\varepsilon^*\varrho}{2\psi}\left\{\mathrm{Li}_{5/2}(\psi)-\mathrm{Li}_{3/2}(\psi)\right\}. \qquad \text{(C.8)}$$

Next, the derivative of the pressure is needed:

$$\begin{aligned}
\left(\frac{\partial\beta P}{\partial\varrho}\right)^{\mathrm{V}} &= 1+\alpha-\frac{1}{2\pi^{3/2}R^3}\left\{\frac{\pi^{3/2}\varepsilon^*R^3}{K\psi}\left(K+\varrho\frac{\partial K}{\partial\varrho}\right)\left[\mathrm{Li}_{3/2}(\psi)-\mathrm{Li}_{1/2}(\psi)\right]-\right. \\
&\quad \left.-\frac{1}{K^2}\frac{\partial K}{\partial\varrho}\left[\mathrm{Li}_{5/2}(\psi)-\mathrm{Li}_{3/2}(\psi)\right]\right\} = \\
&= 1+\alpha-\frac{1}{2\pi^{3/2}R^3K^2}\left\{\frac{1}{\varrho}\left(K+\varrho\frac{\partial K}{\partial\varrho}\right)\left[\mathrm{Li}_{3/2}(\psi)-\mathrm{Li}_{1/2}(\psi)\right]-\right. \\
&\quad \left.-\frac{\partial K}{\partial\varrho}\left[\mathrm{Li}_{5/2}(\psi)-\mathrm{Li}_{3/2}(\psi)\right]\right\} = \\
&= 1+\alpha-\frac{1}{2\pi^{3/2}R^3K^2}\left\{\frac{1}{\varrho}K\left[\mathrm{Li}_{3/2}(\psi)-\mathrm{Li}_{1/2}(\psi)\right]+\right. \\
&\quad \left.\frac{\partial K}{\partial\varrho}\left[2\mathrm{Li}_{3/2}(\psi)-\mathrm{Li}_{1/2}(\psi)-\mathrm{Li}_{5/2}(\psi)\right]\right\}. \qquad \text{(C.9)}
\end{aligned}$$

Now, the partial differential equation is given by:

$$1+\alpha-\frac{1}{2\pi^{3/2}R^3K^2}\left\{\frac{1}{\varrho}K\left[\mathrm{Li}_{3/2}(\psi)-\mathrm{Li}_{1/2}(\psi)\right]+\frac{\partial K}{\partial\varrho}\left[2\mathrm{Li}_{3/2}(\psi)-\mathrm{Li}_{1/2}(\psi)-\mathrm{Li}_{5/2}(\psi)\right]\right\} = 1+\psi$$

$$\alpha-\frac{1}{2\pi^{3/2}R^3K^2}\left\{\frac{1}{\varrho}K\left[\mathrm{Li}_{3/2}(\psi)-\mathrm{Li}_{1/2}(\psi)\right]+\frac{\partial K}{\partial\varrho}\left[2\mathrm{Li}_{3/2}(\psi)-\mathrm{Li}_{1/2}(\psi)-\mathrm{Li}_{5/2}(\psi)\right]\right\}-\psi = 0$$

$$\frac{\partial K}{\partial \varrho}\frac{1}{2\pi^{3/2}R^3K^2}\left[2\mathrm{Li}_{3/2}(\psi)-\mathrm{Li}_{1/2}(\psi)-\mathrm{Li}_{5/2}(\psi)\right]= \\ =\alpha-\psi-\frac{1}{2\pi^{3/2}R^3K^2\varrho}K\left[\mathrm{Li}_{3/2}(\psi)-\mathrm{Li}_{1/2}(\psi)\right] \tag{C.10}$$

This finally results in

$$\frac{\partial K}{\partial \varrho}=\frac{K\left\{\pi^3\varrho^2R^6\beta\varepsilon K\left(K+1\right)-\left[\mathrm{Li}_{3/2}(\psi)-\mathrm{Li}_{1/2}(\psi)\right]\right\}}{\varrho\left[2\mathrm{Li}_{3/2}(\psi)-\mathrm{Li}_{1/2}(\psi)-\mathrm{Li}_{5/2}(\psi)\right]}. \tag{C.11}$$

Appendix D

Polylogarithm

The polylogarithm [42, 43] is defined as the complex-valued function

$$\mathrm{Li}_n(z) = \frac{z}{\Gamma(n)} \int_0^\infty \frac{t^{n-1}}{e^t - z}\, \mathrm{d}t \quad \text{for} \quad n > 0, \tag{D.1}$$

where n is a real parameter and z the complex argument. It is also known as *Jonquière's function.* (D.1) can also be written as

$$\mathrm{Li}_n(e^w) = \frac{1}{\Gamma(n)} \int_0^\infty \frac{t^{n-1}}{e^{t-w} - 1}\, \mathrm{d}t, \tag{D.2}$$

where w is normally restricted to the range $|\mathrm{Im}(w)| \leq \pi$.
Because of the singularity in the integrand at $t = w$ in (D.2), the integral is singular at $w = \pm 2\pi i j$ with $j = 0, 1, 2....$ The principal branch is chosen to be the one where $\mathrm{Li}_n(e^w)$ is real for real $w < 0$, and which is continuous in the entire plane except for the positive real axis, where a cut is made from $w = 0$ to infinity, such that $-\pi < \arg(w) \leq \pi$. The function is complex for real arguments $w > 0$, i.e. $z = e^w > 1$.
It can be shown that the derivative of the n-th polylogarithm can be written as

$$\frac{d}{dz}\mathrm{Li}_n(z) = \frac{1}{z}\mathrm{Li}_{n-1}(z). \tag{D.3}$$

(D.1) can be expanded and integrated term by term, giving

$$\mathrm{Li}_n(z) = \sum_{k=1}^{\infty} \frac{z^k}{k^n} \quad \text{for} \quad |z| < 1. \tag{D.4}$$

A detailed list of further relations can be found at [44].
The polylogarithm is implemented in an efficient way in *Mathematica* as `PolyLog[n,z]` using Euler-Maclaurin summation, expansions in terms of incomplete gamma functions and numerical quadrature [45].

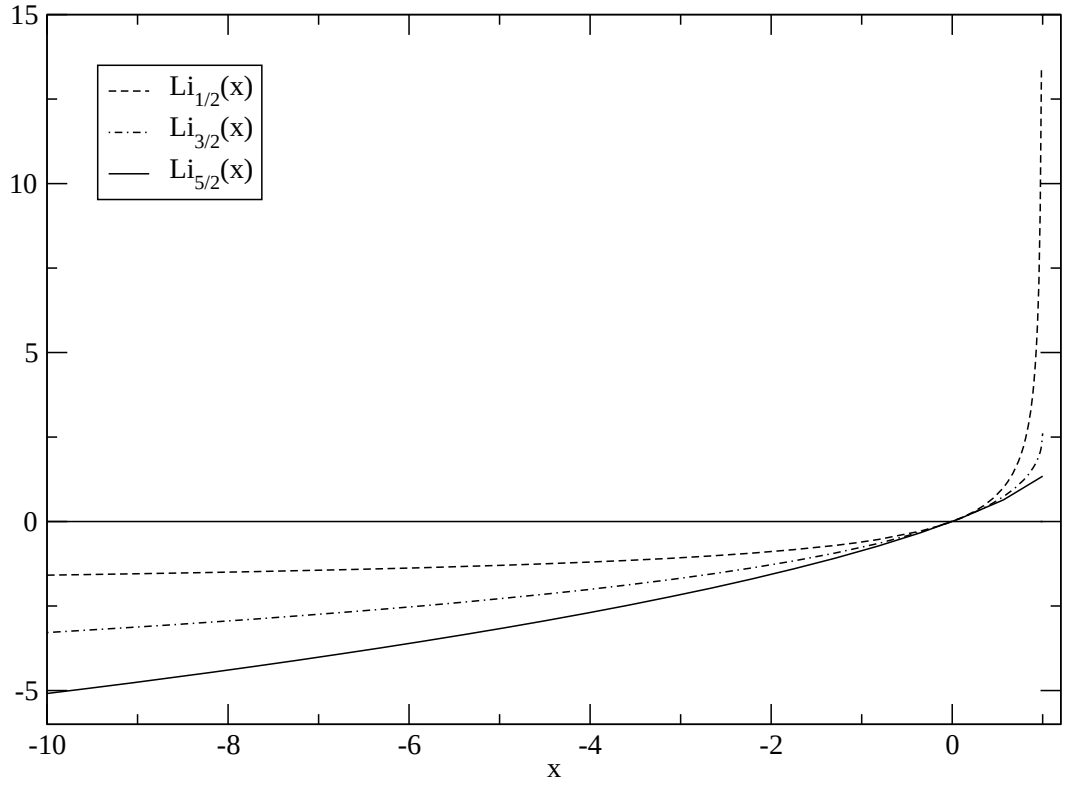

Figure D.1: The polylogarithm for $n = 1/2$, $3/2$ and $5/2$.

Bibliography

[1] J.P. Hansen and I.R. McDonald, *Theory of Simple Liquids*, 2nd ed. (Academic Press, London, 1986).

[2] J.L. Barrat and J.P. Hansen, *Basic Concepts for Simple and Complex Liquids* (Cambridge University Press, Cambridge, 2003).

[3] C.N. Likos, *Effective Interactions in Soft Condensed Matter Physics* (Heinrich-Heine-Universität, Düsseldorf, 2000).

[4] K. Huang, *Statistical Mechanics* (John Wiley and Sons, New York, 1963).

[5] R. Kubo, *Statistical Mechanics* (North-Holland Publishing Company, Amsterdam, 1965).

[6] D. Frenkel and B. Smit, *Understanding Molecular Simulation* (Academic Press, London, 1996).

[7] L.S. Ornstein and F. Zernike, Proc. Akad. Sci. (Amsterdam) **17**, 793 (1914).

[8] J.L. Lebowitz and J. Percus, Phys. Rev. **144**, 217 (1966).

[9] J.M.J. van Leeuwen, J. Groenveld, and J. De Boer, Physica **25**, 792 (1959).

[10] J.K. Percus and G.J. Yevick, Phys. Rev. **110**, 1 (1958).

[11] J.S. Høye and G. Stell, Mol. Phys. **52**, 1071 (1984).

[12] D. Pini, G. Stell, and N.B. Wilding, J. Chem. Phys. **115**, 2702 (2001).

[13] J.S. Høye and A. Borge, J. Chem. Phys. **108**, 8830 (1996).

[14] D. Pini and G.Stell, Physica A **306**, 270 (2002).

[15] C. Caccamo, G. Pellicane, D. Costa, D. Pini, and G. Stell, Phys. Rev. E **60**, 5533 (1999).

[16] M.E.J. Newman and G.T. Barkema, *Monte Carlo Methods in Statistical Physics* (Clarendon Press, Oxford, 1999).

[17] M.P. Allen and D.J. Tildesley, *Computer Simulation of Liquids* (Clarendon Press, Oxford, 1990).

[18] J.M. Yeomans, *Statistical Mechanics of Phase Transitions* (Clarendon Press, Oxford, 1992).

[19] W. Gibbs, *Elementary Principles of Statistical Mechanics* (Yale University Press, New York, 1902).

[20] S. Lipschutz, *Schaum's Outline of Theory and Problems of Probability* (McGraw-Hill Book Company, New York, 1968).

[21] N.G. van Kampen, *Stochastic Processes in Physics and Chemistry* (North-Holland Physics Publishing, Amsterdam, 1981).

[22] N. Metropolis, A. Rosenbluth, M. Rosenbluth, A. Teller, and E. Teller, J. Chem. Phys. **21**, 1087 (1953).

[23] C.N. Likos, N. Hoffmann, H. Löwen, and A.A. Louis, J.Phys.: Condens. Matter **14**, 7681 (2002).

[24] C.N. Likos, N. Hoffmann, A. Jusufi, and H. Löwen, J.Phys.: Condens. Matter **15**, 233 (2003).

[25] C.N. Likos, A. Lang, M. Watzlawek, and H. Löwen, Phys. Rev. E **63**, 31206 (2001).

[26] C.N. Likos, M. Watzlawek, and H. Löwen, Phys. Rev. E **58**, 3135 (1998).

[27] D. Ruelle, *Statistical Mechanics* (Banjamin, New York, 1969).

[28] P.J. Flory and W.R. Krigbaum, J. Chem. Phys. **18**, 1086 (1950).

[29] F.H. Stillinger, J. Chem. Phys. **65**, 3968 (1976).

[30] F.H. Stillinger and D.K. Stillinger, Physica A **244**, 358 (1997).

[31] A. Lang, C.N. Likos, M. Watzlawek, and H. Löwen, J.Phys.: Condens. Matter **12**, 5087 (2000).

[32] A.A. Louis, P.G. Bolhuis, and J.P. Hansen, Phys. Rev. E **62**, 7961 (2000).

[33] C.N. Likos, Phys. Rep. **348**, 267 (2001).

[34] P.G. Bolhuis, A.A. Louis, J.P. Hansen, and E.J. Meijer, J. Chem. Phys. **114**, 4296 (2001).

[35] J. Dautenhahn and C.K. Hall, Macromolecules **27**, 5399 (1994).

[36] Wolfram MathWorld: `http://mathworld.wolfram.com/GeneralizedHypergeometricFunction.html`.

[37] A.A. Broyles, J. Chem. Phys. **33**, 456 (1960).

[38] Wolfram MathWorld: `http://mathworld.wolfram.com/SigmoidFunction.html`.

[39] Wolfram Research, Inc., *Mathematica*, Version 4.2 and 5.

[40] D. Gottwald, C.N. Likos, G. Kahl, and H. Löwen, *Phase Behaviour of Ionic Microgels*, to appear in Phys. Rev. Lett., 2003.

[41] M. Fernaud, E. Lomba, and L.L. Lee, J. Chem. Phys. **112**, 810 (2000).

[42] D. Wood, *The Computation of Polylogarithms*, `http://www.cs.ukc.ac.uk/pubs/1992/110`, 1992.

[43] L. Lewin, *Polylogarithms and Associated Functions* (North Holland, New York, 1981).

[44] Wolfram Research: `http://functions.wolfram.com/ZetaFunctionsandPolylogarithms/PolyLog/`.

[45] S. Wolfram, *The Mathematica Book*, 5th ed. (Wolfram Media Inc., Champaign, 2003).

Acknowledgments

I would like to thank...
...my supervisors Martin Neumann and Gerhard Kahl, not only for their assistance and encouragement, but also for their patience when I decided to fall into nearly every pitfall abundantly present in an unexplored physical area. Furthermore, for their humour and their quest to make me broaden my horizons by reading "The Strudlhof Steps".
...my colleague Dieter Gottwald, not only for helping me out of various pitfalls but also for nice conversations about all the world and Lao-Tse. Without his assistance it would have certainly taken considerably longer to complete this work.
...Dieter and my other colleagues at the University of Technics, Maria-José Fernaud and Peter Winkler - for the comfortable working atmosphere; you made each working day a pleasure.
...Michael Kunzinger for his willingness to help me to solve differential equations and for arousing my interest in programming.
...my colleagues Christina Forster and Herbert Richter from the University of Vienna for their advice, good deeds and friendly faces.
...my colleague and friend Claudia Zechmann, who is all ears for me and is there for me whenever I need good advice.
...my friends Patricia Kaspar, Martin Pflügler, Christian Scheske, Bianca Schubernigg and Martin Stieglmayer for their encouraging words during dry spells, for allowing me to lean on their strong shoulders, when I was about to despond, for their gift of making me laugh and for the inner serenity they give me by being my friends. And last but not least for the hot chocolate that makes a long working day a little bit shorter. I have found you all by myself and won't give you away. ☺
...my boyfriend Andreas Himmetzberger for his love and his readiness to be there for me anytime.
...my parents for their encouragement, for making my studies possible and for their belief in me.
...my grandmothers, whose joy of life and dignity shall be good examples for my life.

Danksagung

Rechterhand standen glatt und verschlossen die Bauten der Universitätsinstitute für Physik und Radiologie, unbegreiflichen Inhalts, und hauchten jene neue Art von Romantik, die gerade von den allerexaktesten Wissenschaften am meisten ausgeht, als würde deren Wesen in ihrer Emanation gleichsam ins Gegenteil verkehrt. - Heimito von Doderer, 'Die Strudlhofstiege'

Ich danke...
...meinen Betreuern Martin Neumann und Gerhard Kahl vorallem für ihre fachliche Unterstützung, aber auch für ihre endlose Geduld mit mir, als ich beschloß, in fast jede der in unerforschtem physikalischem Gebiet reichlich vorhandenen Fallgruben hineinzutappen. Weiters für ihren Humor und ihr Vorhaben, meinen literarischen Horizont um die „Strudlhofstiege" zu erweitern.
...meinem Kollegen Dieter Gottwald nicht nur dafür, daß er mir geduldig aus unzähligen Fallgruben herauszuklettern geholfen hat, sondern auch für die vielen netten und lustigen Diskussionen über Gott, die Welt und Lao-Tse. Ohne seine Hilfe hätte die Fertigstellung dieser Arbeit wohl beträchtlich länger gedauert.
...Dieter und meinen weiteren Kollegen an der TU - Maria-José Fernaud und Peter Winkler - für das überaus angenehme Arbeitsklima - durch sie wurden die Arbeitstage zu Freude und Spaß.
...Michael Kunzinger für seine Bereitschaft, mir beim Lösen von Differentialgleichungen mathematisch unter die Arme zu greifen und dafür, daß er mein Interesse am Programmieren geweckt hat.
...meinen KollegInnen Christina Forster und Herbert Richter von der Universität Wien, daß sie mir mit Rat, Tat und stets freundlichem Gesicht zur Seite standen.
...besonders meiner Kollegin und Freundin Claudia Zechmann, die jederzeit mit offenem Ohr, gutem Rat und großem Herz für mich da ist.
...meinen FreundInnen Patricia Kaspar, Martin Pflügler, Christian Scheske, Bianca Schubernigg und Martin Stieglmayer für ihre aufbauenden Worte entlang von Durststrecken, für ihre starken Schultern, an die ich mich lehnen durfte, wenn ich zu verzagen drohte, für ihre Gabe mich trotzdem zum Lachen zu bringen und die Seelenoasen, die sie mir durch ihre Freundschaft schufen. Und nicht zuletzt danke ich ihnen für heiße Schokolade zur Verkürzung eines langen Unitages. Ich hab euch ganz allein gefunden und geb euch nicht mehr her. ☺
...meinem Freund Andreas Himmetzberger von Herzen für seine Liebe und seine Bereitschaft, jederzeit für mich da zu sein.
...meinen Eltern für ihre seelische Unterstützung, die Ermöglichung meines Studiums und ihren Glauben an mich.
...meinen beiden Großmüttern, deren Lebensfreude und Würde, mit der sie dem Leben begegnen, mir stets ein Vorbild sein soll.

Curriculum Vitae

Personal Data

Name: Bianca Maria Mladek
Birth Date: July 2nd, 1980
Birth Place: Vienna, Austria
Citizenship: Austria

Educational History

1986 - 1990	Evangelische Volkschule am Karlsplatz, Vienna
1990 - 1998	Bundesrealgymnasium BG IX, Wasagasse, Vienna
1998 - 2004	Studies of Physics at the University of Vienna
09/2002 - 12/2003	Diploma Thesis at the "Institute for Experimental Physics" at the University of Vienna in collaboration with the "Institute for Theoretical Physics" at the Vienna University of Technology
2003 -	Studies of Medical Computer Science at the Vienna University of Technology

Employment History

2000 - 2003	Tutor at the "Department of Mathematics" at the University of Vienna

We shall not cease from exploration
And the end of all our exploring
Will be to arrive where we started
And know the place for the first time.
T.S. Elliot, 'Little Gidding'